Optics for high-efficiency full spectrum photovoltaics

Thesis by
Sunita Darbe

In Partial Fulfillment of the Requirements for the
degree of
Ph.D in Materials Science

CALIFORNIA INSTITUTE OF TECHNOLOGY
Pasadena, California

2017
(Defended October 24, 2016)

Sunita Darbe
ORCID: 0000-0002-8099-1814

ACKNOWLEDGEMENTS

There were many people who enabled this work in a variety of ways. First, thanks to my advisor Professor Harry Atwater who ambitiously started the Full Spectrum photovoltaics project and invited me to participate in it. He provided on-going optimism, an endless supply of ideas, and the resources to tackle the wide range of tasks this project would require. My work was funded by the Advanced Research Projects Agency-Energy (ARPA-E), U.S. Department of Energy, under Open 2012 Award Number DE-AR0000333 and MOSAIC Program Award ARPA-E Award No. DE-AR0000627 and the Dow Chemical Company through its University Partnership Program.

The Full Spectrum Photovoltaics project was carried out by a large team that provided support throughout my graduate career. Emily Kosten was an example of skepticism and showed me the value of not accepting something until I have convinced myself why. Emily Warmann was a consistent collaborator throughout prototyping and simulation efforts – making CPC, CAD designs and mechanical parts. Her optimization of bandgaps for spectrum splitting photovoltaics and work on annual energy production also provided a crucial basis for much of our system design efforts. Matthew Escarra was a mentor to me throughout my graduate career, collaborating closely on the holographic spectrum splitting work. My work on cost modeling was a small addition to primary work done by Kelsey Whitesell-Horowitz. Carissa Eisler was my conference roomie, confidant and friend. John Lloyd built the CPC measurement set-up and so much else. You were a dependable, resourceful colleague and provided an example I aspire to. Cris Flowers was my sounding board for everything from lab safety to optical measurements to office etiquette. Thank you for listening, for your thoughtful responses, and for asking me when you had questions too. Pilar Espinet, Annabelle Sibue, Michelle Dee, and Dirk-Jan Spaandermann made a variety of contributions to our sprawling project including cell measurements, CPC fabrication, CPC procurement and mechanical design. Rebekah Feist, Weijun Zhou and Jim Stevens from Dow provided support, encouragement and guidance.

For the TLSC project, Noah Bronstein from Berkeley introduced us to the Monte Carlo model that he and Vivian Ferry developed for LSC. David Needell took up that the modeling mantle. Colton Bukowsky designed the DBR filters.

The Atwater group has many resources and facilities primarily maintained by fellow group members. Nick Batara trained me on and maintained both the ellipsometer and the group computers for most of my graduate career. I am deeply indebted, as both were primary tools. Davis Darvish got me started on the group computer cluster and Phil Jahelka has been fielding my tech questions most recently. Lab safety officers Jeff Bosco, Rebecca Glaudell, Kelly Mauser and Cris Flowers trained, consulted and guided the rest of us. Ragip Pala set up and trained me on the SARP system; Giulia and Siying provided additional help. Jing-Shun Huang maintained the sputterer with me. Emily Warmann, Hal Emmer and Siying Peng all helped me with the confocal microscope. Hal Emmer taught me a little bit about vacuum systems and a lot about common-sense trouble-shooting of equipment. Dagny Fleischman trained me on the ebeam evaporator. Rebecca Saive trained me on the AFM. Ray Weitekampe and Adam Pietrick trained me help with the MMRC integrating sphere. I used Ali Ghaffari's PDMS lab extensively, and he deserves thanks for increasing order in our sometimes chaotic labs.

In addition, all the members and affiliates of the Atwater group I overlapped with. You contributed to my work and had on-going impacts on how I think about my work. You listened to my group meeting presentations and practice talks for conferences, asked questions, discussed your own work, and answered my random questions about software, tools, physics and managing up. There are too many people to name and I will surely forget too many, so thank you all.

All the administrative support I received from Christy Jenstad, Tiffany Kimoto, Jennifer Blankenship, Liz Jennings, Lyann Lau, Connie Rodriguez, Michelle Rodriguez, Tess Legaspi, Natalie Gilmore, Mary Sikora and Helen Duong over the years made the ride smoother and more pleasant. In the KNI I received training and help from staff members Melissa Melendes, Guy de Rose, Matt Sullivan Hunt, Nils Asplund, and Steven Martinez. The collaborative environment of KNI relies on a collaborative user environment. Thanks to Max Jones, Yu Horie, and Amir Arbabi for guidance on fabrication work.

Finally, I must acknowledge my master's advisor Pascale Chenevier. Working in her lab prompted my interest in continuing my scientific education by pursuing a Ph.D. My friends Jackie and Sarah convinced me to apply to Caltech. Once I got here, my entering first year materials science class and the many others we adopted into the lunch table crew including Andrew Hoff, Max Murialdo, Renee McVay, Mark Harfouche, Kevin Fiedler, Ivan Papusha, provided both social respite from work and

added breadth to my Caltech education. To my friends Sam, Erik, Jackie, Sarah, Chengyun, Lisa - thank you! There is too much to say to say more than that. Finally, my parents and Oliver pushed and reminded me that good enough and finished is the goal, even when I did not receive that advice gracefully or gratefully.

ABSTRACT

While the price of solar energy has dropped dramatically in the last few years, costs must be further reduced to reach wide-scale adoption. One strategy to decrease cost is to increase efficiency. Photovoltaic energy conversion is most efficient for a narrow frequency range. Lack of absorption of low energy photons and thermalization of high-energy photons leads lead to a loss of over 40% of incident solar power on a silicon cell. Current-matching and lattice-matching restrictions limit the efficiency of traditional monolithic multijunction solar cells. In order to avoid these limitations and realize ultrahigh efficiency (close to 50%), this thesis explores use of optical elements to split broadband sunlight into multiple spectral bands that can each be sent to physically separated solar cells tuned to best convert that band.

Design of a holographic diffraction grating based spectrum-splitting system resulted in a simulated module efficiency of 37%, meeting the efficiency of state-of-the-art modules. One of four holographic grating stacks is experimentally characterized. Next, a design incorporating dichroic filters, seven subcells with bandgaps spanning the solar spectrum, and concentrators with efficiency potential exceeding 45% module efficiency is presented. While prototyping this design, we also used on-going cost-modeling to ensure that our design was on-track to be a high-volume technology with low lifetime energy cost.

Finally, high-contrast gratings are used as resonant, dielectric spectrally selective mirrors in a tandem luminescent solar concentrator and as alternatives to Bragg reflectors. Gratings can have omnidirectional, high reflectivity by appropriately offsetting grating resonances in nano-patterned subwavelength thickness high-refractive index material. Subwavelength feature sizes suppress diffraction, and the high-refractive index of the grating layer leads to relatively angle-insensitive reflectance. Gratings can be fabricated by nanoimprint lithography, making them a scalable and economical option for photovoltaic applications. Simulations show hemispherically average reflectivity near 90% possible from a single subwavelength thickness layer. These properties are well suited for a variety of applications including multiple spectrum-splitting device architectures.

PUBLISHED CONTENT AND CONTRIBUTIONS

[1] M. D. Escarra, S. Darbe, E. C. Warmann, and H. A. Atwater, "Spectral-splitting photovoltaics: Holographic spectrum splitting in eight-junction, ultra-high efficiency module," in *IEEE PVSC 39*, 2013. DOI: http://dx.doi.org/10.1109/PVSC.2013.6744503,
S.D. participated in the conception of the project and performed holographic grating simulations.

[2] S. Darbe, M. D. Escarra, E. C. Warmann, and H. A. Atwater, "Spectral-splitting photovoltaics: Holographic spectrum splitting in eight-junction, ultra-high efficiency module," in *High and Low Concentrator Systems for Solar Electric Applications VIII*, 2013. DOI: http://dx.doi.org/10.1117/12.2024610,
S.D. participated in the conception of the project, performed holographic grating simulations, and wrote the manuscript.

[3] S. Darbe and H. A. Atwater, "Resonant dielectric high-contrast gratings as spectrum splitting optical elements for ultrahigh efficiency (>50%) photovoltaics," in *IEEE PVSC 42*, 2015. DOI: http://dx.doi.org/10.1109/PVSC.2015.7356160,
S.D. performed optical simulations, data analysis, and wrote the manuscript.

[4] C. N. Eisler, C. A. Flowers, P. Espinet, S. Darbe, E. C. Warmann, J. Lloyd, M. Dee, and H. A. Atwater, "Designing and prototyping the polyhedral specular reflector, a spectrum-splitting module with projected >50% efficiency," in *IEEE PVSC 42*, 2015. DOI: http://dx.doi.org/10.1109/PVSC.2015.7356406,
S.D. participated in spectrum-splitting optical element prototype and concentrator fabrication.

TABLE OF CONTENTS

LIST OF ILLUSTRATIONS

LIST OF TABLES

NOMENCLATURE

$\$/W_p$. Cost per peak power rating of a photovoltaic system. E.g. If a silicon module costs $200 and has a maximum power of 200 W, its $\$/W_p$ cost is $\$1/W_p$.

μ. Electrochemical potential.

azimuthal angle. Longitude angle.

B270. A common variety of glass.

bankability. Ability to obtain financing..

BFO. Bismuth ferrite.

BOS. Balance of System - all non-module costs of an installed photovoltaic system.

bypass diode. In strings of solar cells if any one unit fails, the whole unit's energy production can be lost as the failed unit starts acting as a resistor. A bypass diode is triggered by such a situation to put such cells either shadowed during part of the day or damaged into open circuit to prevent this.

chirp. To modify the period of a grating as a function of position in one or more spatial dimension such that the final structure is quasi-periodic structure.

CNC. Computer numerical control, as in CNC machine tools, which are automated rather than manually controlled.

CPC. Compound parabolic concentrator.

CPV. Concentrating photovoltaics.

DBR. Distributed Bragg reflector.

DCG. Dichromated gelatin.

DNI. Direct normal incidence, includes both light directly from the sun and circumsolar irradiance, which is the halo around the sun caused by atmospheric scattering.

ebeam. Electron beam.

EQE. External quantum efficiency.

ERE. External radiative efficiency.

escape cone. The cone of angles not trapped by total internal reflection in a higher refractive index material at its interface with a lower refractive index material defined by the critical angle given by Snell's law.

HCG. High-contrast grating.

HCPV. High concentration photovoltaics.

HIT cell. Silicon Heterojunction with Intrinsic Thin layer solar cell device design.

HOE. Holographic optical element.

HSS. Holographic spectrum splitter.

IQE. Internal quantum efficiency.

IRE. Internal radiative efficiency.

k. Boltzmann constant.

LCOE. Levelized cost of electricity.

LSC. Luminescent solar concentrator.

module. Discrete power producing unit of a photovoltaic system. In CPV, modules are sometimes grouped to be installed on a single tracker.

negative resist. Polymerizes where exposed.

NPV. Net present value.

NREL. National Renewable Energy Laboratory.

packing fraction. In photovoltaics, this is the land area covered by solar collectors when the sun is straight ahead.

PDMS. Polydimethyl siloxane.

polar angle. Angle measured from the grating normal, latitude angle.

positive resist. Dissolves where exposed.

PSR. Polyhedral Specular Reflector.

PV. Photovoltaic.

RCWA. Rigorous coupled wave analysis.

rms. Root mean squared.

runner. The pathway for plastic in an injection mold between the auger where it is melted and the mold cavity. The runners have pinch points at the interface with the part from which they can be easily separated. This process leaves a small nub..

TIR. Total internal reflection.

TMCS. Trimethylchlorosilane.

UV. Ultraviolet.

VPH. Volume phase hologram.

Chapter 1

INTRODUCTION

1.1 Motivation for photovoltaics

Solar energy is a clean, abundantly available power source. As threats of climate change grow more urgent, a carbon neutral power supply is critical. Solar energy is additionally a distributed resource, which makes it a useful power source in areas without reliable grid connection, such as in developing countries or war zones. A variety of factors prevent wide-scale adoption of PV. The cost is nearing and in some cases has hit levels that have been cited as targets for 'grid parity'. However, solar energy is not a dispatchable energy source. This creates some natural limits for how much of the power generation mix can come from solar. Older, inadequate grid technology also prevents effective transportation of power across the United States to balance supply and demand. The more favorable cost metrics can be, the more pressure there will be to innovate and tackle these other challenges head-on. In the past few years, the cost of silicon modules has plummeted. In fact, goals set by the Department of Energy Sunshot program of <$/W module cost and <$0.06/kWh for 2020 have been met early. However, remaining system costs, referred to as Balance of System costs, including mounting and electrical hardware, permitting, and installation have not gone down as fast. Increasing the efficiency of a solar module better leverages these fixed costs, decreasing overall solar energy cost.

1.2 Spectrum-splitting photovoltaics

Single-junction photovoltaics have a theoretical detailed-balance efficiency limit of about 33%. [1] A great deal of research and development have led to crystalline silicon and GaAs cells which approach this thermodynamic limit with record efficiencies of 25.6% and 28.8%, respectively. [2] To increase photovoltaic conversion efficiency beyond this, we turn to multijunction solar cells, which address losses due to lack of absorption of photons with energy below the solar cell material bandgap energy and also address losses due to thermalization of carriers generated by photons with energy greater than the bandgap energy. Together these two losses add up to over 40% of total incident solar power. [3] The higher bandgap cells must generate a higher collection voltage for the spectrum splitting to be worthwhile. For high-quality semiconductor materials the V_{OC} of the solar cell is almost linearly related to

the bandgap of the semiconductor material. [4] Thus using higher bandgap materials to collect higher energy photons returns more electrical energy upon absorption and collection. This motivates incorporation of many, high quality absorber materials into a photovoltaic conversion system. The III-V compound semiconductor system provides direct bandgap materials of high material quality with bandgap tunability over much of the target range of interest for solar applications, so we focus on this material system.

Many methods have been explored for incorporating multiple absorbers into photovoltaic devices. In the past decade, epitaxially grown, monolithic tandem cells (typically 2-4 absorbers) have been the focus of research and development. This kind of cell has the advantage of intrinsic splitting of the solar spectrum into different frequency bands. Each cell acts as a long-pass filter allowing lower energy, unabsorbed photons to pass through to the next cell. However, this device architecture has a series of limitations. First of all, high-quality material requires low defect density in the single crystal material. One way to accomplish this is for all layers to be lattice-matched, which restricts choice in the bandgap of each subcell. Alternatively, incorporating subcells which are not lattice matched imposes a requirement for metamorphic buffer layers [5] which adds complexity. Secondly, since monolithic tandem cells are electrically in series, each junction is limited by the current generated by the cell in the stack which generates the least current. These cells are designed so that this current-matching condition maximizes current for a particular solar spectrum. As the solar input varies over the course of a day or year or with changing location, the current match may no longer hold, decreasing efficiency. Finally, for each additional subcell a tunnel junction must also be designed which allows the series electrical connection between each pair of subcells. These three factors limit the number of subcells one can incorporate into monolithic tandem cells. These factors lead to low marginal return on incorporating additional subcells. [6] In a spectrum-splitting architecture, optics external to the cells separate solar light into bands which are directed to an appropriate receiver made up of a cell of tuned bandgap and possibly a concentrating optic. By incorporating many high quality, independently connected subcells of different bandgaps along with high concentration, this approach could lead to higher efficiencies than have been demonstrated by today's monolithic multijunction devices. This spectral-splitting optic also allows each cell to act electrically independently, enhancing annual energy production. [6]

DARPA's Very High Efficiency Solar Cells program set a goal of 50% cell efficiency and funded the current spectrum splitting efficiency record holder which incorporated two multijunction solar cells for a total of five subcells giving 38.5% submodule efficiency. [7] Their spectrum splitting optical element was a Bragg reflector. A full module made with this design was demonstrated to have 36.7% efficiency. [8] The current module efficiency record of 38.9% is held by a four-junction tandem concentrating photovoltaic module. [9] Other recent efforts have used diffraction [10], refraction [11], specular reflection [12], and diffuse reflection [13] to split the solar spectrum. Imenes and Mills [14] reviewed spectrum splitting technologies in 2004 and in 2013 Mojiri et al. provided an update. [15] and also provided a more recent update to their original review. Groups have also worked on holographic approaches. [16],[17] The efficiencies of lateral multijunction devices, however, still lag behind those of traditional multijunction cells and devices.

1.3 Full Spectrum Photovoltaics Project

The Caltech Full Spectrum Photovoltaics Project sought to take advantage of the efficiency benefits of spectrum-splitting to make a 50% module efficiency photovoltaic system. We begin with an internal design competition among three designs. The Polyhedral Specular Reflector (PSR), Holographic Spectrum Splitter (HSS) and the Light Trapping Filtered Concentrator (LTFC). I discuss the HSS in Chapter 2. Work on the LTFC was undertaken by Emily Kosten and John Lloyd. Both the HSS and LTFC had lower optimized simulated efficiency than the Polyhedral Specular Reflector so the latter was chosen as the winner of our internal design competition. We made four functioning optoelectronic submodule prototypes of the PSR as well as intermediate partial prototypes. Ongoing prototyping efforts are underway at the time of this writing. Chapter 3 gives a brief review of design generations and prototype fabrication and performance of the PSR. In more detail, Chapter 4 discusses production of concentrators for prototyping. Chapter 5 explores commercial prospects of the technology. Finally, Chapter 6 covers work on high-contrast grating filters. These near-subwavelength scale optical elements display relatively angle-independent reflectivity with a single subwavelength thickness layer of high refractive index material. This makes them promising in a number of applications, including a variety of spectrum-splitting architectures. In this thesis, they are explored by simulation as an alternative to Bragg mirrors in the PSR as well as for a tandem luminescent solar concentrator.

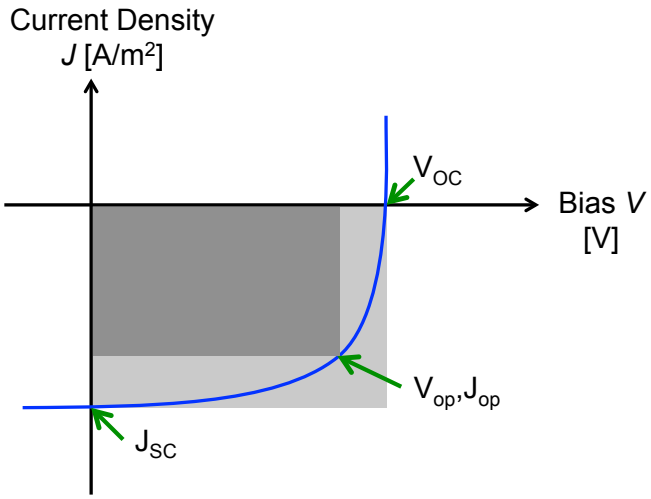

Figure 1.1: Example of a J-V Curve.

1.4 Photovoltaic energy conversation

Photovoltaics are devices that collect the energy imparted to a material by incident light promoting an electron from lower energy state to a higher energy state. Generally speaking this is done in a semiconductor material with the electron promoted from the valence band (the highest energy occupied band) to the conduction band (the lowest energy unoccupied band), leaving an electron vacancy or 'hole'. Rather than decaying back to the ground state by emitting a photon (radiative recombination) or losing energy as heat to the atoms in the material (non-radiative recombination), the excited electron can be collected and run through an external circuit to do useful work. The power P collected by a solar cell is equal to

$$P = V_{op} \times J_{op} = V_{OC} \times J_{SC} \times FF, \tag{1.1}$$

where V_{op} is the voltage and J_{op} the current density produced by the cell when operating at its maximum power point, V_{OC} the voltage of the device at open circuit, J_{SC} is the current that flows in the device at zero bias, and the fill fraction FF the ratio of $V_{op} \times J_{op}$ and $V_{OC} \times J_{SC}$. Fill fraction is a metric for the squareness of the J-V curve, or in other words, of how close the operating performance reaches the potential of that device, as illustrated in Figure 1.1.

The current in the solar cell is determined by how many above-bandgap energy, incident photon are absorbed in the material and collected. The voltage is determined by the quasi-Fermi level separation of electrons and holes in the material. The Fermi energy is the energy level at which the probability of electron occupation is 1/2. At absolute zero, the probably of electron occupation of ground states is 1 while the

probability of occupation of excited states is zero, and the Fermi level lies half-way between the highest energy occupied state and the lowest energy unoccupied state in an undoped semiconductor. At finite temperatures, the probability of occupation changes more gradually from high to low, but as long as the material is at equilibrium the Fermi energy stays the same. When an external energy source is introduced, such as solar illumination, the electrochemical potential of electrons in the material is no longer zero. The quasi-Fermi level splitting indicates the potential difference between excited electrons in the conduction band and excited holes in the valence band. As the charge carrier density goes up, the voltage of the cell goes up, increasing the efficiency of collection. Thus, solar cells illuminated by concentrated sunlight have higher efficiency.

In fact, any effects which increase the ratio of photogenerated current to dark current in the solar cell confer this voltage advantage. Thus if an equal number of photons can be captured by a thinner layer of semiconductor material, there is also a voltage advantage. This can be accomplished by thinning the cell and adding a metallic reflector to the back side. This always a cell to be half as thick as it otherwise would be. Such a back-reflector is added to the single-junction solar cells in our design, but including a sacrificial layer between the active cell layers and semiconductor growth substrate. This layer can be selectively etched away leaving a couple of micron thick free standing solar cell which can have a metallic back reflector deposited on it. Silicon solar cells must be much thicker than III-V solar cells as it absorbs weakly since it has an indirect bandgap. For silicon, rather than a back reflector, the front face of the cell is roughened, significantly increasing the path length of light in the cell (far beyond the factor of two imparted by a back-reflector). [18]

1.5 Relevant optical concepts

Some optical concepts are relevant to work presented in multiple chapters, so I will quickly summarize them here. Light at an interface refracts according to Snell's law,

$$n_1 \sin\theta_1 = n_2 \sin\theta_2 \tag{1.2}$$

where n_i is the refractive index of medium i and θ_i is the direction of propagation measured from the interface normal. Any time light passes through an interface between two materials with dissimilar refractive index there is some reflection given by the Fresnel equations,

$$R_s = \left| \frac{n_1 \cos\theta_1 - n_2 \cos\theta_2}{n_1 \cos\theta_1 + n_2 \cos\theta_2} \right|^2 \tag{1.3}$$

for s or transverse electric (TE) polarization, and

$$R_p = \left| \frac{n_1 \cos\theta_2 - n_2 \cos\theta_1}{n_1 \cos\theta_2 + n_2 \cos\theta_1} \right|^2 \tag{1.4}$$

for p or transverse magnetic (TM) polarization. The polarizations are defined relative to the plane defined by the direction of propagation of light and interface normal. The TE polarization has its electric field vector normal to this plane while for the TM polarization the electric field vector lies in this plane. The behavior of totally unpolarized light can be obtained by averaging the behavior of the two orthogonal polarizations. At Brewster's angle given by

$$\theta_B = arctan\left(\frac{n_2}{n_1}\right), \tag{1.5}$$

R_p goes to zero and the reflected light is only s-polarized. For non-scattering media, the conservation of energy requires $R + T + A = 1$ where R is reflection, T is transmission and A absorption. These reflections coupled with interference effects are exploited in the design of antireflection coatings. The reflectivity of an interface can be decreased using a single thin-film with refractive index $n = \sqrt{n_1 n_2}$ and thickness $\frac{\lambda_0}{4n}$ where λ_0 is the free-space wavelength, n is the refractive index of the antireflection layer and n_1 and n_2 are the refractive indices of the materials on either side of the interface. This occurs because the reflection off the first thin-film interface is of similar amplitude but completely out of phase with the reflection off the back interface causing destructive interference. In contrast, to design a Bragg reflector, one creates a series of interfaces from which the reflected waves constructively interfere. The weak resonances that occur within a thin film due to these interfacial reflections are called Fabry-Perot resonances.

Compound parabolic concentrator

A compound parabolic concentrator (CPC) or Winston cone (named for Roland Winston, who wrote the book [19] and the seminal paper [20] on CPC) is a type of concentrating optical element that is thermodynamically ideal. That is, nearly all light within a certain acceptance angle range θ_{in} is transmitted to the output face, and light outside that acceptance range of angles is not propagated as shows in the blue trace in Figure 1.3. It provides the maximum amount of concentration possible given the angular spread of incident light to be concentrated. It is only possible to concentrate light that has less than maximal directional entropy. In effect, concentrating light is trading off spatial entropy for angular entropy. You

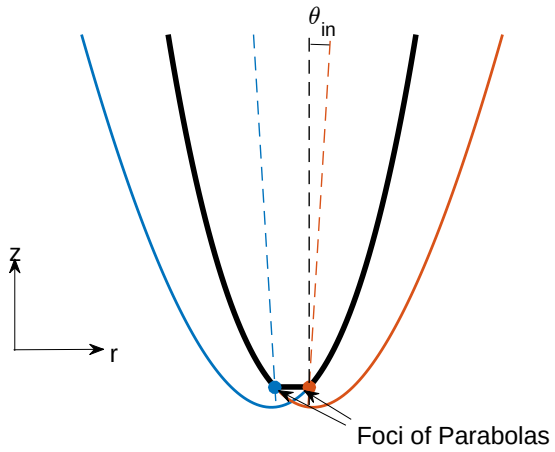

Figure 1.2: Construction of compound parabolic concentrator profile.

can concentrate perfectly collimated light to a diffraction limited spot but cannot concentrate the light of a Lambertian source at all. This principle, often called the brightness theorem or conservation of etendue, is the ultimate limit of the degree of concentration of an optical element,

$$C_{max} = \frac{n_{out} \sin \theta_{out}}{n_{in} \sin \theta_{in}}, \tag{1.6}$$

where C_{max} is the maximum degree of concentration, n_{out} the refractive index of the output medium, n_{in} the refractive index of the incident medium, θ_{out} the maximum angular spread of the concentrated light, and θ_{in} the maximum angular spread of the incident light. The degree of concentration C is the increase in optical power per unit area of the source relative to the output and is either or in the context of photovoltaics expressed as a number of 'Suns', e.g. silicon cells on SunPower's C7 concentrator receive 7 Suns. By pointing a concentrator directly at the sun and restricting θ_{in} to just the solid angle subtended by the sun itself, the maximum possible concentration is around 54,000X. More typically, in concentrating photovoltaics the maximum concentration used is around 1000X with an input angle of 1° to allow for errors in point accuracy of a solar tracker, displacements due to environmental factors such as wind, and to collect circumsolar irradiance (light that is mildly scattered by the atmosphere).

The profile of a CPC is given by

$$(r\cos\theta_{max} + z\sin\theta_{max})^2 + 2a'(1+\sin\theta_{max})^2 r - 2a'\cos\theta_{max}(2+\sin\theta_{max})^2 z - a'^2(1+\sin\theta_{max})(3+\sin\theta_{max}) = 0, \quad (1.7)$$

where 2a' is the width of the output aperture, θ_{max} is the acceptance angle of the CPC, and z is the concentrator height and is zero at the center of the output face, and at $z = 0$, with $r = 0$ as the centerline of the concentrator, $r = a'$. For a circular CPC, this profile is revolved ($r^2 = x^2 + y^2$). For a trough CPC, the profile is extruded in the directional orthogonal to the $r - z$ plane. A square or rectangular CPC is defined by the intersection of two orthogonal trough CPC. Revolved and extruded CPC profiles have fewer aberrations from ideal concentrator behavior than other shapes (see Figure 1.3). Circular cross-section CPC are also much easier to produce due to their rotational symmetry than square cross-section parts, but tiling circular primary CPC would only fill 90.6% of the module input leading to a large aperture area efficiency loss. One arrives at this equation for the profile in the following way: take two identical parabolas with their foci horizontally offset from one another by $2a'$, and tilt each away from the other by angle θ_{max} from the vertical axis. The left side of the parabola on the right and the right side of the parabola on the left, the inside legs, define the CPC curvature as illustrated in Figure 1.2. The straight line between the two foci is the output face. Selecting an acceptance angle and an output area determines the input area and thus the height of the structure as well assuming maximal output angular spread of $\theta_{out} = 90°$. However, for practical photovoltaic systems, the concentrator-cell interface will experience too much Fresnel reflection to have a full hemispherical range of output angles. By adding a conic section at the bottom of the ideal CPC, output angular spread can be decreased at the expense of slightly increased height.

As suggested by Equation 1.7, the medium of the CPC can be air or some other material. If the medium is air, the profile is made by reflective sides, for example, curved silver mirrors. Alternatively, with a solid dielectric material, the reflection comes from total internal reflection (TIR) due to grazing incident angles. As long as the surface quality is high, the reflectivity of total internal reflection is higher than the reflectivity of an air-metal interface with experiences some absorption. There is also a boost in the degree of concentration by a factor of n_{CPC} for a trough concentrator or of n_{CPC}^2 for a square or circular CPC. The downsides of the solid optic include greater weight and volume of material for a comparable size CPC

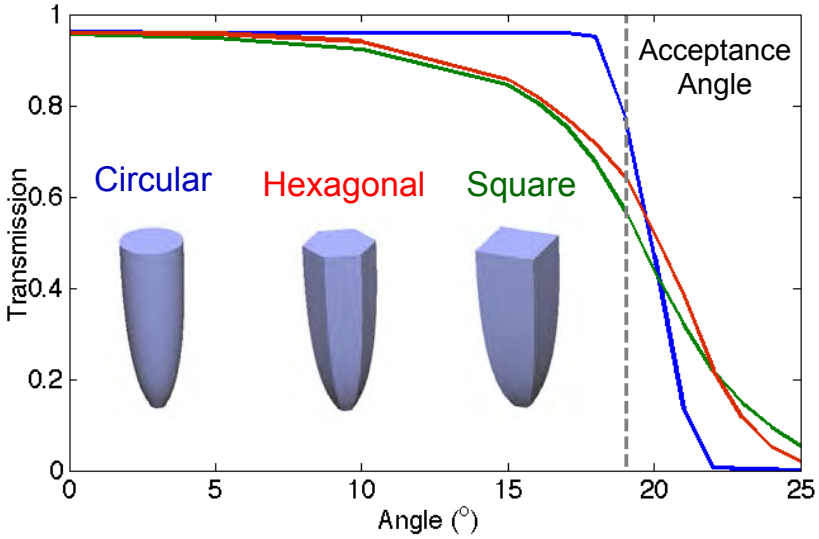

Figure 1.3: Transmission efficiency as a function of incident angle for circular (blue), hexagonal (red) and square (green) cross-section compound parabolic concentrators.

and greater need for high surface quality and cleanliness to ensure that light is not scattered out but successfully reflected by TIR and retained in the concentrator.

While the full height of the gives the highest efficiency of transmission from input to output face for the whole acceptance angle range, truncating a CPC from the top even down to a significant fraction of its intended height decreases efficiency in a nonlinear way. Even down to half the intended profile, much of the intended concentration is retained. Ray tracing simulations of CPC for the Holographic Spectrum Splitter design in Section 2.3 explore the efficiency drop-off. CPC fabrication is described in Chapter 4.

Chapter 2

HOLOGRAPHIC SPECTRUM SPLITTING

To move beyond the efficiency limits of single-junction solar cells, junctions of different bandgaps must be used to avoid losses from lack of absorption of low energy photons and energy lost as excited carriers thermalize to the semiconductor band edge. Over 40% of solar power incident on a single-junction solar cell is lost to one of these. [3] Spectrum-splitting photovoltaics mitigate these losses by incorporating multiple absorbers of different bandgaps. Tandem multijunction solar cell achieve high efficiencies but have challenges including current-matching and lattice-matching constraints and tunnel junction design required for each additional bandgap added. [4] Additionally high concentration makes thermal management challenging. Reference [6] has shown these factors can confer annual energy production advantages on collections of independently connected subcells. Such an arrangement is easier to achieve through lateral spectrum-splitting in which external optical elements are used to separate spectral bands. In addition to independent electrical connection, the thermal load of each cell is decreased by virtue of physical separation.

A common spectrum-splitting optical element is the Bragg stack. They are quite ideal spectrum-splitting optics as they can be designed to have sharp cutoffs in reflection and transmission to separate bands quite effectively without spectral band overlap, as can be achieved in tandem multijunctions in which subsequent cells are filtered by the absorption edges of higher bandgap cells. [8],[21] However depositing many dielectric layers of precise thickness is time-consuming and requires costly capital equipment. Holographic diffraction gratings, on the other hand, can be fabricated in a large area at high fidelity, motivating studies into holographic spectrum-splitting. High-efficiency designs demonstrating two-way splitting have been shown. [17]

Volume phase holograms have thicknesses much larger than their fringe spacings [22]. They can have diffraction efficiencies (intensity of total incident light to intensity of light going into the correct diffracted order) of up to 100% with low-absorption, low-scatter materials. In such gratings, the periodic index of refraction variation in the volume of the grating layer leads to phase differences in incident

light resulting in diffraction. Among diffractive optics available, holograms have the advantage of avoiding complex lithographic fabrication steps. Hologram fabrication (using the exposure of a recording material to an interference pattern between coherent light sources) allows large-area fidelity of recording, creating a low-scatter, high-performance diffractive optic.

2.1 Methods

We use Moharam and Gaylord's 1977 generalized coupled wave analysis (GCWA) to model the holographic gratings [23]. GCWA neglects second derivatives of the electric field associated with each diffracted order (a slowly varying field approximation). Additionally, reflected diffracted orders are neglected. This leaves a system of 1st order, coupled linear differential equations to solve. This method gives the diffracted intensity in those output diffracted orders that are retained in the calculation. In our calculations, transmitted diffracted orders -7 to +7 have been retained. This large number has been retained due to diffraction into progressively higher orders as the initially normally incident solar light passes through each grating stack.

The GCWA approach balances accuracy and computational expense better than more conventional choices. Coupled-wave analysis, considering only the input (0th order) and 1st order output is a valid approximation when the angle of incidence is near the Bragg angle and the grating is thick. In our case of stacked gratings and very broadband illumination, there will be much incident light that is far from the Bragg condition, and so we need a broader theoretical formulation to consider diffraction from our gratings. Rigorous coupled wave analysis, on the other hand, gives a more accurate solution (it is exact for a grating of infinite area when an infinite number of diffracted orders are used) but is computationally expensive.

To model the full compound holographic spectrum splitter, the output of each successive grating in a particular stack is found using GCWA for normally incident light. The intensity of normally incident light diffracted into orders -7 to +7 by the top hologram is calculated and those orders with greater than 0.01% diffraction efficiency are retained and become an input into the second grating in the stack. Similarly the output of the second grating becomes the input into the third grating. Finally, the output intensities and diffraction angles from the final grating are used to determine which underlying solar cell any particular output from the bottommost grating will hit. The total output fraction of input light intensity hitting each cell can

be converted to a photon flux using the AM1.5d spectrum to determine how many above bandgap photons are hitting each of the four tandem cells.

Holographic recording media

The holographic material is a key component of this design. We require low absorption and scattering over a broad wavelength range (300 nm - 1700 nm), high resolution, tunable properties, high diffraction efficiencies, and ease of processing. In addition to all this, incorporation into a solar application requires a long lifetime (>25 years), the ability to withstand high-intensity light without performance degradation, and resistance to the elements and to breakage. These criteria make dichromated gelatin (DCG) the top choice with its low absorption [24] and scattering and a wide range of index of refraction modulation (Δn). Common applications of DCG holograms include laser applications such as pulse compression, beam-splitting, and beam-combining, which require high light intensity exposure. DCG is hygroscopic and thus requires encapsulation. Additionally, the index of refraction modulation can vary from 0.01 to up to 0.4, but as this index modulation increases scattering into spurious diffraction orders also increases [22], so we have restricted the range of search from 0.01 to 0.06. Layers can be easily deposited and exposed at thicknesses less than 30 μm. All simulations used dichromated gelatin as the recording medium. Calculations assumed the refractive index of dichromated gelatin to be a constant value of 1.3 and the refractive index modulation to be sinusoidal. Edge effects in the holograms are assumed to be negligible.

DCG gratings are recorded on a substrate, in our case fused silica. During post-processing a superstrate is placed on top, and the edges are sealed with a moisture barrier for full encapsulation. The effective index of refraction of the DCG gratings is around 1.3 while the substrate, commonly fused silica or glass ranges from 1.45 to 1.55. The index of DCG during recording (before development), however, is 1.55. It is desirable to have an index-matched substrate during the hologram fabrication to avoid artifacts due to Fresnel reflections off the substrate during the recording process. Alternatively, having an index match during use in the grating stack reduces Fresnel reflections during the lifetime of the grating stack. This trade-off also incentivizes the use of holographic materials which can be better index-matched to available substrates and which do not require post-processing, which might alter their pre- and post-recording properties. There are holographic photopolymers, but none with the record of use or full set of desirable qualities of DCG.

Target spectral band selection and band gap energy dependent external radiative efficiency

Cell bandgap selection was done using a detailed balance model incorporating non-unity external radiative efficiency and non-unity current collection as variable parameters to approximate realistic cell performance according to [6]. We assume that only certain percentage of incident photons are absorbed and that the active materials have either a fixed external radiative efficiency (ERE) of 1% or 3% or a bandgap dependent ERE as described below. These de-rating factors account for losses such as non-radiative recombination and parasitic absorption and produce realistic cell efficiency estimates from the theoretical detailed balance calculation. The eight subcells of the four dual-junction solar cells shown in Fig. 2.5 have a combined de-rated detailed balance efficiency of 46.97% using these de-rated parameters of 90% absorption, 1% ERE for unconcentrated illumination and perfect spectral splitting. With a concentration of 100X this goes to 52.7%. The figure of merit for the splitting performance is the optical efficiency, defined as,

$$\eta_{optical} = \frac{System\ power\ with\ actual\ splitting}{Power\ with\ perfect\ splitting}, \tag{2.1}$$

where system power refers to the power obtained by independently connecting the four dual-junction cells and using DC-to-DC converters to combine the output current and voltage into a two-terminal output.

In order to appropriately select among available III-V semiconductor alloys, we extracted external radiative efficiency using experimental cell voltages. We used experimental data from our Full Spectrum Photovoltaics collaboration with Spectrolab lab as well as published data from Spectrolab [4] to extract external radiative efficiency using the reciprocity relation [25],

$$V_{OC} = V_{OC}^{rad} + kT\log(ERE), \tag{2.2}$$

where V_{OC} is the experimental open-circuit voltage, V_{OC}^{rad} is the open-circuit voltage expected in the radiative limit (internal radiative efficiency=1) according to the Shockley-Queisser detailed balance limit [1], k is the Boltzmann constant, and T is the cell temperature.

The simulated hologram output was propagated from the hologram output plane to the cell plane, and the output efficiency was weighted by the AM1.5D [26] spectrum to generate photon fluxes incident on each dual-junction cell. The iterative optoelectronic design process includes updating the ideal bandgaps of the four dual-junction cells to account for photon misallocation after design of the optical element.

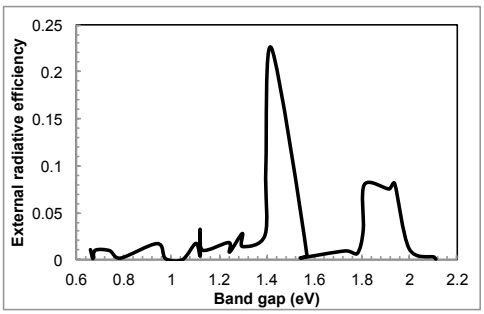

Figure 2.1: Band gap depdendent external radiative efficiency.

In order to re-optimize the subcell bandgaps based on the simulated input fluxes, the top cell bandgap was varied across all accessible values (0.7 eV to 2.1 eV) and used to find a corresponding current-matched bottom bandgap. We allowed thinning of the top cell if a current match could not be found without it. A lattice matching constraint that restricted both top and bottom bandgaps to either be above 1.41 eV or both below 1.34 eV was also implemented. The tandem pair generating the highest power of all was selected. Details of the target spectral bands are specified in 2.1.

Holograms were fabricated by Wasatch Photonics as a best effort to match our specifications. Angle-dependent transmission of the holograms was measured using the Scatterometry feature of a J. A Woollam VVase Spectroscopic Ellipsometer. The total collected light in these measurements were treated to remove Fresnel reflections from the front and back air/fused silica interfaces without anti-reflection coatings using 2.4.

Concentrating elements were simulated in commercial ray tracing program Light-Tools. Optimization was done by fixing the concentrator shape to an ideal compound parabolic concentrator (CPC) [20] with free parameters being the input angle, the trim, and input size. The output size was fixed at 1 mm as a minimum cell width. The CPC-height-to-cell-width ratio is set by the hologram diffraction angle and the CPC medium.

2.2 Results

Diffraction of a particular wavelength at a particular angle occurs at a given grating thickness, ϕ angle, refractive index modulation and grating line periodicity. If the grating thickness is modified from this optimum, the diffraction efficiency falls off. Similarly, as the diffraction efficiency falls off as the illumination wavelength changes from the design wavelength. All but the 0th order are dispersive, so the diffraction angle also changes with wavelength.

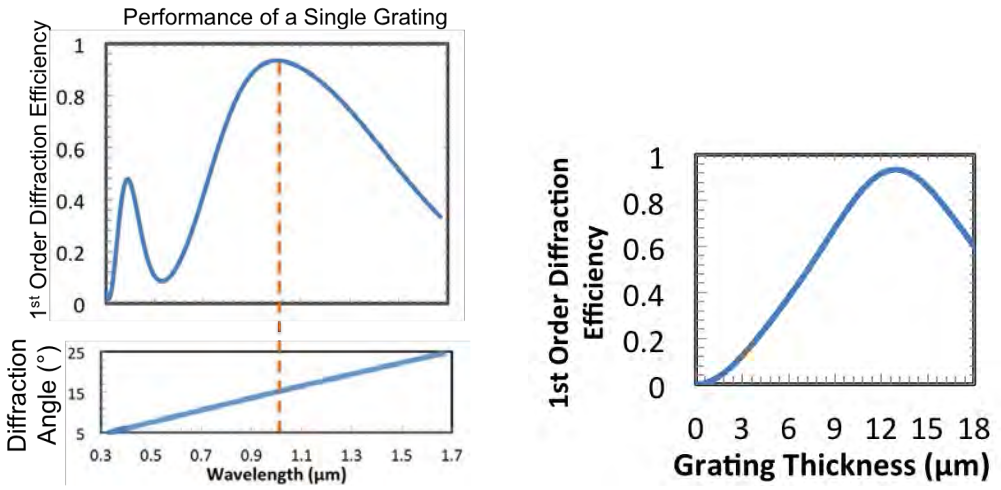

Figure 2.2: Diffraction efficiency and diffraction angle of a single grating as a function wavelength and grating thickness.

For a single grating, there is a minimum effective refractive index modulation for high diffraction efficiency for high first order diffraction efficiency. This is due to the thickness limit of dichromated gelatin holograms. As the diffraction angle increases, the effective path length within the grating increases and the maximum possible diffraction efficiency increases for the low modulation case. Also, because of this, the minimum needed refractive index modulation is higher for longer wavelengths.

Optimizing diffraction angle

For a given value of Δn there is a minimum effective thickness to get high diffraction efficiency. Thicker gratings and lower Δn give lower bandwidth diffraction peaks and likewise thinner gratings with higher Δn give higher bandwidth peaks. In order to select the primary diffraction angle which sets the aspect ratio of the holographic splitting module, the relationship between diffraction angle and diffraction efficiency was mapped. Fig. 2.3 shows first order diffraction efficiency as a function of first order diffraction angle, wavelength, and refractive index modulation Δn. Passing through a minimum effective grating thickness is needed for high diffraction efficiency. Effective thickness can be increased by increasing the diffraction angle or increasing Δn. For $\Delta n = 0.02$, the longer three wavelengths do not reach high diffraction efficiency, because the interaction between the incident beam and the grating is not enough to full couple the light into the first diffracted order. For higher values of Δn all wavelengths are able to couple into the first diffracted order with high efficiency when the first diffraction angle is between about 10° and 45°. Diffraction angles larger than 50° within dichromated gelatin will lead to diffracted

light being totally internally reflected if there is an air-encapsulant interface between the holograms and the cells. While larger diffraction angles enable a smaller aspect ratio, they also increase the spread of angles hitting the solar cells increasing the burden on the cell anti-reflection coatings to perform for a larger angle range.

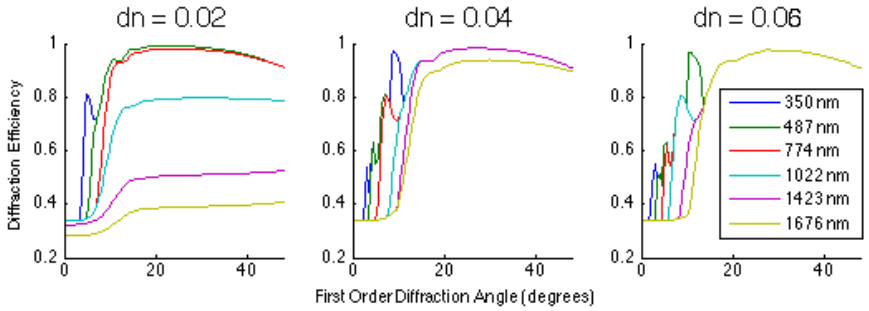

Figure 2.3: Peak first order diffraction efficiency for a given wavelength as a function of Δn, first order diffracted angle, and wavelength.

Two-way splitting design

We first consider the simpler problem of two-way holographic splitting using a single grating above each cell used to diffract the out-of-band light to the neighboring solar cell. As seen in Fig. 2.4, with only two single gratings placed one next to the other, intentional heuristic design is possible. In the top figure, two gratings are design to have their diffraction peaks aligned with the nulls of the other grating leading to diffraction peaks of light going to each cell at near unity. In contrast, if both gratings are diffracting in a certain wavelength range as is the case for short wavelengths here, poor separation occurs. In contrast, to this simple case, multivariate optimization is needed for the four-way splitter as the complexity is too high for a simple method. The greater number of subcells are needed, however, for the potential for high conversion efficiency.

2.3 Four-way holographic stack design

The Holographic Spectrum Splitter, shown schematically in Fig. 2.5, splits broad-band, incident sunlight into four spectral bands, each targeted at a dual-junction solar cell with bandgaps tuned to best convert the incident spectral band. The transmissive holographic spectrum-splitting optical element is composed of 12 individual volume phase holographic diffraction gratings arranged into four stacks of three gratings. Each grating in a stack is designed to primarily diffract one band of light toward one of the three solar cells in the cell plane which are not directly underneath the hologram stack. The fourth spectral band is intended to pass through the three

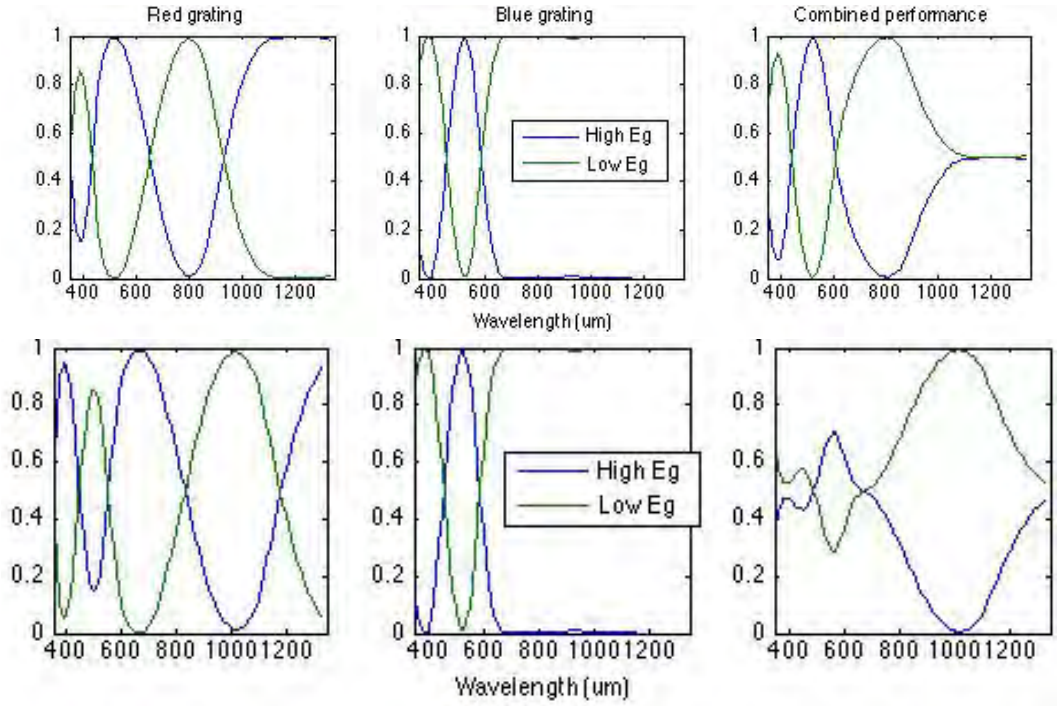

Figure 2.4: Plots show the fraction of light reaching either the high bandgap or low bandgap subcell in a two-way holographic splitter. The two left plots show results for two different designs for the 'Red grating' which sits above the higher bandgap subcell and diffracts longer wavelength light toward the lower bandgap subcell. The blue grating (center) is the same in both cases. When the fluxes hitting both cells are combined, the top grating pair is clearly complementary, while the bottom Red grating is a poor partner for the blue grating.

stacked gratings to the cell directly underlying the stack. Each grating stack sends the highest energy light incident on the stack toward the tandem cell designed for high-energy photons, and the lowest energy light incident upon it toward the right-most cell, designed for low-energy photons. The spectral bands and bandgaps of the top and bottom subcell in each tandem are given in Table 2.1. Lattice-matched III-V alloys can be found for each of these subcell pairs.

Band	Design λ (nm)	Bandwidth (nm)	Top bandgap (eV)	Bottom bandgap (eV)
1	487	300-674	2.1	1.84
2	774	675-873	1.6	1.42
3	1022	874-1170	1.23	1.06
4	1425	1171-1676	0.93	0.74

Table 2.1: Wavelength range of spectral bands

Each grating is designed for a particular wavelength within its spectral band. Holographic diffraction gratings have a decrease in diffraction efficiency as the wavelength deviates from this design wavelength as shown in 2.2. We aim to have the full width, half maximum of each diffraction peak equal to the desired bandwidth to get optimal diffraction of each band and minimize cross-talk between spectral bands.

Only the light at the design wavelength of a given grating will get diffracted to the correct angle. As the wavelength deviates slightly from the design wavelength, so too does the angle corresponding to the output diffraction order shift slightly. As the wavelength increases the diffraction angle increases. Thus in the spectral band in which 874 nm to 1170 nm light is to be diffracted 10 deg, the 970 nm light will go 10 degrees, the 874 nm light will go < 10 deg and the 1170 nm light will go > 10 deg. Thus most of the light is falling not just on the intended cell, but also onto one of its neighbors. Photons falling on cells with bandgaps to the blue of their energy will not be absorbed at all while photons falling on cells with bandgap to the red of their energy can get collected and generate some energy. Additionally the more energetic spectral band contains the most power, so it is most important that this band get to the correct cell. The extended structure of the array is a head-to-head, tail-to-tail arrangement, to minimize photons going to cells of completely different bandgaps. This dependence of output angle on wavelength and this extended geometry are accounted for in our holographic simulations.

The individual gratings have four design parameters shown in Fig. 2.5a: grating fringe tilt angle Φ, periodicity L, amplitude of index of refraction variation Δn, and grating thickness d. The individual gratings are encapsulated and combined into a stack using optical adhesive as shown in Fig. 2.5b. The idealized splitting of Stack 2, the second grating stack from the left is shown in Fig. 2.5c along with size ranges for various components and the optimized bandgaps for an ideal split of the AM1.5D spectrum [26]. The eight subcells are composed of group III-V semiconductor alloys, latticed matched to either GaAs or InP as growth substrates. Angle θ_1 is selected to be 10° based on simulations of single gratings subject to a maximum thickness of the holographic recording medium of 18 μm, the results of which are shown in Fig. 2.3. The diffraction angles θ_2 and θ_3 are calculated assuming four equally-sized tandem solar cells and constant distance between the cell plane and output plane of the holograms.

For highest efficiency, both high optical efficiency of spectrum splitting and concentration are required as seen in Fig. 2.7a. Fig. 2.7c shows the strong angle

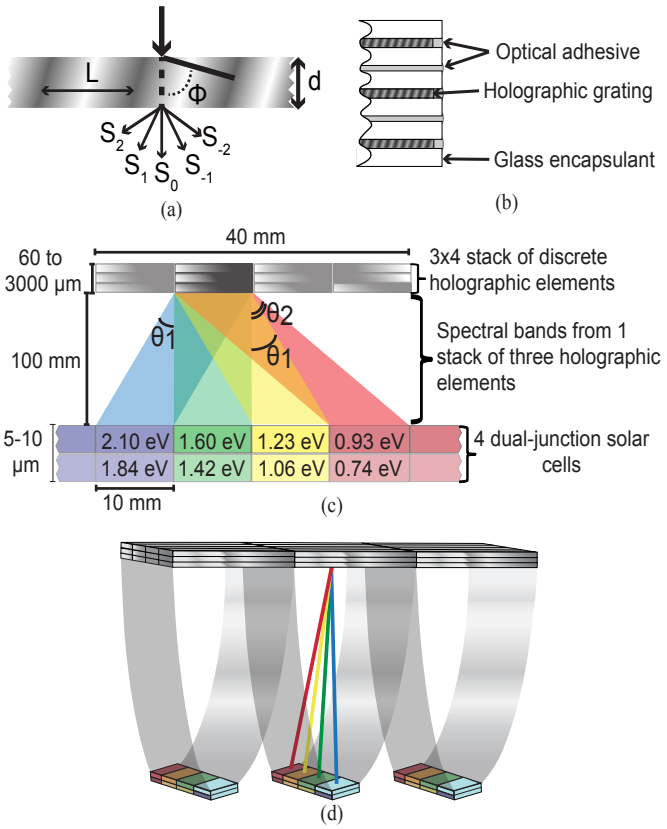

Figure 2.5: (a) Schematic of volume phase hologram of thickness d with write and gray fringes representing varying refractive index with periodicity L, tilted with respect to the grating normal by angle Φ. Normally incident light S_{inc} is split into a series of diffracted orders S_i.(b) Encapsulated holograms are glued into a stack of three with optical adhesive (c) Four stacks of three holographic gratings are assembled into a spectrum-splitting optical element. Each stack generates four spectral bands, one from each grating and a fourth that passes straight through the three-grating stack. Spectral bands are coupled into one of four high-efficiency III-V alloy, dual-junction solar cells tuned to best convert the target band of light. (d) Trough compound parabolic concentrators concentrate light after splitting in the direction orthogonal to frequency splitting. Individual spectrum splitting submodules tile to form a photovoltaic module.

sensitivity of the spectrum-splitting element, leading us to correspondingly design concentrating optics for a 1° acceptance half-angle. Concentration is incorporated orthogonal to the plane of spectrum splitting using a trough compound parabolic concentrator (CPC). Individual submodules can be tiled one next to the other into a module as shown in Fig. 2.5d.

Φ and L are chosen to fulfill the grating equation for the central wavelength of each spectral band for normally incident light.

Grating thickness and Δn were optimized by multiple strategies presented below.

Vary minimum diffraction angle for fixed index modulation

Despite the earlier result that higher refractive index was necessary for single gratings to achieve high diffraction efficiency, when combined into a 12-grating array which interfere with one another, lower modulation for each grating yields better overall results to avoid stronger interference effects.

Fix dn for all Gratings, pick d for central λ

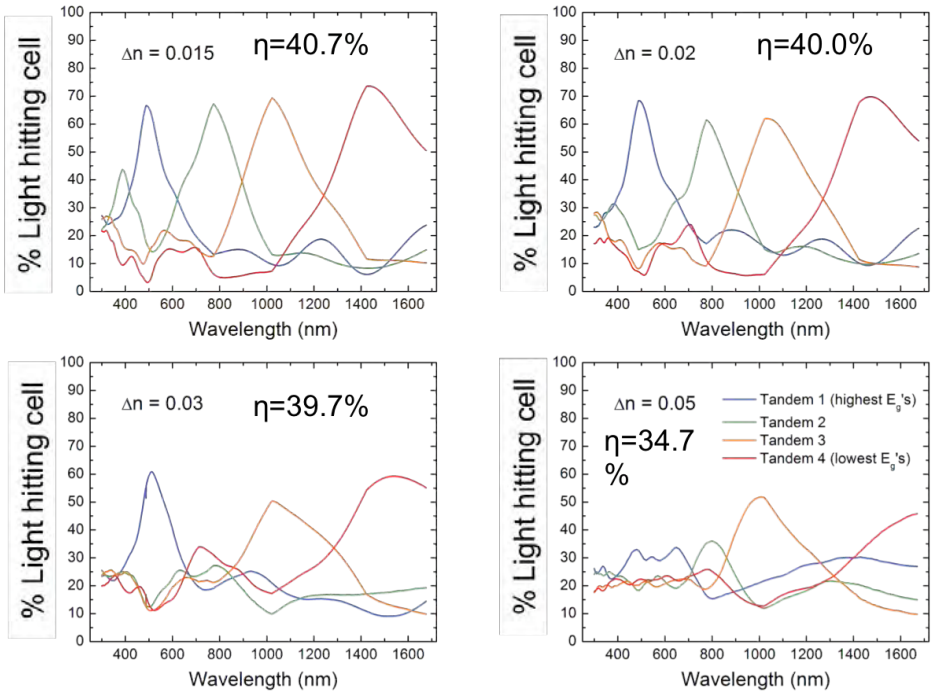

Figure 2.6: System performance for varying Δn.

The flux hitting each cell becomes the input to detailed balance calculations, which give a conversion efficiency for the sub-module. The grating model accounts for any misallocated photons due to the optics. The parameters of the holographic spectral splitter grating are given in 2.2. The index of refraction variation Δn=0.015 is used for all of the gratings. Recognizing that the optimal current matched tandem cells for the actual spectral bands generated from the splitting optics will not be the same as the best bandgaps for perfect splitting, the bandgap selection is re-optimized. This gives bandgaps of 2.24 eV/1.38 eV for the top cell, 1.74 eV/1.12 eV for the second highest, 1.36 eV/0.94 eV for the third tandem, and 1.06 eV/0.75 eV for the lowest energy tandem. These pairs are current-matched but not lattice-matched. Including

realistic cell performance with 90% absorption and 1% external radiative efficiency de-rating factors at the cell level and the splitting of the holographic stacks, the total system efficiency with the re-optimized bandgaps and 380x concentration is found to be 43.19%. The optical efficiency of these holograms is found to be 78.80%. A 5% loss due to Fresnel reflections between the gratings and their substrates, off the front face of the cells, and from the interface between the two CPC stages is assumed. A 2% series resistance due to electrical contacts and an additional 2% due to power conditioning electronics are assumed[27]. Finally the losses due to the concentrators are estimated to be 8.3%. All together the sub-module is expected to have a realistic efficiency of 36.14%.

Vary dn, pick d for central wl

The grating thickness was selected to maximize the diffraction efficiency of the central wavelength going into the first diffraction order for a given Δn. A parameter sweep was done over Δn values and over the order of the three gratings in each stack to optimize the value of a figure of merit which power weights the percentage of photons hitting the correct subcell. We define it as

$$FOM_i = V_i \times flux_i(\lambda) \times \eta(\lambda), \tag{2.3}$$

where i is the spectral band, V_i is a lower bound for open-circuit voltage of subcell i estimated by the bottom bandgap of the subcell minus 400 meV, $flux_i(\lambda)$ is the portion of the AM1.5D spectrum in band i, and $\eta(\lambda)$ is the fraction of in-band incident light reaching the solar cell.

This figure of merit was evaluated over 58 wavelength points over the solar spectrum (300 nm-1700 nm) with 24 nm spacing. Δn was varied between 0.01 and 0.06 by 0.005 for stacks 1 and 2 and between 0.015 and 0.055 by 0.01 for stacks 3 and 4 yielding up to 11 possible values. Additionally, the three gratings could be stacked in six possible permutations giving $\leq$7986 configurations for each of the four grating stacks. Each parameter combination was evaluated, and the results were sorted by the figures of merit of the stacks. The output fluxes of the eight best parameter combinations for each stack were combined giving $8^4 = 4096$ combinations which were evaluated using a detailed balance re-optimization of the bandgaps for the actual flux hitting each cell (described in Section 2.1). The twenty best parameters sets for the holographic splitting element were then simulated with wavelength spacing of 1 nm. Through this process, an optimized set of grating specifications, given in Table 2.2, was determined. The resulting spectral separation is shown in Fig. 2.7b,

where the fraction of incident light hitting each of the four subcells is shown along with dashed vertical lines showing the position of the absorption cutoffs for the top and bottom solar cells re-optimized for the actual flux they are receiving under the holographic splitting element. The bandgaps are also given in Fig. 2.7d.

Table 2.2: Optimized holographic splitting element grating parameters

	λ_c (nm)	Φ (°)	L (μm)	d (μm)	Δn
Stack 1	1423	-77.0	2.43	18.0	0.01
	1022	-80.6	2.40	17.1	0.03
	774	-85.0	3.42	18.0	0.015
Stack 2	487	85.0	2.15	16.1	0.015
	1022	-85.0	4.51	18.0	0.015
	1423	-80.6	3.34	18.0	0.03
Stack 3	487	80.6	1.14	4.4	0.055
	1423	-85.0	6.28	18.0	0.045
	774	85.0	3.42	18.0	0.015
Stack 4	487	77.0	0.83	4.5	0.055
	1022	85.0	4.51	18.0	0.015
	774	80.6	1.82	18.0	0.015

Experimental Results

The holographic recording medium, dichromated gelatin, is hygroscopic and must be encapsulated for the holographic diffraction grating to persist. The holographic gratings fabricated here are sandwiched between 1 mm fused silica slides with Norland Optical Adhesive as an edge barrier, as illustrated in 2.5b.

The three gratings of Stack 1 were fabricated, and the diffraction efficiency of each grating was measured as a function of diffraction angle and wavelength. Fig. 2.8 shows the diffraction efficiency of each order for the four fabricated gratings with $\lambda_c = 1022\ nm$. In addition to the diffracted orders, the summed transmission is shown at the top. At the peak of the first order diffraction efficiency, all transmitted light is going into the first diffracted order. In contrast the grating designed for $\lambda_c = 1423\ nm$ was optimized into invisibility. This is most evident in comparing the simulated flux going through Stack 1 to each of the four tandem subcells with and without the $\lambda_c = 1423\ nm$ shown in Figure 2.9. Given the realistic losses associated with passing through an additional grating layer, the final experimental results presented here exclude this grating and focus on a two-grating stack.

Total transmission and specular reflection measurements of the fabricated gratings were also taken. Fig. 2.10a and 2.10b show color plots of diffraction efficiency

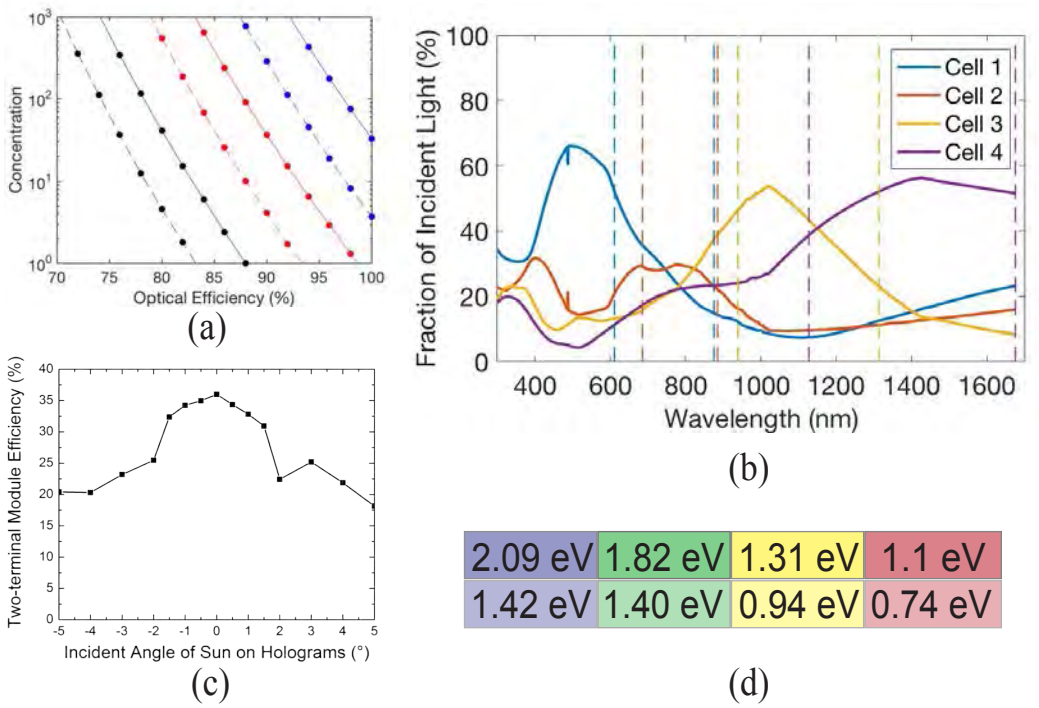

Figure 2.7: (a) Contours of 40% (black), 45% (red) and 50% (blue) module efficiency for aggressive cell performance targets (solid) of 3% ERE and 92.5% of ideal absorption and moderate cell performance targets (dashed) of 1% ERE and 90% of ideal absorption as a function of optical efficiency of spectrum splitting, concentration, and cell performance, (b) Percentage of incident light hitting each of the four tandem solar cells after passing through optimized holographic splitting element. Vertical lines correspond to the re-optimized bandgaps of the dual junction solar cells that optimize device performance for the actual incident flux hitting each solar cell, (c) Holographic splitter and concentrator performance as a function of incident angle. A tracking accuracy of 1° is sufficient to retain >93% system performance. (d) Re-optimized bandgaps of four dual-junction cells based on actual spectral bands from (b).

versus wavelength and diffraction angle for the experimental and simulated grating stacks, respectively. In order to isolate the spectral match-up of the simulated and experimental gratings, scattering and absorption losses were extracted from total transmission measurements and added to the simulated results as described in the Methods Section. Additionally, polarization averaged normal incidence Fresnel reflections from the front face R_f and diffraction-angle dependent Fresnel losses from the back interface R_b were removed from the measured transmission results T_m to get the Fresnel corrected transmission T_c from

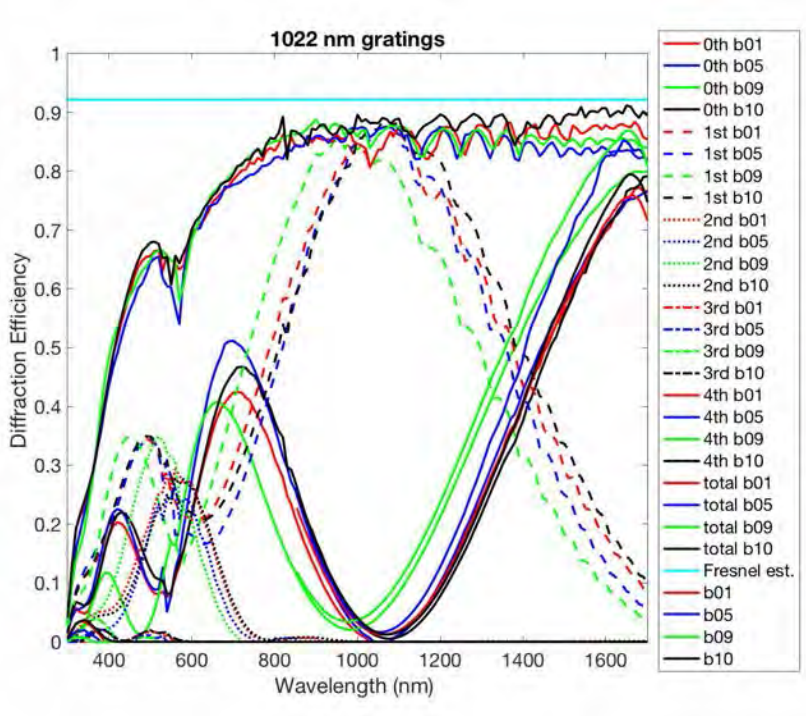

Figure 2.8: Measurement results for four $\lambda_c = 1022\ nm$ gratings. Each color represents a different grating and each line style shows a different diffracted order. The cyan line at 0.92 represents a rough approximation of expected Fresnel reflection loss.

$$T_c = \frac{T_m(\lambda, \theta)}{(1 - R_f(\lambda)) \times (1 - R_b(\lambda, \theta))}. \tag{2.4}$$

This dataset, like for the simulation results above, was converted from intensity as a function of wavelength and angle leaving the hologram plane to flux hitting the subcells by propagating the diffraction efficiencies to the cell plane and weighting by the AM1.5D reference spectrum. The fraction of photons hitting subcells 1 to 4, where 1 is the highest bandgap tandem and 4 the lowest bandgap tandem, determined by simulation and experiment with correction are presented in Fig. 2.10c-f, respectively, along with total transmitted light in both cases shown in Fig. 2.10e.

Concentrator Design

The holograms are sensitive to the angle of incidence of light, and this sensitivity is increased when stacking holograms, which act in concert. Thus, they must be incorporated into a tracker. The submodule performance drops off significantly for

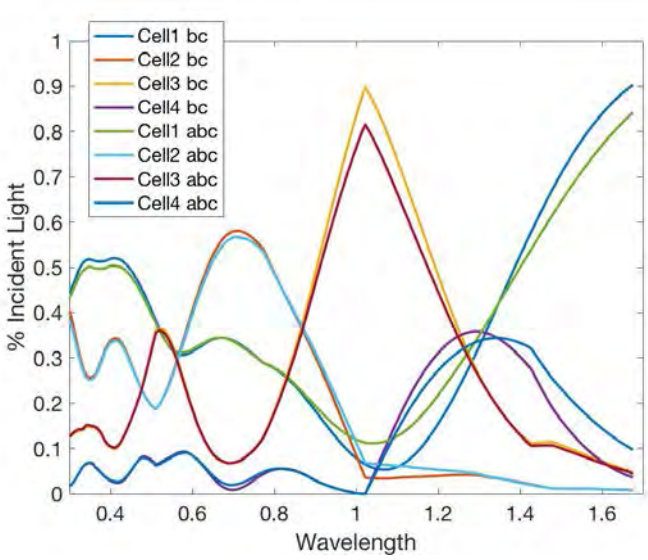

Figure 2.9: Fraction of light going into each subcell versus wavelength. The discrepencies between the two stacked gratings (bc) and the three stacked gratings (abc) are minimal.

light incident at a deviation of greater than 2° from normal. This angular sensitivity is similar to that of high-concentration optics. Since using angle-of-incidence sensitive diffractive optics requires tracking of the sun and use of only the light in the direct solar spectrum rather than the global solar spectrum, concentration allows both a compensation for the diffuse light lost as well as the potential to access much higher overall efficiencies.

Increasing concentration, holding all else constant, improves efficiency. Additionally, concentration allows smaller active device areas and thus lowers cell costs. Non-imaging optical elements allow concentration that can reach thermodynamic limits [20]. A compound parabolic concentrator (CPC) takes any light incident on its input aperture within a certain half-angle (its acceptance angle) from the normal and reflects it to its output aperture. In the concentration scheme used for the holographic splitter (2.5), the top CPC is a curved, silvered mirror, which concentrates light orthogonal to the direction of spectral splitting. The secondary CPC is concentrating in two directions with rectangular input and output apertures. It is solid and made of a high-index polymer (n=1.65) giving an n^2 enhancement in the concentration relative to a hollow CPC with the same acceptance angle. The reflection at the surface of the CPC is due to total-internal reflection at the polymer-air interface. The rectangular shape comes from intersecting two trough CPC profiles. The inset shows the shape of the secondary concentrator. The corners add some loss

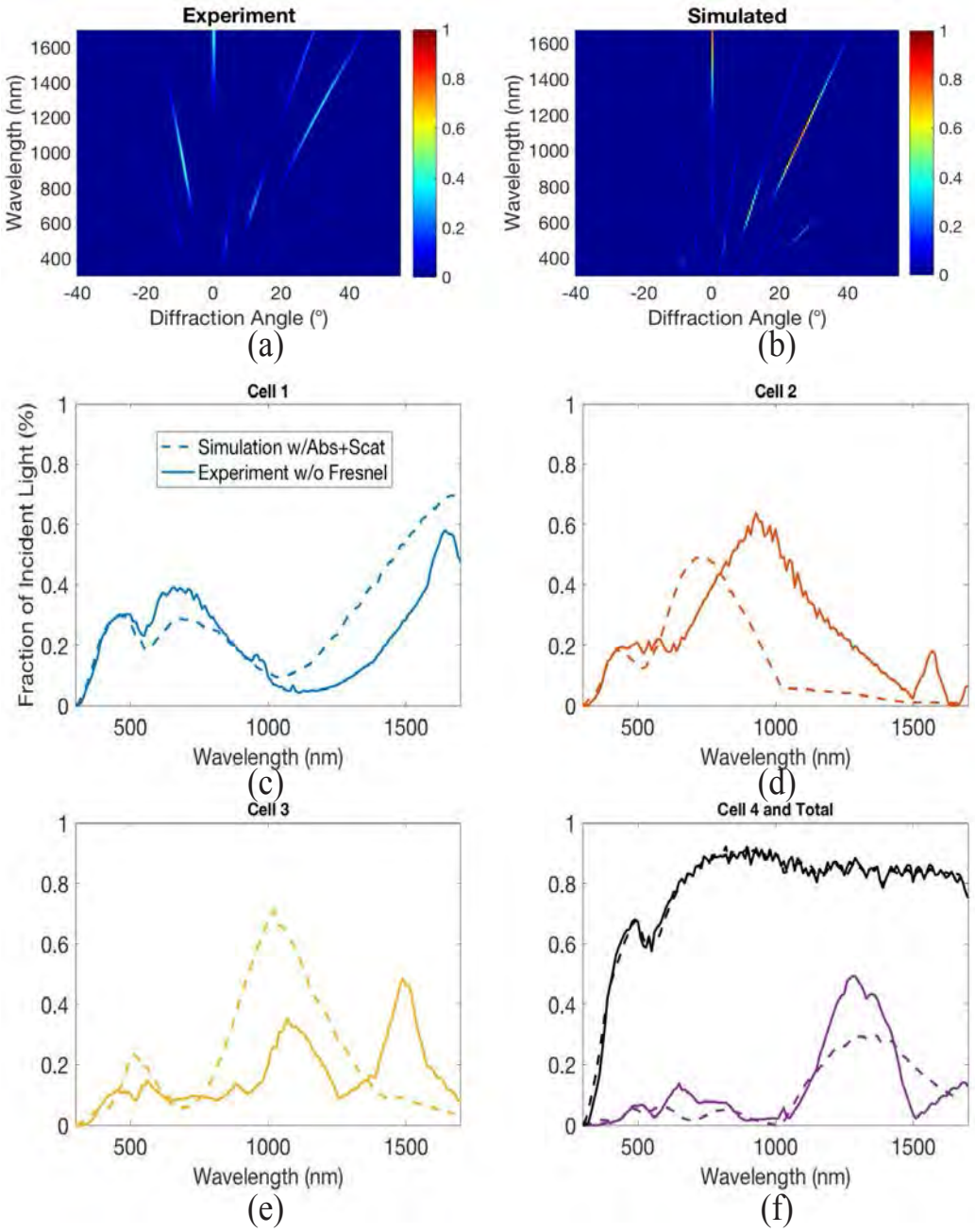

Figure 2.10: Color plots showing spectral and angular spread of (a) measured and (b) simulated light going through one grating stack (Stack 1). (c-f) Fraction of light hitting each solar cell after passing through the grating stack in simulation (dashed) and experiment (solid) with Cell 1 as the highest bandgap tandem and cell 4 being the lowest bandgap tandem. (f) additionally shows the total light transmitted through the stack.

relative to a trough that concentrates in only one direction. The optimum output to the cells accounting for both increased concentration and increased loss from the

concentrator must be balanced.

We use trimmed trough compound parabolic concentrators (CPC) as concentrating elements in the direction orthogonal to the spectrum-splitting direction [20]. The angular spread of light exiting the concentrator is limited to 50° using a conical section at the CPC output to minimize Fresnel losses at the cell/concentrator interface. The spectrum splitting itself incorporates an additional factor of 4X concentration. A hollow, silver-coated trough, solid quartz, and solid PMMA trough CPC were optimized. Total concentration and transmission efficiency of the external concentrator are given in 2.3.

The concentrator transmission efficiency and the simulated photon flux hitting each subcell are used to simulate module efficiency. We account for losses including misallocation of light due to the holographic spectrum splitting, Fresnel reflection loss, non-unity external radiative efficiency of the solar cells (detailed in Section 2.1), imperfection collection of incident light on the cells (92.5%), 98% power conditioning efficiency [27], and 2% series resistance loss. For the front air-fused silica interface, the normal incidence reflectivity of an optimized anti-reflection coating is assumed to be 99% across the solar spectrum. At the back air-fused silica interface with an additional need for anti-reflection for a broad angle range, a reflectivity of 98.5% is assumed. Finally at the cell input face an angle and spectral averaged transmission of 97.5% is assumed for a total of 5% Fresnel reflection losses. The optical adhesive used to glue the three gratings into a stack is assumed to be perfectly index matched and lossless.

The range for projected experimental module efficiency comes from averaging the total transmission of all the fully characterized experimentally made holograms, correcting for Fresnel reflections, and using the corrected average total transmission as a proxy for all unaccounted for losses. This maximum transmission cubed was applied to the simulated fluxes to give the bottom end of the range and this factor squared and applied to ideal spectral bands gives the top end of the range.

2.4 Discussion

Individual grating diffraction profiles of volume phase holograms can have quite high peak diffraction efficiency at the intended angle and design wavelength. This is evident in Fig. 2.8 at its peak all light transmitted through the $\lambda_c = 1022\ nm$ grating is going into the first diffracted order. As the incident angle or wavelength varies, however, the diffraction efficiency decreases smoothly in either direction.

Table 2.3: Simulated and projected module efficiency

Configuration	Concentration	Concentrator efficiency	Simulated module efficiency	Experimental efficiency projected
No external concentration	4X	100%	35.2%	
hollow trough CPC	101.3X	96.0%	36.8%	27.2%-39.5%
solid quartz trough CPC	121.2X	97.4%	37.54%	27.8%-40.2%
solid PMMA trough CPC	19.0X	95.4%	34.93%	

Additionally, diffracted orders (as opposed to the directly transmitted beam) are dispersive. As such, the angle at which light is diffracted varies as the wavelength varies. Both of these factors lead to the sloped fraction of light profiles in 2.7a and 2.7b, and thus the overlap of top and bottom bandgaps of adjacent tandem subcells bandgaps after re-optimization for actual splitting. This smeared out partial separation limits the amount of thermalization loss that can be compensated by converting higher energy photons in higher band gap cells and vice versa. A more ideal spectrum splitting element would have a more square reflection profile with sharper cutoffs. Reference [28] has shown that incorporating some concentration immediately below the hologram plane of a single holographic elements allows this problem to be partially overcome.

The current design for four-way splitting based on three stacked gratings and four dual-junction solar cells was motivated by pursuit of >50% module efficiency. Given the currently achieved design with losses originating mainly from optical losses it is possible that a redesign cutting the number of gratings or spectral bands would result in sufficiently higher optical efficiency to give a net efficiency benefit to a less ambitious design. As an example a two-way splitting design is presented in the supplementary information.

The experimentally fabricated hologram stack represents a first prototype rather than the best possible outcome. After absorption, scattering and Fresnel reflection losses are reconciled between simulated data and experimental data as described above,

the most notable difference between the simulated stack results and the experimental results is a negative order peaked around 900 nm which pushes much light intended for cell 3 into cell 2. Measurements indicate this spurious order to be due to diffraction of light by the third grating which enters grating 3 in the first diffracted order of grating 2. While simulations accounted for such cross-talk, this diffraction, present in the experiment and not the simulation, indicates a deviation between the experimental and simulated results. Iterating the fabrication process should better reconcile the experimental results to the intended designs. For this reason, in making the projection for experimental module efficiency, we apply the Fresnel-corrected average transmission of the experimental gratings. This way, we incorporate losses such as grating scattering and absorption but not spectral mismatch between the simulated and fabricated gratings. The lower end of the projected range is the three-grating correction applied to the simulated fluxes while the high end of the range is the two-grating correction applied to ideal splitting.

The degree of concentration incorporated for the different concentrator types is constrained by many factors. For the solid quartz trough, weight is the primary concern. We limit the height of the concentrator to about 27 cm, giving an eventual module height of about 30 cm. For the solid PMMA trough, the height is significantly limited by absorption in the polymer. The height in this case is limited to 0.7 cm giving a power weighted solar absorption of 3.3% in the concentrator material. On the other hand, the hollow silver-coated trough CPC incurs metal absorption losses rather than volumetric losses, so the height is much larger 17.3 cm. However, the higher transmission efficiencies are for a higher degree of trim as less light hits the silver surface at very shallow, grazing incidence, minimizing absorption to 2.7%.

The optical efficiency of the concentrator is the key determiner of improved system efficiency. While 100% efficiency 90X concentrator and a 90% efficiency 100X concentrator give an equal current density at the cell plane, the former is much preferred from an overall energy conversion standpoint. Concentrator transmission losses directly cut down on cell current and thus also cell voltage. Thus increasing the degree of concentration at the expense of the transmission efficiency of the concentrator does not pay off for system efficiency.

Conclusion

Transmissive, volume phase holograms were explored as a spectrum splitting optical element. Optical recording confers benefits of avoiding mechanical fabrication

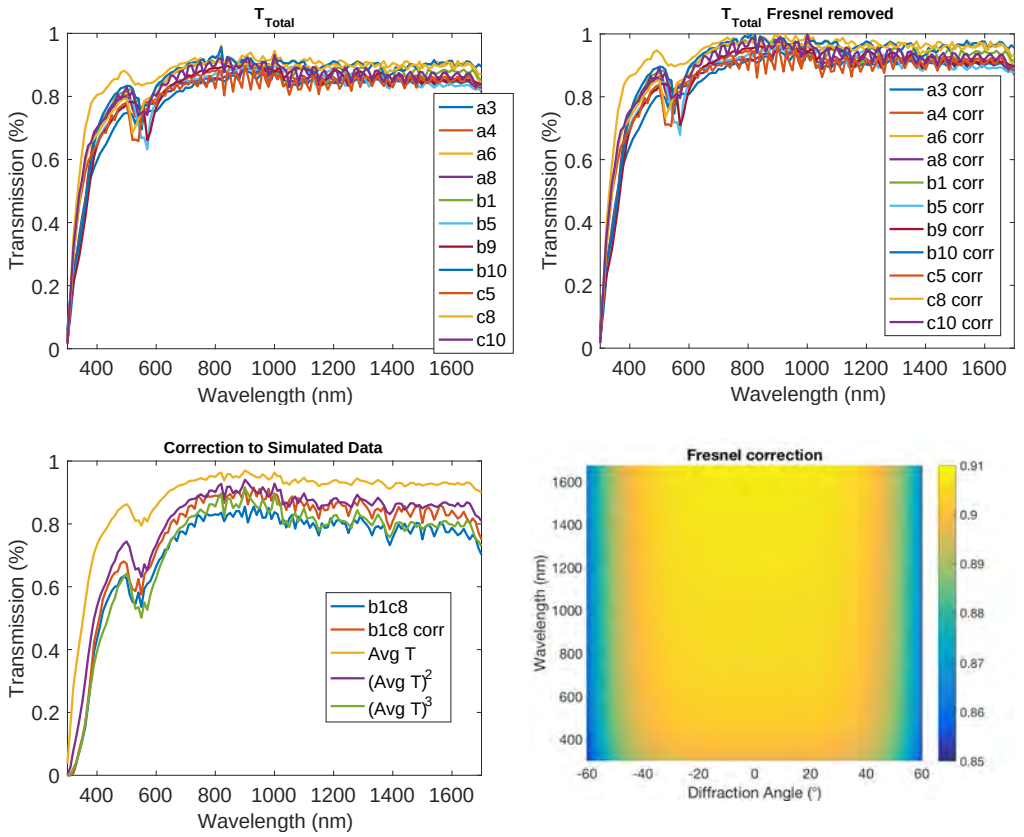

Figure 2.11: (top left) Total transmission as a function of wavelength for 11 fully characterized experimentally fabricated gratings. (top right) Total transmission treated with Fresnel correction (two normal-incidence air-glass interfaces). (bottom left) Average transmission through the eleven experimentally fabricated gratings after Fresnel correction applied plotted with this same transmission squared and cubed to approximate transmission through two and three-grating stacks. Also shown are the transmission and Fresnel corrected transmission for the two-grating stack. (bottom right) Fresnel reflection correction applied as a function of wavelength and diffraction angle.

defects. Additionally, these gratings can funnel all diffracted light into a single diffracted order for a single wavelength and diffraction angle. A holographic spectrum splitter design is presented which uses four stacks of three gratings each. Separated light hits one of four dual-junction solar cells for a total of 8 bandgaps. Grating simulations use generalized coupled wave analysis to track normally incident broadband light as it passes through and is diffracted by each grating in the stack. Simulated module efficiencies for this design can hit 37% including reflection, electrical, non-unity radiative recombination, and non-unity current collection losses.

Experimental demonstration of one of four three-grating stacks shows a fair match with simulated targets. It sets a lower bound for experimental realization of the design, since no iteration was done on the gratings. The experimental data are used to extract a spectrally dependent grating transmission function which is used to project a lower bound efficiency for a fully realized module.

Currently, the best simulated efficiency designs match current experimental records for lateral spectral splitting and for traditional tandem multijunction CPV modules. Thus future design efforts should focus on bringing up the efficiency even further. Incorporating lenses to decrease deleterious effects of dispersion in diffracted orders could improve efficiency significantly. Additionally, given the experimental measurement of grating losses, decreasing interface reflections and iterating on the hologram design toward a parameter set which transmits more light across the spectrum is necessary.

Chapter 3

POLYHEDRAL SPECULAR REFLECTOR

The goal of the Full Spectrum Photovoltaics Project was to design and prototype a 50% module efficiency photovoltaic system. Of the three designs we initially pursued, the Polyhedral Specular Reflector (PSR) design came closest to achieving this goal. In targeting this efficiency record, our design evolved over time as we fleshed out our device models and gained new information.

The initial estimate from Emily Warmann's detailed balance modeling was that we would need to to incorporate eight single-junction III-V subcells for 50% efficiency. The initial design, shown in Figure 3.1a, was inspired by Reference [12]. Largely collimated light entered the device via a primary trough concentrator and hit a series of solar cells tiled along the sides of a parallelepiped angled at 45° to the direction of light incidence. It was noted that the lowest bandgap cell contributed only 0.5% of the power to the device, so it was decided to eliminate it and have a seven-way split instead. The 7th cell would be attached to the bottom of the parallelepiped instead of on the side. The bandgaps of the seven chosen subcells are listed in Table 3.1. Next, we saw that the limit on concentrating in only one direction was lower than the degree of concentration needed for our target high efficiency, especially if the angular spread entering the parallelepiped was to stay low so the trough concentrator was changed to a primary square CPC as shown in Figure 3.1b.

The simplest version of this design uses the cells themselves as absorption filters with their back-reflectors as mirrors. Broadband light enters the structure, enters the highest bandgap subcell where the above-bandgap light is absorbed. The remainder is reflected by the back reflector to the 2nd highest bandgap subcell and so on. However, in each cell there is some small amount of loss of below-bandgap energy light. Simulations were done assuming 5-10% parasitic absorption of out-of-band light. The efficiency of the structure was not high enough, so we opted to include short pass filters on the front of each of the seven solar cells. Thus the filter would reflect all out-of-band light before it entered and experienced parasitic absorption in the cell while the target band would be transmitted. The filters were designed to be short-pass filters so that any high energy light that failed to be transmitted and collected in the highest bandgap cell could still be transmitted and converted in one

of the lower bandgap cells. This way, instead of being lost completely, it might simply produce lower voltage than if collected in the correct cell. This was dubbed the Generation I design.

Designing Bragg stacks with short wavelength pass-bands which simultaneously reflected light all the way to 1676 nm for the seventh subcell with bandgap E_g = 0.74 eV proved very difficult. Decreasing angular spread on the filters improved efficiency, but there is a need for concentration for both high performance and acceptable cost. Thus the primary concentration was decreased and we incorporated secondary compound parabolic concentrators between the filter and cell creating the Generation II design which had a multipart secondary receiver at each of the seven positions as shown in Figure 3.1d. The concentrators were cut at a 45° angle for incorporation. Fabrication and characterization of the concentrators is discussed in Chapter 4. This is the Generation II PSR.

The performance of the Generation II filters was still not high enough to achieve 50% module efficiency. In response, the Gen. II filter order was modified so that the lowest bandgap subcell came first. With this changed order the first subcell was the 0.74 eV cell followed by the six other cells in order of decreasing bandgap from 2.11 eV to 0.93 eV. The first filter could then be a long-pass filter, and the second filter with the broadest reflection band must reflect from 589 nm to 1333 nm rather than 589 nm to 1676 nm in the original order.

Despite the improvement over the Generation I filter design, getting sufficient performance from the one long-pass and six short-pass filters still required many inconvenient design compromises. First, it was necessary to remove the primary concentration to reduce the angular spread on the filters. Second, without primary concentration, the only way to tile the PSR submodules into a module is via vertical offsets equal in height to the PSR height as shown in Figure 3.1c. This would in very tall, unwieldy modules. Third, the lack of a common plane for the cells meant we would need to somehow contact and heat sink seven physically separated cells. Finally, the hollow PSR cavity required high quality anti-reflection coatings for both the filters and the cells.

To address these practical and performance challenges, the Generation IV design was developed (Figure 3.1e). Given that long-pass filters are easier to make, all the filters were converted to long-pass filters placed at a 45° angle to the incident lightpath. Each reflected frequency band is directed perpendicular to the lightpath, allowing a common plane for the cells allowing easier integration. The long-pass

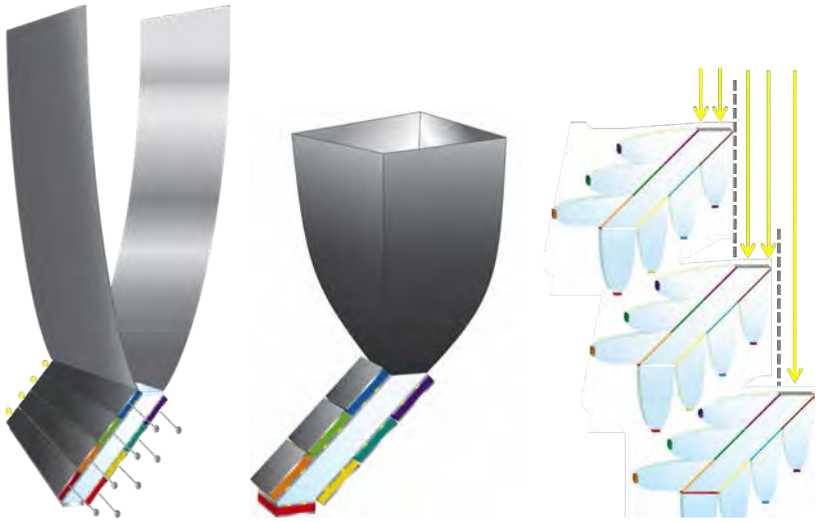

(a) Original Concept (b) Generation I (c) Vertical Offset

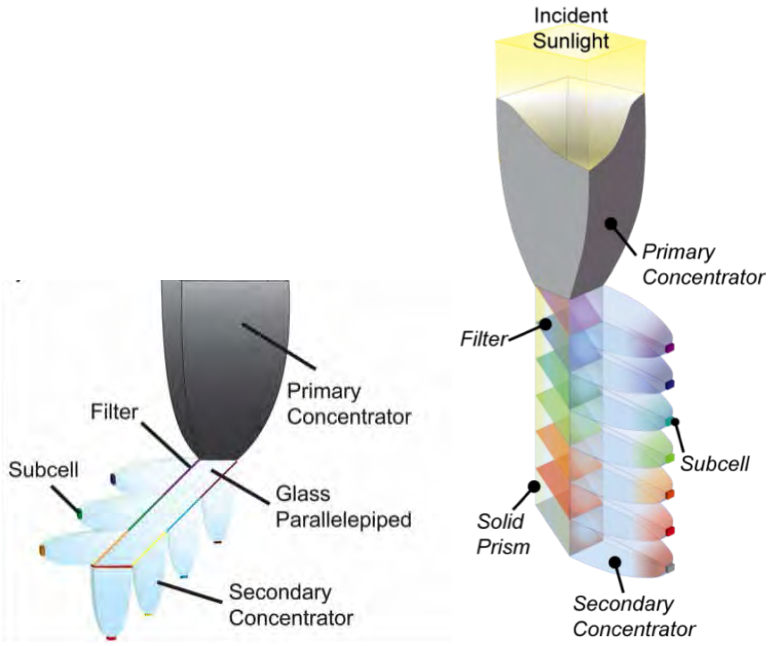

(d) Generation II (e) Generation IV

Figure 3.1: Polyhedral Specular Reflector design schematics.

filters can be designed to be embedded in an $n \approx 1.5$ medium with some degree of primary concentration simplifying ARC design and tiling of the submodules into modules. The final change made to the PSR design during prototyping was to change the secondary concentrators from PDMS CPC to glass lightpipes. This change was made because the long optical path length of PDMS absorbed too much light and finding a method or vendor to fabricate the CPC curvature in glass proved elusive.

Further design changes to make the PSR concept a viable commercial photovoltaic technology are discussed in Section 5.2.

Receiver	Subcell E_g (eV)	Gen IV filter reflection band	Subcell Alloy
1	2.11	350 – 588 nm	$Al_{0.20}Ga_{0.32}In_{0.48}P$
2	1.78	589 – 697 nm	$Ga_{0.51}In_{0.49}P$
3	1.58	698 – 785 nm	$Al_{0.1}Ga_{0.9}As$
4	1.42	786 – 873 nm	$GaAs$
5	1.15	874 – 1078 nm	$In_{0.87}Ga_{0.13}As_{0.28}P_{0.72}$
6	0.93	1079 – 1333 nm	$In_{0.71}Ga_{0.29}As_{0.62}P_{0.38}$
7	0.74	1334 – 1676 nm	$In_{0.53}Ga_{0.47}As$

Table 3.1: Wavelength range of spectral bands for the PSR design and Generation IV design filter specifications

Coupled Optoelectronic Model

In order to get a full sense of the efficiency potential of the PSR, our team coupled a series of simulation tools. Dr. Emily Warmann used available databases of solar resource data including the NREL Simple Model of the Atmospheric Radiative Transfer of Sunshine (SMARTS) resource [29] and National Solar Radiation Database (NSRDB) [30] to create a dataset of 365 days of annual solar irradiance in a variety of locations across the US to estimate annual energy production. [6] Dr. Carissa Eisler used an open-source transfer matrix method optimization software OpenFilters to design Bragg stacks for the PSR as well as anti-reflection coatings (ARC) for each of the seven solar cells. [31] The filter and ARC optical characteristics were then integrated into a ray tracing program (LightTools) to optimize the degrees of primary and secondary concentration and to determine the incident photon flux on each solar cell in the integrated PSR. The spatial distribution of the photon fluxes were used by Cris Flowers using an HSPICE based distributed circuit model to design an electrical contact grid to minimize fraction of the solar cells shadowed by the metallic front contacts while also limiting series resistance losses. The resulting data for integrated device peak efficiency and annual energy production were used to evaluate our progress toward 50% module efficiency. Additionally, these technical data were used in conjunction with cost modeling, described in Chapter 5, to project $/W and LCOE for the PSR at high-volume production.

PSR Prototypes

We made a number of prototypes of the PSR design throughout the project. The first two were prototypes of the Generation I design, made with six of the seven

intended subcells (all but the 0.74 eV). This was done using commercially available long-pass filters. The cells were designed using open-source 1D device physics solver AFORS-HET [32], were grown by a semiconductor and were processed into devices at Caltech. The prototype efficiency measured 11%. Figure 3.2a shows this design. Generation 2 was not prototyped, and only partial prototypes were made of the Generation III design. Figure 3.2b shows a 3D printed mechanical prototype of Generation III. The green collars connect the CPC tips to photodiodes mounted on small, yellow pieces of printed circuit board which would both mechanically support the cell and allow for electrical interconnections. Figure 3.2c shows a partial optical prototype of this design. The first long-pass filter and the first two short pass filters are shown with concentrators attached. Normally incident red and green light from laser pointers is appropriately separated. The green light is reflected off the longpass filter, passed through the second filter, and concentrated where the 2.1 eV cell would be in a full prototype. Likewise, the red laser light is predominantly reflected by the first two filters and passed into the third concentrator. The fact that the laser beam paths are visible going through the concentrator is indicative of surface and volume scattering.

Three Generation IV prototypes have been built, and the final prototyping effort is currently underway at the time of writing. The solar cell epitaxial layer growth was done by Boeing Spectrolab while processing of wafers into devices including epitaxial lift-off was done in our labs by John Lloyd. The optical path was composed of six parallelepiped pieces with filters deposited on one face each and a seventh triangular piece to give the flat input aperture. These seven pieces were each masked using Kapton tape and adhered using PDMS. The tape prevented the PDMS from running up the sides of the structure creating scattering points for light that should be totally internally reflected at optically smooth interfaces. A similar tape masking and PDMS gluing process was used to attach the seven concentrators to the appropriate faces of each parallelepiped piece after the main optical splitting structure had been assembled, resulting in the prototype shown in Figure 3.2d. The optical characterization results for the PSR train with 194X PDMS secondary concentrators and 1.7X primary concentrator are shown in Figure 3.3. While the filter train alone has high optical efficiency, the PDMS concentrator efficiency is 60-70% and the integrated CPC have alignment errors contributing additional losses. The overall optical efficiency of this structure is thus slightly above 60%.

The next Generation IV prototype used 16X glass lightpipes (Figure 3.2e), which

gave much higher optical efficiency than PDMS CPC. The incident photon collection efficiency averaged 73%. Its spectral dependence was also very flat as shown in Figure 3.4. The overall submodule efficiency was found to be 22.9%. Losses included a variety of optical, cell and integration related issues. The cell voltages and degree of concentration were lower than simulated. Due to all seven subcells not yet being ready, 0.74 eV bandgap cells were incorporated at each of three lowest bandgap locations, and similarly a 1.54 eV cell in place of the intended 1.78 eV cell.

Many of these concerns were addressed in the most recent prototype which used 100X long lightpipes in place of the 16X short lightpipes (Figure 3.2f). However, the small size of the subcells created a new loss source. The alignment of the 1 mm^2 subcells at the bottom of the 10 cm long lightpipes proved difficult, and misalignment and light leakage at the cell-PDMS-lightpipe interface decreased photon collection to 53%. Thus, despite incorporating the seven correct subcells which much improved performance, the overall submodule efficiency dropped slightly to 22.4%. The simulated efficiency of the long lightpipe PSR with subcells hitting their performance targets is 47%. The current prototyping effort incorporates improved cells as well as an improved alignment procedure for attaching the subcells to the end of the 100X lightpipes. Hopefully this last prototype will far surpass the previous prototypes and approach or beat today's spectrum splitting submodule efficiency record of 38.5%. [9]

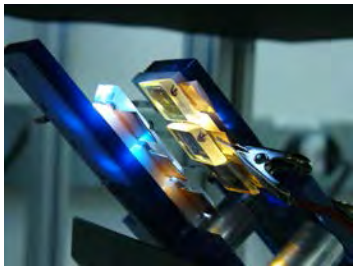

(a) Gen I

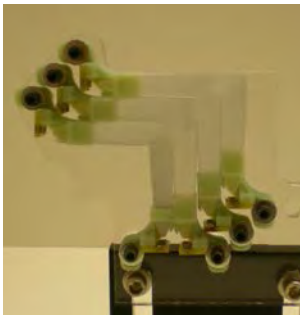

(b) Generation III

(c) Generation III

(d) Gen. IV with PDMS CPC

(e) Gen. IV with short glass lightpipes

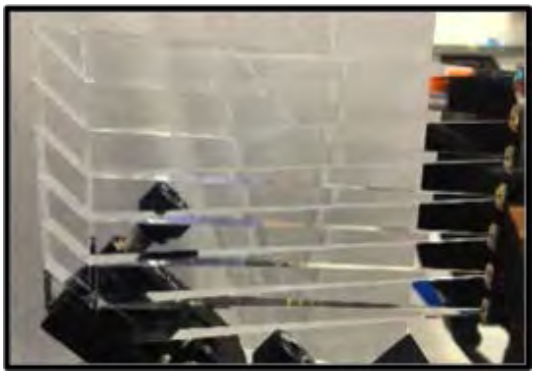

(f) Generation IV with long lightpipes

Figure 3.2: Polyhedral Specular Reflector prototype photographs.

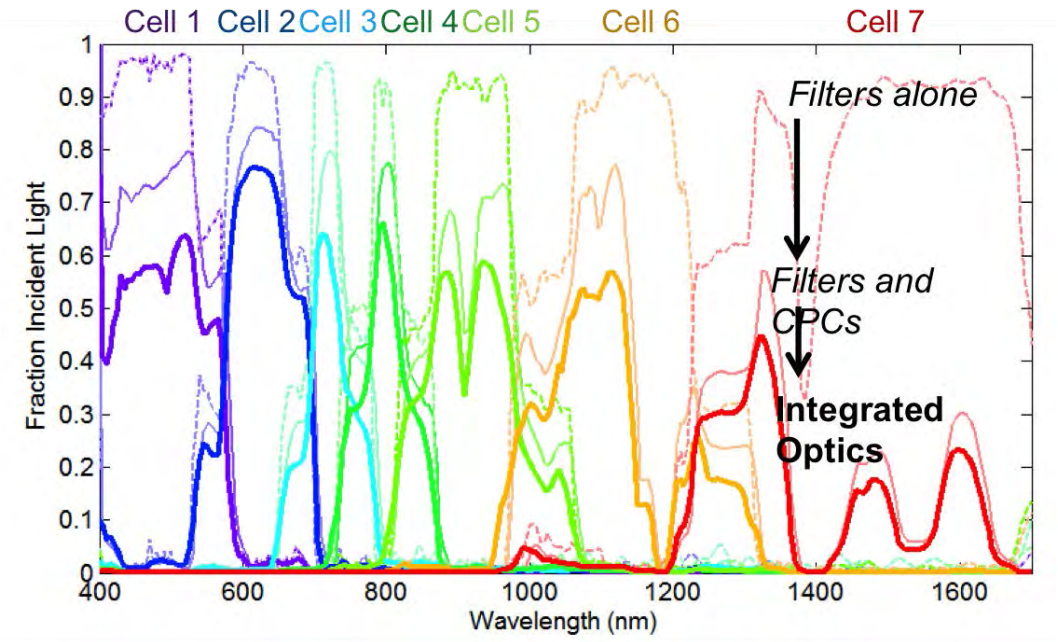

Figure 3.3: Polyhedral Specular Reflector with PDMS CPC optical characterization results. © 2015 IEEE

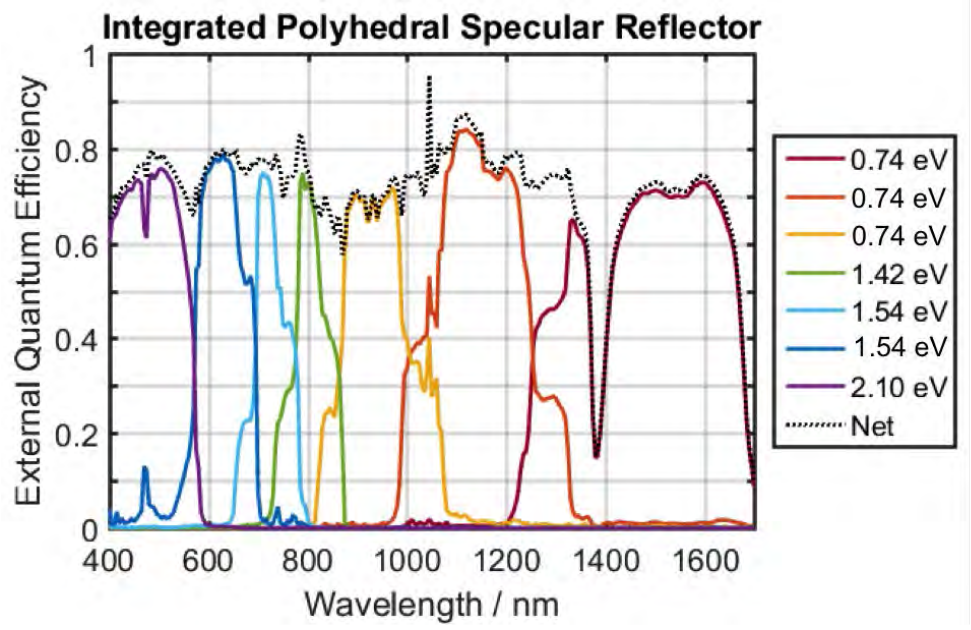

Figure 3.4: Polyhedral Specular Reflector with short lightpipes full device external quantum efficiency.

Chapter 4

COMPOUND PARABOLIC CONCENTRATOR FABRICATION AND CHARACTERIZATION

Given its potential for 50% module efficiency as described in [33], the winner of the Caltech Full Spectrum team's internal design competition and choice for full prototyping was the Polyhedral Specular Reflector (PSR). The simulated power conversion efficiency, though short of 50%, is higher than the state-of-the art as of this writing in 2016. This design uses seven distributed Bragg reflector (DBR) filters embedded at a 45° angle in a solid optical train as shown in Figure 3.2. Normally incident light enters the structure through a hollow, reflective primary compound parabolic concentrator. The primary concentration level is low to minimize the spread of angles hitting the filters for high optical efficiency of splitting. Each filter selectively reflects one band of light perpendicularly out of the incident beam into a receiver composed of a secondary concentrator and a subcell tuned to best convert that band of light. Parameters in the design include the overall size scale and the degree of primary, secondary, and overall concentration. Thus the name PSR refers not to a completely fixed design but a suite of designs that share the structure shown in 3.1e. The overall size scale and the degree of primary, secondary and overall concentration can be co-optimized for either $/W or high efficiency metrics. We opted to prototype a version of the PSR design optimized for highest efficiency. At the same time we explored the design space for a different version that would give the lowest cost. In order to prototype the highest efficiency design, we made and characterized compound parabolic concentrators (CPC) – the focus of this chapter. Explorations of the design's commercial potential are summarized in Chapter 5, including the cost model to design for lowest $/W.

4.1 Compound parabolic concentrator fabrication

Higher concentration improves efficiency (as described in Section 1.4) as long as the efficiency of concentration is high. Constraints on the level of achievable concentration in the PSR design include minimum cell edge length of about 1 mm. This is a rough lower bound for ease of manual handling during processing. Also, as the surface-area-to-volume ratio increases, surface recombination losses play more of a role, so for this reason we do not want smaller cells. In addition, we

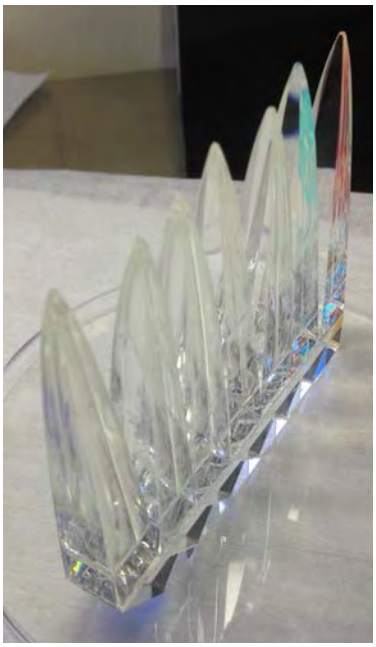

Figure 4.1: Schematic of the Generation IV Polyhedral Specular Reflector and photograph of PSR optical train with PDMS concentrators (images from Carissa Eisler).

restricted ourselves to an overall height of about 30 cm to avoid assembled modules being too heavy and unwieldy. A design with 1.73X primary concentration and 200X secondary concentrators was decided upon with highest possible module efficiency in mind. As intermediate steps toward this goal, we acquired or made a variety of compound parabolic concentrators (CPC). In total, we acquired and fabricated six different compound parabolic concentrator designs with distinct levels of concentration, material and cross-sectional shape to develop a measurement procedure and to understand trade-offs in efficiency.

CPC sources

We purchased a 13x Edmund Optics stock B270 glass circular cross-section CPC which was fire-polished after machining. Circular diamond-turned acrylic CPC were custom ordered from Syntec Optics at 15.6X and 27.7X. Finally, square injection molded CPC made of a proprietary plastic which was selected for visible light LED were also acquired from a vendor. Finally, Polydimethyl siloxane (PDMS) CPC with 77x and 194x concentration were fabricated in our labs. The lower concentration shape profile was milled into an aluminum block at the Caltech machine shop and then polished by hand using mechanical and chemical polishing. This piece was used to make molds in a low mechanical modulus PDMS (Sylgard 184 4:1 base:binder).

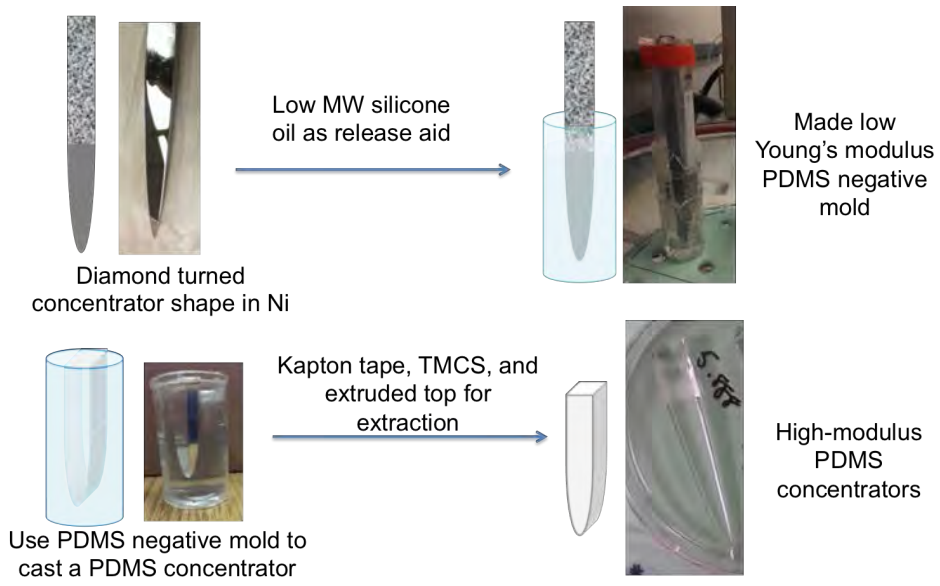

Figure 4.2: Schematic of the PDMS CPC molding process to make 194X concentrators using a high-quality diamond turned CPC form in a two-step molding process.

The mold was used to cast PDMS concentrators using a higher mechanical modulus PDMS mixture (Sylgard 184 2:1 base:binder). This process, shown schematically in Figure 4.2, was ultimately the most successful for producing CPC though yields remained low. For the higher concentration profile, Nipro Optics used single-point diamond turning to machine the square CPC profile into a thin layer of phosphorous alloyed Ni, plated on steel. The metal part was used to cast both electroformed molds by Nipro as well as PDMS molds in our lab to cast PDMS CPC.

The electroformed molds did not successfully produce usable CPC. The interior of the nickel mold surfaces had some imperfections that appeared to be particles stuck on the surface. These imperfections were transferred into molded CPC to the extent that they could be extracted. Attempts to extract crosslinked PDMS from the molds, however, invariably tore or otherwise damaged the concentrators. Having the PDMS stop flush with the top of the mold meant there was nothing to grab and use as leverage to pull the CPC out of the molds. PDMS is a very low surface energy material and the 194x CPC had a very large surface-area-to-volume ratio so a lot of friction needed to be overcome to extract the CPC from the molds. The PDMS was not compressible enough nor the mold large enough to fit grasping tools into the mold to exert pressure and grasp the CPC by two of its sides. In an attempt to overcome this challenge, we made tape collars at the top of the electroformed mold

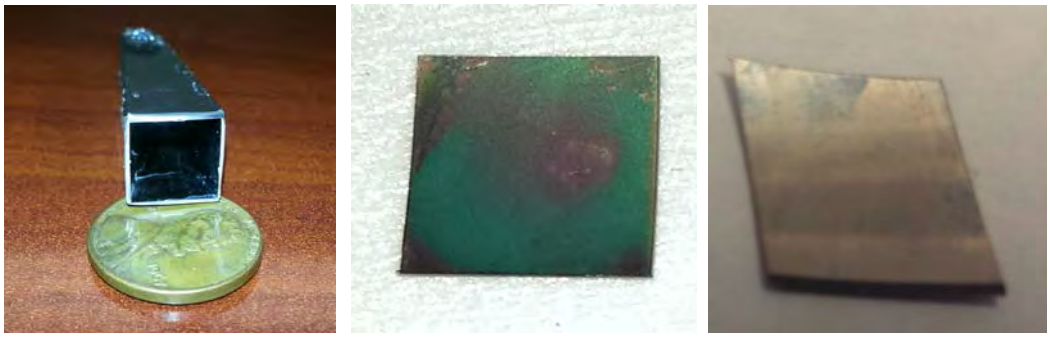

(a) Electroformed mold (b) Oxidized Ni (c) TMCS treated Ni

Figure 4.3: (a) Electroformed nickel mold with coin for scale showing some debris and scattering sources on the inside of the mold, (b) oxygen plasma cleaned nickel mold surface showing damage from oxidation, and (c) foggy nickel surface after exposure to trimethylsilyl chloride.

to create a knob on top that could be used to pull CPC up and out. However tears would often form in the PDMS at the height of the tape-mold interface. This likely occurred because the square CPC corner concentrated the stress applied. These tears would propagate tearing the whole CPC. In such cases, the PDMS in the mold would need to be cut into smaller extractable pieces. Cleaning the remaining PDMS out for reuse posed challenges. In a few cases this procedure worked to partially remove PDMS CPC from the electroformed molds if a tear formed lower in the structure. We could never successfully extract a whole CPC manually, however, so we investigated surface treatments and a non-manual extraction apparatus to facilitate extraction.

Various surface treatments were attempted on mostly flat test samples of a nickel electroform cut to about 1 cm by 1 cm by wire electric discharge machining (wire EDM). Motivated early on by the idea that the CPC were getting stuck on the visible surface imperfections of the molds, attempts to lubricate the PDMS-Ni interface started with improved cleaning of the nickel surface using both solvent rinsing and wiping with solvent moistened lens cloth. This did not change the ease of separation. Plasma cleaning nickel pieces caused oxidation of the surface leaving it roughened and damaged which a greenish tinge of nickel oxide. Trimethylsilyl chloride, a treatment often used on PDMS to modulate surface properties, left a foggy residue on the nickel surface that could be scratched off with wooden applicators or fingernails. PDMS curved against this foggy surface had this non-specularity transferred, resulting in rough rather than mirror-like PDMS molded surfaces. We additionally attempted to use low and high molecular weight silicone oil. The high molecular weight oil coated the mold with a macroscopically thick layer of oil that

ran during PDMS curing, leaving hundreds-of-micron to millimeter sized tracks in the molded CPC even after the oil treated mold was turned upside down and left to drip overnight. The low molecular weight silicone oil seemed to dissolve into PDMS, leaving no traces on the final part but also not improving ease of extraction. A visiting engineer who acted as a design consultant to this project designed a fixture for the bottom of the molds to attempt to blow pressurized air from the bottom of the mold to push the CPC out. However the opening at the bottom was $< 1mm^2$ in area. The first and only implementation of this concept did not exert enough force to remove parts from the mold.

CPC Measurement

For measurement, the PDMS CPC were cut on top using a razor blade to obtain a flat surface at the appropriate height. They were then attached using an optical adhesive to a glass cover slip to use as a handle and to provide a flat top interface. The top of the glass slide was taped off to make an aperture (Figure 4.4b,4.4c) with matte black tape. The circular cross-section Syntec CPC were epoxied into a collar at the top (Figure 4.4d), which reduced their effective aperture area from 9 mm diameter to 7.9 mm diameter without any additional interface between the CPC and light source. Finally square injection molded CPC also acquired from a vendor were held for measurement using a clamp to hold two parallel sides during measurement, so no additional interface was added nor was clear aperture lost.

Measurements were made using a large area, ABET solar simulator with divergence angle 1.3° as the light source. Two Advanced Photonix Si photodiodes were used to measure intensity at the input and output of the CPC, so these efficiency results are for the spectrum below ~1100 nm. Measurements were made using a solar simulator with an angle spread of 1.3° (half-angle of divergence). The reference photodiode was placed in the plane of the input face of the CPC as close to the input as possible (about 1 cm away) and the measurement photodiode was aligned with the bottom of the CPC to obtain the light intensity at the output of the CPC. Figure 4.5 shows photos of the setup from two angles including the measurement photodiode aligned with the output of a CPC and the reference photodiode mounted on the fixed platform used to hold the CPC. An x,y,z-stage setup was used for alignment and Cargille Refractive Index Liquids was used to form good optical contact between the CPC output and the top of the measurement photodiode.

As the measurement photodiode was raised from a position x-y aligned but far below

(a) 194X PDMS CPC

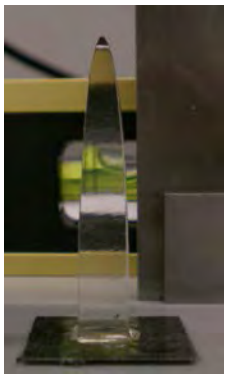

(b) 194X mounted

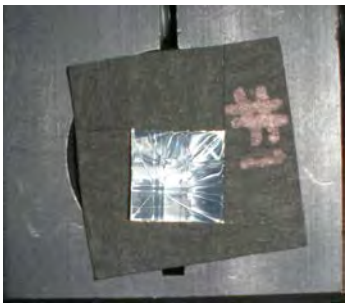

(c) 194X apertured

(d) Mounted circular CPC

Figure 4.4: CPC, fabricated and mounted for measurements, (a) Light being split in a partial optical prototype with the light path clearly visible due to scattering within the PDMS, (b) Series of PDMS cast CPC showing varying height and degrees of surface roughness, (c,d) Two views of a square PDMS CPC mounted to a glass coverslip with optical adhesive and apertured with black masking tape and (e) circular CPC mounted in a collar for efficiency measurements.

the CPC to close to the output face, the current increased slowly. The current jumped up when the index matching liquid on the photodiode came into contact with the tip of the CPC. Once in contact, I adjusted the stages to maximize the photodiode photocurrent. In some cases, this occurred when the photodiode was raised to the point that it pushed the whole CPC upward or when the CPC and photodiode were in sufficient mechanical contact that the motion of the photodiode in the x-y plane deflected the CPC tip. In these cases, it seemed that the deformation or displacement from force applied by contact with the photodiode was compensating for imperfections such as the top of the CPC being cut at a non-perpendicular angle to its axis or shape deformation of the tip. While this allowed slightly higher efficiency at the individual CPC measurement stage, it was a source of concern for a fully assembled device in which it would be preferable to have a CPC that provided the desired concentration well without needed to be strained in a particular

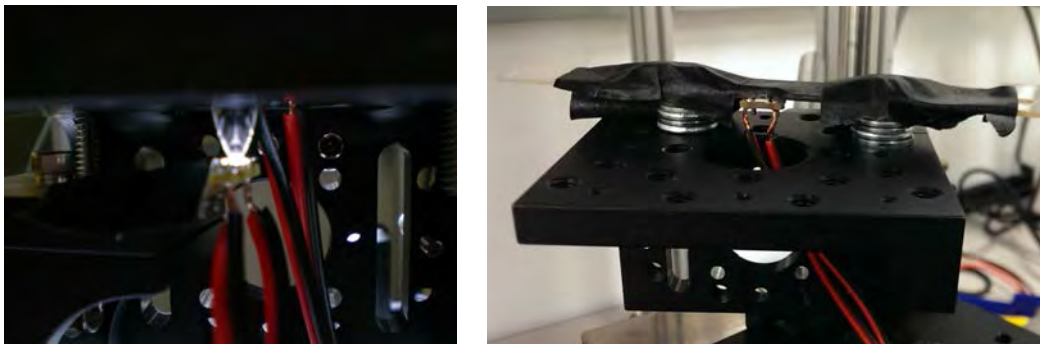

Figure 4.5: Measurement setup for CPC showing (left) the measurement photodiode attached to an x,y,z-stage setup for alignment and (right) the top photodiode mounted to a fixture that also holds the CPC in a fixed location. The top CPC setup was fixed in a location and the measurement photodiode was aligned with its output aperture to maximize the measurement photodiode current.

direction. The surface adhesion that posed challenges for mold extraction also caused problems at the cutting stage when the razor blade surface would stick and then suddenly release as more and more pressure was applied leading to uneven cuts. This made an internal interface that could scatter.

Our visiting engineer, Dirk-Jan Spaanderman, improved upon the manual cutting procedure by designing a jig to hold the CPC at 45° and the razor blade on a cutting track to even the pressure and the angle of the blade to remove some of the manual variability from cutting the CPC top. By initiating the cut at a corner with a smaller area of contact, less pressure was needed and thus less deformation induced in the whole CPC. Despite searching for a more effective cutting tool including the thinnest available gauge wire, individual steel wool threads, and a scalpel, no candidates were identified that could cut through PDMS more easily than a razor blade. While the jig improved cuts, the underlying problem of PDMS deforming as it was stressed and then suddenly slipping and creating a jagged edge along the input face persisted.

The efficiency of the CPC as measured in this setup is defined as

$$\eta = \frac{Output\ light}{Input\ light} = \frac{I_{mmt} * PDCF}{I_{ref} * \frac{A_{in}}{A_{PD}}}, \tag{4.1}$$

where I_{mmt} is the current of the measurement photodiode, I_{ref} the current of the reference photodiode, A_{in} input area of the CPC, and A_{PD} the area of the photodiode. The photodiode correction factor $PDCF$ was obtained by measuring the reference and measurement photodiodes against one another six times before each measurement to get the photodiode correction factor – the ratio of their currents

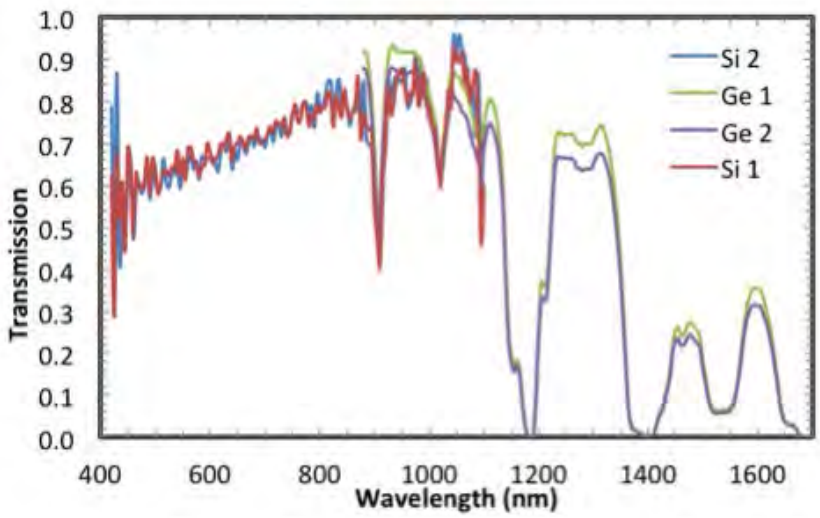

Figure 4.6: CPC transmission measurement using a supercontinuum laser source with monochromator and Si and Ge photodiode detectors showing large deviations from ideal transmission across all wavelengths and especially in the infrared.

from measurements at the same location. It is assumed that the spatial output of the source lamp is uniform so that the current can be scaled up by the ratio of areas of the CPC input face to the active area of the photodiode to obtain the light intensity hitting the CPC input. It is also assumed that no stray light is hitting the measurement photodiode; i.e., only light that is coming through the CPC output face hits the photodiode. Anecdotally, there is a shadow cast around the output of the CPC where light is totally internally reflected to the CPC output.

A second measurement setup was used to measure the best 194X PDMS concentrator. The source was a supercontinuum laser with a monochromater allowing spectrally resolved measurements. Additionally, both Si and Ge photodiodes were used to measure through 1700 nm.

CPC Results

The PDMS CPC made in our labs have some visible surface roughness and volume scattering. This can be seen especially well in Figure 3.2c in which a laser beam's path through the CPC is clearly visible. Table 4.1 summarizes the results of the measurements. First, Equation 4.1 was used to produce a raw efficiency. The best efficiencies of 194X CPC was 69.6%±3.1% and overall 77.6%±1% for 15.6X circular CPC where errors include only precision of the measurements. 4.2 summarizes relevant information on these five CPC shapes.

Samples				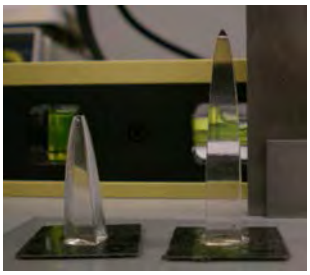	
Fabrication Method	Single-point diamond turning	Single-point diamond turning	Injection molding	cast from CNC machined positive	cast from diamond turned positive
Material	Acrylic	Acrylic	Proprietary plastic	PDMS	PDMS
Concentration	15.6X	27.7X	42.25X	77X	194X
Cross-sectional shape	Circle	Circle	Square	Square	Square
Output angle of CPC (°)	90°	90°	90°	50°	26°
Best Raw Efficiency	92%±2%	77.6%±0.7%	67.7%±0.8%	74.8%±1.3%	69.6%±3.1%
Preliminary corrected Efficiency	n/a	80% ±1%	70% ±1%	n/a	n/a

Table 4.1: CPC measurement Fresnel corrections

Preliminary corrections were made to the raw measured efficiency in order to back out the efficiency of the CPC itself by using ray tracing simulations. We sought to know the efficiency of the CPC itself (η_{CPC}) independent of its environment in order to appropriately use CPC measurements to estimate the efficiency of the whole photovoltaic module. This was done by assuming that the photodiode had only a 160 μm thick encapsulant layer (of refractive index $n = 1.42$ or $n = 1.59$, the lower and higher bounds for a clear plastic layer since the encapsulant material is unknown) on top of bare Si. A ray trace was done by my colleague John Lloyd for the photodiode in which a light source outputting isotropically into a half angle of 1.3° is incident on it. Fresnel reflections at the air-encapsulant interface and and the encapsulant-Si interface are the only loss mechanisms accounted for. The encapsulant is assumed to be lossless and the Si perfectly absorbing. The percent of incident light absorbed is found to be 74.8% with a low refractive index encapsulant or 77.3% if the encapsulant were high refractive index. Table 4.1 summarizes these

	77X PDMS CPC	42.2X Acrylic CPC	Photodiode alone
n = 1.42	75.1%	71.9%	74.8%
n = 1.59	78.2%	78.5%	77.3%
n = 1.42 correction factor	0.996	1.040	xx
n = 1.59 correction factor	1.029	0.985	xx

Table 4.2: CPC measurement Fresnel corrections

numbers for each combination. A second ray trace was done for the 27.7x acrylic circular CPC and the 77x PDMS square CPC. For the former a constant refractive index of 1.49 was used. For the latter a 200 μm glass coverslide was included as an additional interface and PDMS refractive index from [34] data across a wavelength range of 400-850 nm was used. In both cases, the CPC was assumed to be in index-matched optical contact with the encapsulant on the photodiode.

In the ray trace with the CPC, incident light is still 1.3° in angle spread at the input to the CPC, but as it propagates through the CPC by total internal reflection off the sidewalls, the angular spread increases up to the output angle (90° for the circular 27.7X CPC and 50° for the square 77X CPC), increasing Fresnel reflections off the encapsulant-Si interface. The percent absorption in the Si with the CPC in place is found to be 76% = $\eta_{RayTrace,CPC}$. Thus to back out the efficiency of the CPC, we use

$$\eta_{CPC} = \frac{\eta_{RayTrace,Photodiode}}{\eta_{RayTrace,CPC}} * \eta_{Measurement}. \tag{4.2}$$

This ability of the photodiode to absorb light at higher angles is not part of the internal efficiency of the CPC. In our device, the cells have specially designed anti-reflection coatings to ensure that light within our narrow spectral bands will be transmitted with high efficiency into the underlying cells for the angle range to which they are exposed. For both ends of the range of encapsulant refractive index, $\eta_{measurement}$ is close to one and thus not a significant source of loss.

Another loss mechanism is absorption in the concentrator material. Based on the absorbance given in Figure 4.9 and estimated optical path length of light passing through the CPC, 11% of light above the silicon absorption edge is absorbed by the PDMS CPC. To track down more of the remainder, a repeated measurement was made on our 'SARP' set-up. Using the SARP setup the transmission efficiency of the CPC was found to be 70% rather than 62.2% ± 4.3%. The SARP detector is a 1

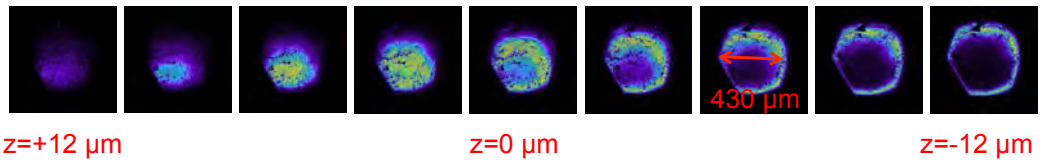

Figure 4.7: Confocal microscope image of the output face of the polished aluminum CPC showing significant rounding at the corners and bottom face itself on the order of tens of microns.

cm x 1 cm area versus 1.5 mm x 1.45 mm so scattering was through to play a role in this increased light collection.

Confocal microscope images of the tip of a CPC molded by the Al positive showed significant rounding of both the square cross-section and the outpout face (Figure 4.7). Ray tracking corner curvature suggests it causes some loss. Modeling the CPC shape with corner fillets of varying radius of curvature (between 1 μm and 300 μm shows a minor drop off for a single wavelength. As the fillet radius of curvature increases the effective acceptance angle (the angle within which CPC transmission efficiency is high) decreases.

CPC Discussion

The efficiencies of fabricated CPC are much lower than those of simulated concentrators. Potential losses could come from surface scattering, volume scattering, shape inaccuracy, absorption, and the attachment interface to the photodetector used in the characterization measurements. In addition to these, the PDMS CPC could have scattering at the top interfaces at the point of attachment to glass slides.

Generally, the circular cross-section CPC have higher performance than square cross-section CPC. First, circular cross-section CPC are more ideal than square cross-section CPC due to the absence of skew rays which can get bounced around the corners and ultimately rejected back out of the top of the structure rather than propagated to the output face. Additionally, the two circular cross-section structures have lower aspect ratios and were produced by single-point diamond turning. This precision fabrication method gives better surface quality and higher shape accuracy. The shape accuracy can diminish as the length and aspect ratio of the part increase, however. As the machine tool applies pressure to make cuts further from the anchoring point of the structure, more deflection will occur giving deviations from the intended curvature profile. Additionally, the 27.7X concentrator has a longer path length of plastic resulting in higher absorption losses. Between the two PDMS CPC,

similar arguments can be made for the 194X concentrator having higher absorption losses. The positive CPC at 194X was made by single-point diamond turning, a much more precision method, giving better surface quality than the CNC machined 77X positive. Its specular surface finish is shown in Figure 4.2. However the additional shape inaccuracy from the higher aspect ratio may or may not outweigh the benefit of moving the higher precision fabrication method. In fact the rougher surface might have allowed more scattered light to be collected by the photodiode in the measurement of the 77X concentrator providing another possible source of its higher efficiency. There are so many unknowns regarding the intended angle spread and material of the injection molded CPC that it is hard to draw many conclusions from its efficiency. It does however provide an existence proof demonstrating square CPC fabrication by molding.

Turning attention to the 194X CPC, the target of our efforts, in the visible and NIR portion of the spectrum measured by the silicon photodiode of the main measurement setup, absorption accounts for at least 10% of incident light lost. Due to the possibility of multiple reflections of skew rays, the total effective path length of light in the material is likely longer than the CPC height of 5.5 cm. Also a SARP measurement of a PDMS CPC with the output face obscured by mylar, so collecting light scattered light near the bottom of the CPC, showed about 5% of light collected. This leaves about 10-15% of losses unaccounted for.

The ray trace suggests that Fresnel reflections at the photodiode interface are not a significant source of variation in measurements of different CPC shapes. However the difference between measuring the rigid circular cross-section and molded CPC and the flexible PDMS CPC seems like it may cause differences. As described above, the flexibility posed problems both for repeatable CPC efficiency measurements and for obtaining the correct final shape due to difficulty cutting the top of the CPC to a flat surface. The aggregated results of this can be seen in Figure 4.1, where the photograph shows misalignment among the CPC relative to one another attached to the main filter train of the PSR. In this process we have realized that concentrators are not sufficiently produced parts to have good measurement standards. We developed characterization protocols with fixed angular spread sources and flat detectors. The full data that would have provided the internal efficiency of the CPC that we sought was transmission into a medium index matched to the CPC as a function of angle of incidence. We could have gotten full bidirectional scattering and/or reflectance distribution function by external characterization but this would only address surface

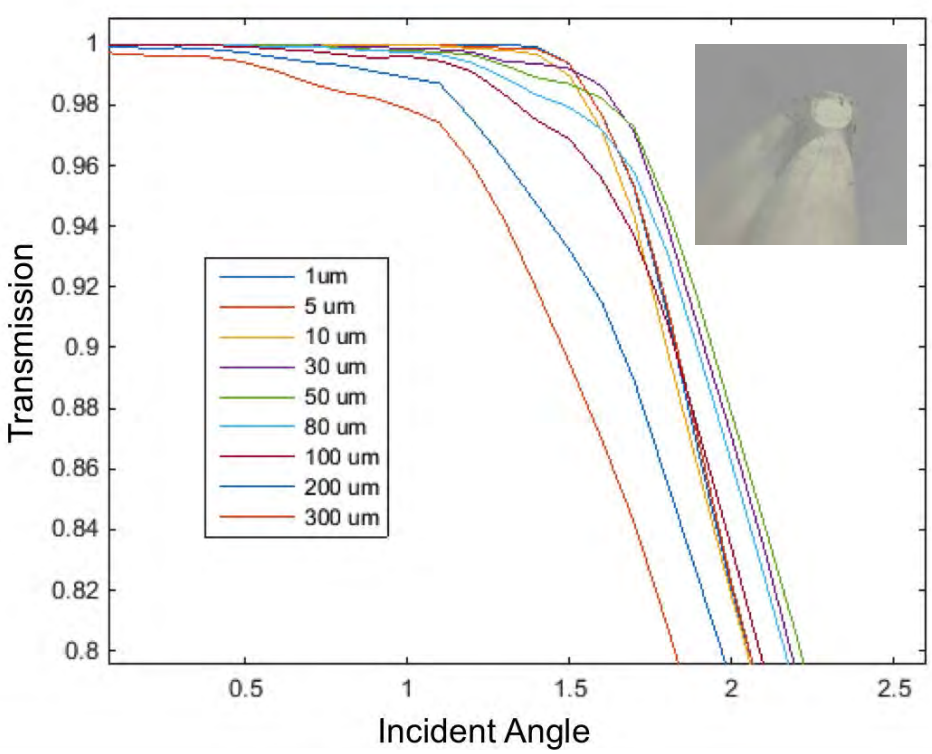

Figure 4.8: Ray trace simulation results for transmission efficiency of a CPC as a function of incidence angle with edge fillets of varying radius.

roughness by allowing us to incorporate the data into ray trace simulations.

We tested a couple of loss mitigation strategies. Toward the end of our time working on PDMS CPC, masters student Annabelle Sibue tried to mold the outer part of a CPC in PDMS around a glass piece. The goal was to have an embedded glass constitute most of the path length to avoid absorption losses. However extracting this heterogeneous structure from the molds without tearing the thin PDMS layers around the glass was more difficult than removing solid PDMS CPC. The thin layers tore very easily. Metal-coating the bottom sides on the CPC where light scatters out was a possibility, but the adhesion of thin metal layers to PDMS is poor and the specularity of a metal layer deposited on a rough surface would be low. We thought about improving the PDMS CPC quality by depositing a smoothing layer on the rough surface, but failed to find materials that could easier serve this role. Finally, a worthwhile experiment would have been measurement of incident light lost due to reflection back out the top of the CPC to determine the shape inaccuracy losses.

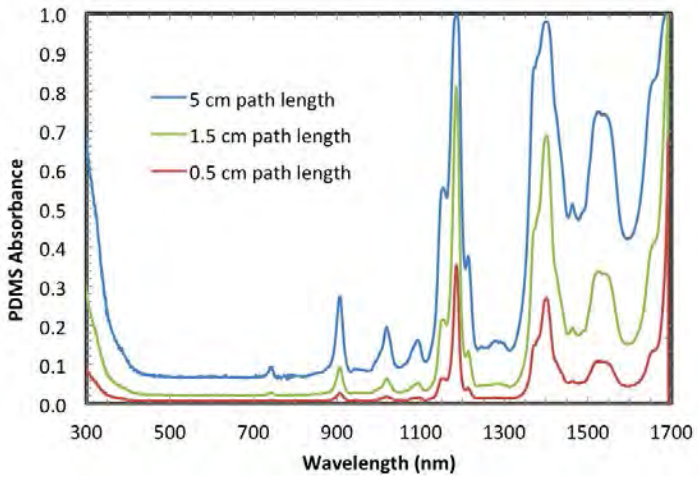

Figure 4.9: Sylgard 184 (2:1 base:curing agent) absorption as a function of path length calculated using measured extinction coefficient data.

Conclusion

We got to the point fabricating PDMS CPC at which we could repeatably mold ~70-75% efficiency 77X CPC and 65-70% efficient 194X CPC. This is far below the 95%-98% efficiency we saw in simulations and were banking on for an ultrahigh efficiency module. For the purpose of demonstrating a high-efficiency spectrum-splitting prototype, the decision was made to move to fused silica lightpipes which can be produced by coarse methods and then polished. We were able to find multiple vendors willing to give quotes for this type of part (unlike CPC), making them less of a struggle to acquire.

However, as discussed in the next chapter, moldable plastic optics are important for reaching high-volume, low-cost production. While PDMS is an optimal material for ease of lab-scale prototyping, the market for bespoke photovoltaic modules is quite small. Thus future work on commercially relevant concentrators should begin by exploring the trade-offs among plano-convex, Fresnel, lightpipe, and CPC concentrator designs with respect to efficiency and ease of fabrication in conjunction with experts in high-volume optics molding. At the academic scale the upfront cost for a mold is too high ($10-100k), especially if cycles of improvements are required for best quality results. On the other hand, even at the laboratory scale, polishing glass to roughness below $\frac{\lambda}{5}$ with an automatic polisher like the one in the Atwater labs is possible.

If there is reason to further explore how to make a high efficiency silicone concentrator, the first steps I would suggest would to be carefully determine our precision

Ni positive's shape profile by a metrology tool. A homemade version might use the deflection of a reflection laser spot to determine the curvature. A commercial example is something like Optical Gaging Products SmartScope ZIP 250. Secondly, I would determine the degree of corner rounding by careful microscopy. (It is a mistake to overlook the utility of optical microscopy or even a good camera's macro lens to assess if a part is as intended.) In the longer term, one would do well to redesign for a shorter path length of absorbing material (<1 cm). In order to ascertain what aspect ratio is feasible for mold removal, I would again use the Ni positive to cast molds of varying heights to attempt to identify if there is an aspect ratio below which removal is consistently possible. Finally, in order to avoid the cutting problem, the only solution I can see is to use sacrificial molds which include a top flat surface and a spout, in the spirit of an injection mold runner. The Ni positive could be used to cast a mold as usual. Then a microscope slide or some other flat surface could be adhered on to the top opening and a hole drilled into the side and a tube inserted that would be used to pour PDMS into the mold and ensure it did not empty out during degassing. The mold could then be cut off including the running portion. This would remove the cut from the critical top surface and place it on a side toward the top, which has much less of an implication for the overall optical efficiency.

Chapter 5

EXPLORING COMMERCIAL PROSPECTS OF SPLITTING PHOTOVOLTAICS

Part of our funding for the Full Spectrum Photovoltaics Project came from the Department of Energy's Adavanced Research Projects Agency for Energy (ARPA-E). They fund high risk, high reward, commercially relevant energy technologies. The agency requires awardees to undertake a technoeconomic analysis and a side-by-side comparison of the projected high-volume cost of our technology versus relevant alternatives in terms of $/W and LCOE. Utility-scale power is a commodity product, so cost is the key factor for adoption. Because new technologies come with additional risk, their cost should not only be lower than the current incumbent technologies but be low enough that there is a driving force to take a risk on them. Keeping this in mind, we used our cost model to inform design choices and undertook market analysis to find niche applications that could serve as entry markets.

Two key cost metrics in solar are $\$/W_p$ and levelized cost of electricity (LCOE). The former is the upfront cost to purchase the system and the latter is the cost of electricity produced by the system over its lifetime. In our cost model, we primarily consider the $\$/W_p$ cost of the module. $\$/W_p$ is the metric of choice among investors and financiers. However our technology's efficiency advantage makes it more expensive upfront in $\$/W_p$ with potential to have lower LCOE, defined as

$$LCOE = \frac{lifetime\ cost}{lifetime\ energy\ production}. \tag{5.1}$$

LCOE includes many factors beyond the $\$/W_p$ cost of the module. First, it includes all the other $\$/W_p$ system costs such as land, permitting, electrical system cost, mounting and racking, tracker, and installation costs. These additional factors are collectively referred to as the Balance of System (BOS). Additionally, assumptions about operations and maintenance cost of the system, details of project financing, performance degradation, and capacity factor are required to project lifetime energy cost. Projections of LCOE are used in setting power-purchase agreements made with buyers of solar energy. During the last couple of years, power-purchase agreements have been signed for solar installations with prices of <$0.06/kWh which has been seen as a target for grid parity for some time (along with $\$1/W_p$ module cost). Factors

enabling this include the price of silicon modules plummeting, solar installations getting low enough in risk that they are able to obtain lower interest rates for financing, and federal and state-level subsidies that have been in place. In order to commercialize our technology, we need to be able to show that either our $\$/W_p$ or LCOE are competitive with current market incumbents.

In section 5.1, the cost model is described. Sections 5.2 and 5.3 explore modified designs with the potential for lower costs. In response to finding the main cost driver to be dichroic filters, we considered two alternatives to decreasing cost. The first is to redesign the structure to a point of eliminating the filters as a cost-prohibitive element. This can be done by increasing the degree of primary concentration as in the 50X Gen IV design, thereby decreasing the number of components per module. Due to the angle sensitivity of dielectric mirrors, however, as the angular output of the primary concentrator increases, the optical efficiency of the structure decreases. Re-optimizing the PSR design for $/W rather than highest efficiency with this reality in mind also resulted in the Mini Gen I and Kirigami PV designs. The parameters, performance, and costs associated with these three design variants are discussed in Section 5.2. The second strategy we explored was to keep the design the same and swap out the spectral splitting elements to alternate filters with the possibility of lower costs. Section 5.3 describes the design of polymer filters as an alternative which avoid the need for vacuum deposition of inorganic dielectric layers. Chapter 6 considers high-contrast gratings as an alternative optical element, motivated by their subwavelength thickness and lower angle sensitivity. In Section 5.4, I discuss the effectiveness of our cost model including the input of a third-party consultant. Finally, in Section 5.5, I discuss the take-aways from our market analysis.

5.1 Full Spectrum Cost Model

Early in the Caltech Full Spectrum Photovoltaics project, Kelsey Whitesell-Horowitz developed a cost model of our spectrum-splitting technology. The model projected costs for each component, as listed below. The output of this model was a $\$/W_p$ module cost for a particular point design of the PSR which could be combined with financing, location, and system performance assumptions to project LCOE (in $/kWh) for the technology.

Cells

Cells costs were drawn from NREL cost projections [35] for large scale (500 MW) III-V semiconductor alloy cell production as well as through private correspondence

with Alta Devices, a GaAs solar cell company co-founded by Harry Atwater. It should be noted that we used a cell cost rather than a cell price, implicitly assuming that we would produce these cells.

Assembly

In many cases somewhat customized equipment would be necessary, for example custom robots for automated assembly of components, so the most realistic costs could not be realized without contracting with a vendor to do design work. In these cases, the closest commercially available option is considered instead.

Bottom-up Model of filter production cost

In estimating filter costs, it was determined that we would need to produce dichroic filters at a scale that made a large dent in the total market, and thus, the model assumed in-house filter fabrication rather than sourcing them from a vendor. The total cost of filter production comprises material, operating, and capital costs. To establish a bottom-up production model of the PSR filters, first, a procedure was established for filter production. The three main steps were determined to be substrate cleaning and drying, thin-film layer deposition, and protective sealing. For each step, any needed capital equipment for the step was identified. Substrate cleaning and magnetron sputtering tools were identified as the main capital needs for filter production. Depreciation was assumed to be ten-year, straight-line depreciation with no salvage value at end-of-life to determine the annual capital costs. The number of tools needed for a given step was determined from the target annual production volume and the tool's cycle time. These values were determined from specifications for commercially available tools, phone calls with representatives at companies making relevant tools, and the NREL cell cost report [35]. Additional values drawn from the NREL work included the number of workers needed per tool and the ratio of indirect workers needed per direct worker. The number of tools needed also implies a certain facility size and thus costs for rent, maintenance and electricity input required. Finally, material utilization rate for each step as well as yields for each process could be used to determine total materials needs. Quotes were acquired for materials for volumes needed at the target production scale. If a high volume quote could not be acquired, estimates were used either from commercially available volumes or listings on the online vendor Alibaba. With the bottom-up model, benefits of scale can be captured and costs projected as a function of production volume.

Injection molded optics

The costs of optical elements were based on a simple model for high-volume injection molding which was not bottom-up. Economies of scale associated with lower machine rate or material cost are not considered. All non-recurring expenses associated with initial engineering of an appropriate mold are lumped into the mold cost. The total $\$/W$ cost of a given molded component is

$$\begin{aligned}\frac{\$}{submodule} &= Tooling\ Costs + Processing\ Costs + Material\ Costs \\ &= \left[\frac{Mold\ Cost}{Uses \times Batch\ size} + \left(\frac{\$}{hr}\right) \times t_c + V\rho \times \left(\frac{\$}{kg}\right)\right] \times \frac{parts}{submodule} \\ \left(\frac{\$}{W_p}\right)_{molded\ component} &= \frac{\frac{\$}{submodule}}{\frac{W}{submodule}} \end{aligned} \quad (5.2)$$

where t_c is the cycle time, ρ is the density of the molded material, V is the volume of the material needed in the part. The batch size was estimated by taking a typical mold area of 30 cm^2 x 30 cm^2 and dividing it by the cross-sectional area of the part to be molded. Thus, for the primary concentrator this was taken to be

$$Batch\ size = \frac{30\ cm^2 x 30\ cm^2}{CPC\ input\ edge\ size x CPC\ height}. \quad (5.3)$$

It was assumed that the four sides of the square hollow primary concentrator would be separately molded and silver-coated and epoxied together.

Electrical

For electrical costs, we projected an amount of metal for subcell string connections as well as the cost of power conditioning electronics. We used a quoted price for 3000 bypass diodes of $1.28/diode.

5.2 Applying the cost model to design decisions: Redesigning the PSR

We applied the cost model to our baseline point design, the 9X Gen IV, which was optimized with 50% module efficiency in mind as the target (actually 52% in recognition of there likely being unanticipated hurdles in the experimental realization). The module cost of $\$2.05/W_p$ was unsurprisingly too high for a realistic photovoltaic system, so we went through a series of redesigns to address cost drivers. Figure 5.1 shows the array of our design concepts which will be discussed below. The schematics and photograph are to scale. The 9X Gen IV is shown without its primary concentrator or cells. The results of cost modeling for each of the designs

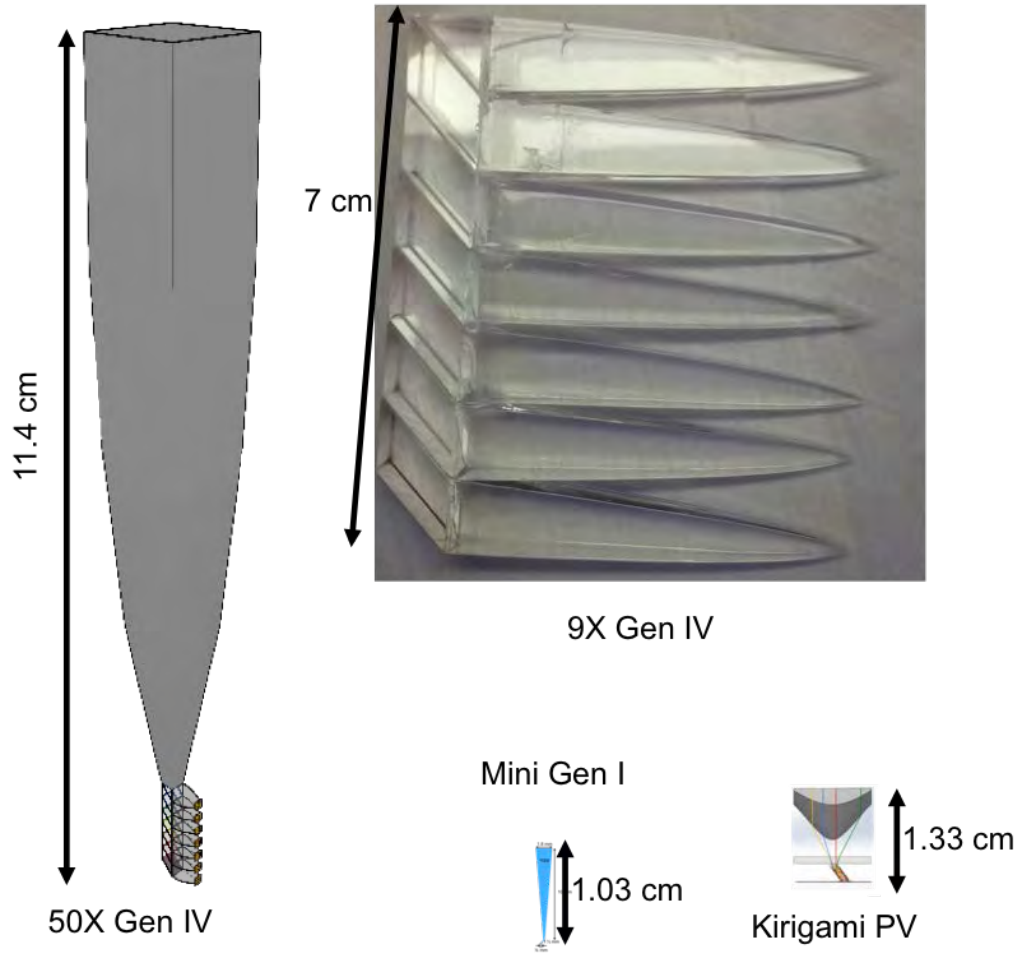

Figure 5.1: Summary of PSR designs to scale.

are shown in Table 5.2, where the Kirigami PV cost projection come from our third-party consultant. The total submodule costs come to well above the target of $\$1/W_p$. The single largest cost comes from the dichroic filters which comprise almost half the submodule cost.

50X Gen IV

In response to the high cost projection, we opted to move to a much higher degree of primary concentration (and a correspondingly lower secondary concentration). The motivation was to decrease the area of filters per unit aperture area. To prevent the primary concentrator from getting too tall as the degree of concentration increased, we scaled down the whole structure including the optical train and cells. Figure 5.1 shows the 50X Gen IV. Its overall size is much smaller than the 9X Gen IV which has a 30 cm tall primary concentrator. These parameters are compared for all four

designs in Table 5.1. The 50X Gen IV is 11.4 cm in height of which 1 cm is the filter train as opposed to 7 cm for the 9X Gen IV. The costs associated with this design listed in Table 5.2 use largely the same cost model assumptions described above with minor improvements including better large volume costs for solvent used in filter production, batch sizes for molded elements limited to 70, and the depreciation timeline for equipment changed from ten years to a more realistic seven years. Secondary CPC costs increase because with limited batch sizes more molding cycles are required to produce the larger number of CPC needed per Watt, despite their significantly smaller volume per part. Filter costs go down because less area is needed. Directly extrapolating costs despite a 7-fold change in the size of the optical train concerned us. It seemed possible we might need a more sophisticated assembly robot, for example, to handle assembling seven unique, filter-coated, ~1 mm^3 angled parallelepiped pieces and seven slightly smaller secondary concentrators accurately, automatically, and quickly in the correct order than when each component was 1 cm^3. However, this was a difficult trade-off to quantify. Capital costs aside, given the increase in parts per unit aperture area, the assembly costs go up unless something in the process changes. We conceived of avoiding assembly by molding the optical train and concentrators around filters already sitting in the correct positions relative to one another. Experimental execution of this remains unexplored.

Mini Gen I

At this small scale corner curvature, the finite radius of curvature of corners and other edge effects start to significantly and detrimentally affect efficiency. These accumulated fabrication concerns pushed us, first, to consider removing the secondary concentrators. Instead the cells would be directly attached to the side of the parallelepiped pieces. We then reconsidered use of the filters altogether. The cells themselves have sharp absorption cutoffs. As long as parasitic absorption of longer wavelength light is low, it can pass through the cell, reflect off the metallic back-reflector, and keep traveling down the optical train. Thus, re-opening the design space, we ended up pursuing a design that resembled our original polyhedral specular reflector concept, shown in Figure 3.1a with a trough primary concentrator and eight cells along the body. The optical path can include any number of subcells. From a theoretical point of view the efficiency does not start going down (when including photon recycling and cell luminescence effects) until the spectral bands get smaller than the cell emission bands [36].

In order to re-optimize the number of cells for this design without filters or secon-

	9X	50X	Mini Gen I	Kirigami PV
Number of Cells	7	7	4	4
Concentrator height (mm)	300	100	10	13.3
Primary concentrator material	silvered plastic	silvered plastic	PDMS	PMMA
Secondary concentrator material	PDMS	PDMS	n/a	PMMA homogenizer
Primary Concentration	9	50	116	225
Total Concentration	821	150	116	225
Module Efficiency	50%	42%	37%	40%
PSR height (mm)	70	10	0.33	1.3

Table 5.1: Parameters of four point designs

daries, the optoelectronic model described in Chapter 3 was used to evaluate many point designs across different numbers of subcells, degrees of concentration, and concentrator type. We explored a range of 2-5 subcells, with trough CPC, square CPC, or primary Fresnel lenses as primary concentrators providing 1X, 25X, 100X, 225X, 400X, 625X, and 900X concentration. The designs were evaluated for cost. We ran the cost model on the highest efficiency designs and whittled those down to a best option with lowest $/W. The design at this point had diverged enough from the design the cost model was made for that it seemed necessary to revisit the details. The same tools and processes assumed when the structure was one to two orders of magnitude larger and included additional components might no longer apply. For power conditioning electronics costs we referred to a Greentech Media Research report [37] which had projections for 2016 (made in 2012) of $0.31/W for microinverters and $0.37/W for a central inverter with DC optimizers. We used the same areal costs (in $/$m^2$) for cells as above. The previously used price of $1.28/bypass diode ended up being an significant overestimate for a large volume order of $0.1-0.15/diode. We assumed one microinverter per 280 W and one bypass diode for every four microinverters. Wiring was simplified to metallic traces on a PCB or other support rather than insulated wiring as the overall sizes shrank to millimeter

Item	9X	50X	Mini Gen I	Kirigami PV
Assembly	0.249	0.25	$0.02	
Secondary CPCs	0.27	0.418	n/a	n/a
Primary CPC	0.38	0.194	$0.12	0.153-0.267
Parallelepiped and prisms	0.173	0.004	$0.00	0.125
Filters	0.904	0.101	n/a	
Anti-reflection Coating	0.055	0.059	$0.79	
Total optics costs	2.03			
Total cell costs	0.020	0.135	$0.20	0.10-2.14
Total Submodule costs	2.05	1.5	$1.58	
Electrical	0.617	0.338	$0.46	0.22-0.25
Total w/o assembly ($/W)			$0.80	0.40-2.56
LCOE estimate	0.21		$0.09	–
LCOE estimate w/o assembly	–		$0.05	0.047-0.115

Table 5.2: Costs of four point designs

ranges. Assumptions about assembly time, batch size, and what constituted one molded unit varied, unfortunately, without much practical input about reasonable manufacturing limits. Through a private communication we got an estimate of $\$40/m^2$ as the cost of primary Fresnel concentrator. For 1D trough CPC, extrusion was assumed as the manufacturing process rather than molding.

In the initial cost model, the batch size for injection molding was determined by dividing a standard mold size (30 cm by 30 cm) by the cross-sectional area of each part. This greatly overestimated batch sizes. Over time we learned about many constraints in the process. First, plastic must be injected into the mold fast enough that it does not solidify on the way. Thus if the path of the plastic is too long we can end up with defects such as internal scattering interfaces. Additionally, for parts like CPC with six faces needing to be high quality optical surfaces, some minimum post-molding work would need to be done to remove the little burrs that come from breaking the runners feeding plastic into the mold cavity. Also for highest efficiency, one would use a four-part rather than a two-part mold to make square CPC, so that each face of the mold could be single-point diamond turned. With a

two-part mold, the fine details too small for the tool head to reach would need to be coarsely machined and then polished resulting in lower shape accuracy and overall quality. However having batch sizes larger than one for a four part mold adds cost and complexity. In general for molding, we learned the rules of thumb that batch sizes should not be higher than 64 and that for quality optical parts, closer to 4 was preferable. Finally, the machine rate for injection molding was assumed to be fixed at a high-volume rate regardless of production volume. Additionally, given that we require optical quality surfaces, our molds would require polishing every few thousand uses.

Evaluating the new range of designs with the updated cost model, we found that at least 100X was necessary for moderate cost cells and that four cells and 225X gave us an optimum in terms of $/W. To get high optical efficiency for this level of concentration, an all solid optical path was attractive to avoid Fresnel reflections. Due to material absorption, the path length needed to stay small, motivating us to shrink down our whole submodule even furthur. These changes produced the Mini Gen I design. We did not find an accessible manufacturing pathway to produce the large primary CPC in a single unit with the submillimeter parallelepiped piece.

Kirigami PV

Continued concerns about joint assembly and part count led us to keep brainstorming leading us to the Kirigami PV design. We traded in the primary CPC for a conventional lenslet array and conceived of a massively parallelized assembly process to handle the thousands of parts per cm^2. The concept, illustrated in Figure 5.2, is to position and attach cells and contacts onto foldable tabs on a pre-cut flexible backsheet. The parallelepiped pieces would be produced as a monolithic sheet with parallelepiped projections at the appropriate periodicity. This sheet would be aligned on top of the backsheet, so that each parallelepiped was placed at the center of the array of cells that end up attached to its sides. A thin layer of optical adhesive is then applied to the cell faces which need to make optical contact with the parallelepiped. The tabs of the pre-cut flexible backsheet with the cells and contacts already attached would then be folded up into contact with the parallelepipeds. Ideally the backsheet would have appropriate thermal properties to provide any heat-sinking the cells would need. Finally, a lenslet array would be aligned so that each lenslet's focal spot for normally incident light coincided with one of the parallelepipeds. Thus, assembling an entire submodule would primarily consist of four steps: laying up the backsheet, aligning the parallelepiped sheet, folding the back sheet onto the

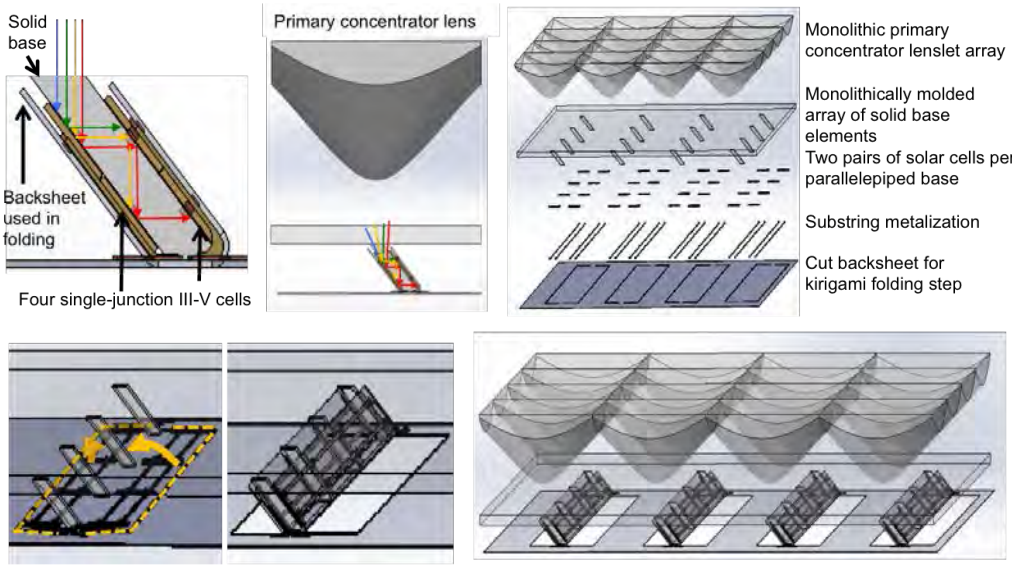

Figure 5.2: Kirigami design.

parallelepipeds, and aligning the primary lenslet array.

If successful, such an assembly process would allow us to benefit from scaling down in size without adding too much additional expense from having to assemble more parts per W. The primary lenslet array can be produced by standard commercial techniques while the parallelepiped sheet would require exploration of more exotic techniques such as liquid injection molding. Optical simulations of this design with a primary plano-convex lens and four subcells had 40% simulated module efficiency, a small improvement over today's cutting edge multijunction photovoltaic modules which have achieved a record efficiency of 36.7% as of this writing. Experimentally realizing a structure with 40% simulated efficiency, would likely result in a lower efficiency. However, if this assembly procedure can be validated, further steps can be taken to re-optimize the efficiency around this design.

External validation of our models

The cost projection for the Kirigami PV design as well as a holistic evaluation of our cost mode was performed toward the end of the project. For external validation and third-party expert perspective on our modeling, we engaged Adam Plesniak as a consultant. Plesniak has spent the past few years working at Amonix (now Arzon) Solar, a concentrating photovoltaics company which deployed >60 MW of concentrating photovoltaic modules during its active period. His take on cost modeling was top down rather than bottom up. We gave him a bill of materials for a complete Kirigami PV submodule, and he added in common components to

go from a submodule to an installed array of 2 MW, as in our own model. These included framing, electrical connectors and wiring to go 6″ by 6″ submodules into 10 submodule by 10 submodule modules. Next, twelve modules were combined with aluminum framing elements to populate an array that is mounted to a ground-mounted pedestal tracker. A selection was made among commercial options for the type of ground mounting as well as for a particular inverter model. Adding these part costs and associated efficiency losses an installed $\$/W$ was determined. For cell costs he assumed a range of cases. The conservative cell cost case was a price of Alta Devices GaAs solar cells as of his analysis of $\$100/W$. The aggressive option was based on our original cost model and the intermediate option was the long range assumptions in the NREL report [35] of ~$\$4/m^2$. For each component he included costs of acquisition from vendors and, rather than breaking down assembly costs, he assumed that in sum they would be about 15% of the total module cost.

His main conclusion was that the uncertainty in cell cost and assembly process were the main concerns. These uncertainties swamped factors such as degrees of primary and secondary concentration as a risk of pushing the cost beyond a practical scale. His cost projections included a potentially attractive range for LCOE ($\frac{\$}{kWh}$) at the low end of <$0.05/kWh, but also impractically high costs on the other. At the same time the resdesigning exercise brought us to a next generation design which is cheaper than our original design and has the potential to be competitive in the solar market. Throughout the process, cost and material absorption pushed us to smaller size elements, and assembly complexity drove massive parallelization in the design.

5.3 Applying the cost model to design decisions: Polymer Filters

As seen in Section 5.1, for low primary concentration, optics dominate the module cost, and the filters dominate the optics cost. Significant decreases in the costs of the filters is an alternative to improve the cost outlook for the PSR. The main cost of the current dielectric, chirped, Bragg stack filters is from the base materials with the capital equipment being the next largest portion. Moving to polymer filters would allow a decrease in both of these cost drivers. One polymer filter (stop-band 590 nm to 700 nm) is optimized as a test case. If simulated filter performance could be realized, module cost reductions between a couple of percent to nearly 30% would be possible.

The polymer filter production cycle is faster than the precision slow vacuum deposition process for the dielectric filters stacks, allowing the capital costs to be

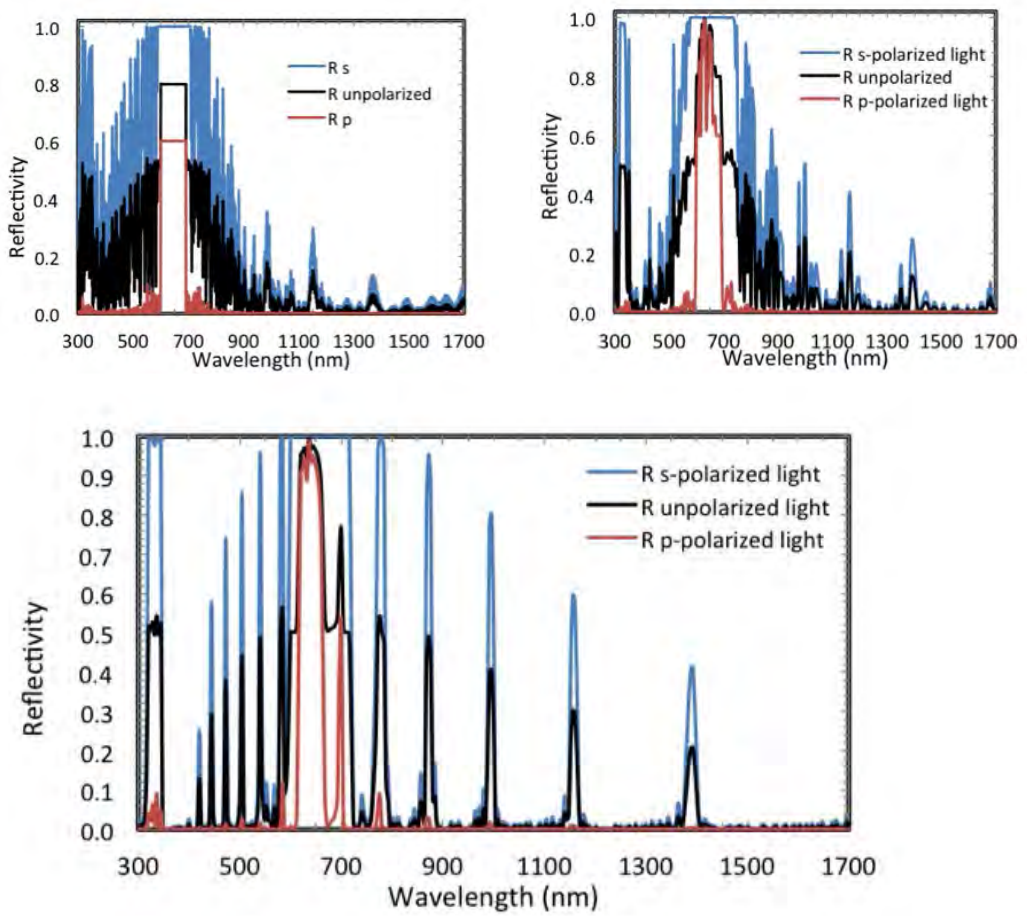

Figure 5.3: Polymer filter reflectivity for both polarizations and unpolarized light for a stack with 1721 layers (top left) and for 3441 layers (top right). The bottom plot shows the reflectivity of the initial filter stack before optimization.

amortized over a larger production volume assuming comparable capital equipment costs. Also, materials costs are much lower. However, because of the method of making the polymer filters in which a machine is used to fold and stretch the layers, we cannot have arbitrary control of the thickness of each layer. The layer thicknesses across the whole stack must be related to the layer thicknesses of the initial block of extruded material. An additional concern with polymer filters is that the incident 45° angle of light on the filters is near Brewster's angle for single polarization reflection, resulting in significant polarization sensitivity in reflection of these filters. While a reflection band for s-polarization light is easy to achieve, many additional layers are needed to get a comparable p-polarization reflection band. The additional thickness increases the path length through the polymer increasing unintended reflection and decreasing out-of-band transmission.

	F1	F2	F3	3M IR reflector[1]
Number of layers	3441	1721	799	
Optimization Target	R>0.8 (600-690)	R>0.8 (600-690)	R>0.8 (600-690)	R (850-1150)
Optimized R (590-700 nm)	81%	74.8%	61.2%	
Mean out-of-band R	10.9%	10.3%	1.7%	18.5%
Total thickness	487.5 μm	244 μm	113.2 μm	
Optical efficiency	76%	75%	–	66.6%

Table 5.3: Polymer filter designs and corresponding optical efficiency values

Materials choices for the polymer filters are constrained by the need for compatible rheological properties in the high and low refractive-index components for co-extrusion. Additionally, since cheaper base materials are a motivation to consider these filters, exotic materials which drive the costs back up are less attractive. Thus for maximum cost benefit, commodity plastics are the best choice: polystyrene (PS) as the high-refractive index layer and polymethylmethacrylate (PMMA) as the low-index choice. The refractive indices used for these materials are plotted in Appendix A. They were assumed to be lossless.

Filter optimization was done using an open-source filter design software program OpenFilters [31]. An initial filter design is input and the program optimizes layer thicknesses to achieve a defined performance target. The optimization was done for the second filter in the PSR stack, which was selected because of its low $\frac{\Delta\lambda}{\lambda}$, making it the easiest to design, thus this analysis represents a best case for performance. This filter should reflect 590 nm to 700 nm and transmit longer wavelength light. Optimized filter performance is shown in Figure 5.3. The reflection spectrum of an initial chirped layer stack is shown at the bottom for comparison. After optimization, this stack of 3441 layers has the reflection spectrum shown on the top right of the figure with >80% unpolarized reflectivity over 600-690 nm.

The optimized filter performances are summarized in Table 5.3 (alongside the published specs of a commercial 3M polymer filter). The total thicknesses are on the order of hundreds of microns. Filter design F1 has a larger number of high-index/low-index interfaces allowing greater reflection within the reflection band but also decreasing out-of-band transmission. Conversely, Filter design F2 has a lower average in-band reflectivity with half as many layers, but has better out-of-band transmission. Design F3 does not have enough layers to achieve the 80%

reflectivity target. To estimate an optical efficiency for the whole filter set based on the single optimized filter performance, it is assumed that each filter has the same average in-band reflectivity and average out-of-band transmissivity as the optimized filters. This allows a calculation of the solar flux allocation to find an overall optical efficiency using

$$Optical\ efficiency = \frac{System\ power\ with\ simulation\ optics}{System\ power\ with\ ideal\ optics}. \tag{5.4}$$

Given our current long-pass filter arrangement, it is more important for transmission to be near ideal than reflection. An erroneously transmitted photon has a high likelihood of getting collected in a lower bandgap cell and producing some voltage whereas an erroneously reflected photon will hit a cell with a bandgap too high to collect it. Thus, despite having much higher in-band reflectivity, the overall optical efficiency extrapolated from F1 is not much higher than that of F2.

With generous assumptions about filter performance: designing the filter with the narrowest reflection band of seven, no absorption in the polymer materials, assuming the ability to set individual layer thicknesses, and neglecting non-normally incident light, we find their effect on $\$/W_p$ of the system to be beneficial. I will consider the 9X primary concentrator system discussed in Section 5.1. With 76% optical efficiency rather than the 92% achievable with the dielectric filters, the cost per Watt of all non-filter system components goes up by a factor of 0.92/0.76 = 1.21. With dielectric filters, the 9X system was found to have a system cost of \$4.26/W with about \$2.05/W coming from the module and the rest from non-module costs. Of the module costs, the filters comprised about 44% or \$0.90/W. Thus the remaining non-filter system cost of \$3.36/W increases to \$4.07/W when the optical efficiency drops. The non-filter module cost increases from \$1.15/W to \$1.39/W due to the performance drop. The module cost estimates are based more specifically on our design, so the cost effect based on module costs is likely to be more accurate in this case.

Next we can estimate the costs of the base materials for the polymer filters. The filter thicknesses are on the order of 0.05 cm (500 μm) and the area of each filter is 1.4 cm^2. With 7 filters per submodule, the polymer volume in the filter stack is 0.245 cm^3. This gives

$$\frac{\$\ polymer}{submodule} = \frac{\$}{kg} \times \frac{1.10\ g}{cm^3} \times \frac{0.245\ cm^3}{submodule} = \frac{\$0.0007}{submodule} \tag{5.5}$$

$$\frac{W_p}{submod.} = \frac{0.1W}{cm^2} \times A_{in} \times \eta_{adj} = 0.04 - 0.37\frac{W}{submod.} \tag{5.6}$$

	Q4 TEA Cost breakdown	With 76% optical efficiency and free polymer filters	% decrease in cost
Module cost ($/W)	$2.05	$1.39	32%
Filter cost ($/W)	$0.90	$0	n/a
Total cost ($/W)	$4.26	$4.07	4%

Table 5.4: Summary of costs for polymer filters

$$\frac{\$}{W_p} = \frac{\frac{\$}{submodule}}{\frac{W_p}{submod.}} = \frac{\$0.0007}{0.04W - 0.37W_p} = \frac{\$0.002 - \$0.018}{W}, \tag{5.7}$$

where concentration C is 1X to 10X, input area A_{in} is degree of primary concentration C times the input aperture of the PSR optical train of 1 cm^2 and adjusted efficiency η_{adj} is $\frac{0.76}{0.92} \times \eta$, cost of polymer is $\frac{\$2.5}{kg}$[2], and density ρ of the polymers is about 1.10 g/cm^3.

As an upper bound for capital cost, we can use the capital cost estimate for the dielectric filters: $0.025/W. As a lower bound, we can assume that, like for injection molding, the marginal cost is simply the raw material cost. This gives a $/W range for polymer filters of $0.002/W to $0.043/W. Thus in a best case, the filters add negligible cost to the system giving an overall decrease of 4%. Since many costs are more uncertain for overall $/W, we can look at potential cost savings to just the module costs which were $2.05/W in the analysis of Section 5.1 and between $1.41/W and $1.46/W with these polymer filter projections. In their materials, 3M uses a cost projection of <$20/$m^2$ [38]. Based on this cost, the $/W of polymer filters would be $0.05/W to $0.49/W for concentrations ranging from 10X to 1X respectively. This is in line with our cost projections described here.

This report indicates that polymer filters are a viable option for cost reduction if the performance assumptions made here can be realized. Next steps would be to incorporate realistic manufacturing constraints to determine the cost-performance parameter space for polymer filters. For practical applications an UV damage mitigation strategy is necessary and may increase costs.

[2] $2.5/kg for EVA from Caelux and DuPont from Q4 TEA

Polymer density	$1.1\frac{g}{cm^3}$
Polymer raw material cost	$\frac{\$2.5}{kg}$
Concentration range	1X to 10X
Filter area per submodule	$9.8cm^2$
Filter volume per submodule (500μm filter thickness)	$0.245cm^3$
3M polymer filter areal cost	$< \$20/m2 =< \frac{\$0.002}{cm^2}$

Table 5.5: Inputs to cost estimate

5.4 Challenges in cost modeling

Challenging aspects of accurately projecting these costs included incorporating the cost of complexity for areas outside of our domain of expertise. For example, intuitively it seemed that very large aspect ratio concentrators would be harder to manufacture, and thus should be more expensive to fabricate. However, in the absence of input from an expert in industry or practical experience, it was easy to extrapolate the same scaling of volume of material and parts per mold size. This suggested on paper that added complexity was worth it for the added efficiency it brought, since our models did not incorporate associated added costs or diminished performance. Analogously, on the technical side, we initially included optical losses due to Fresnel reflections at interfaces but not absorption losses in solid components which were fairly transparent. This resulted in a design with just one air interface, and the rest of the light path was solid. Had we appropriately accounted for all relevant losses, we might have determined that an extra air-glass interface was worth higher efficiency in other areas. We design ourselves away from the problems we are aware of toward unknown ones over time. Thus without the costs of complexity in our model we drove ourselves toward greater complexity.

We did approach some plastic and glass optics manufacturers during the project to delve into manufacturing realities. We learned that there were concerns about the aspect ratio we were interested in both for extraction from the mold and for getting internal interfaces from injection molded parts cooling too much during production. In order to produce a CPC by injection molding a four-part mold would

have been necessary for highest accuracy. Alternatively, we could have opted for a two-part mold which was not single-point diamond turned, but milled by a more standard computer-numerical control (CNC) tool with lower precision and then polished. This process would have resulted in a greater deviation in the shape from the intended design and thus lower optical efficiency. Unfortunately, this expertise was external to our team. Having a team member with these skills, or whose primary role it was to explore scale fabrication, would have allowed us to more seamlessly work around manufacturing constraints.

5.5 Market Analysis

We undertook a market analysis to determine if there were any advantages or niches we might have to differentiate our spectrum-splitting photovoltaic technology from other photovoltaic and renewable technologies. New energy technologies have a difficult scaling problem. In order to get to a competitive cost, a large volume of production is required. For a hardware-based technology, this requires a lot of capital investment which a new company is unlikely to get for an unproven technology. Thus, entry markets are needed to establish cash flow and to build a case for the technology being low risk. For these entry markets, there should be a compelling unique feature of the product that makes them willing to take on more risk and pay more for the technology before it has scaled.

As we explored the potential for commercializing our technology we preferred the idea of licensing intellectual property associated with the design to a photovoltaic module manufacturer. We recognized, however, that the technology was too risky and not sufficiently validated for someone else to take a risk on it. Thus we envisioned starting a photovoltaic module manufacturing company.

In recent years, the costs of photovoltaic modules have gone down significantly. The balance of systems (BOS) costs including installation and racking hardware, however, have gone down much more slowly. Thus, increased efficiency can be an impactful way of bringing down overall system cost, and the biggest advantage of CPV is its high efficiency. In addition to higher peak efficiency, the number of hours of generation per day is slightly longer than a fixed tilt system due to dual-axis tracking. However, $/W cost of an installed system is higher than for a silicon system, and the risks are greater since the technology has not been as time-tested. The longer generating day is useful because evenings and early mornings are time when solar and wind are both less available and there is high demand. This

necessitates ramping up other power generating assets quickly, resulting in lower efficiency and higher cost. Recently, many utility-scale silicon installations have put flat panel silicon modules on one-axis trackers to achieve a similar lengthening of the generating day, eroding much of this benefit.

There are some other subtleties in comparing CPV and flat panel technologies. Two-axis tracking restricts packing fraction. Solar trackers shadow one another as the sun gets lower in the sky, so in order to minimize this, a piece of land with two-axis tracked HCPV arrays is not fully covered, so the technology is not necessarily more land efficient than flat panel solar. In fact, only about 25% of the land is covered compared to 80+% for flat panel. Additionally, as discussed in Section 1.4, concentration is based on restricting the angle range over which light is collected. With a high concentration, the collected angle can be as low as a 1° half-angle cone. Thus, on a cloudy day, the power output of a CPV installation plummets. This makes dry, sunny desert areas the optimal environment for CPV technology. Thus, there are factors such as limited geographical relevance and maximum packing fraction that make comparisons of energy yields or efficiency of CPV modules not an apples-to-apples comparison. There are regions of the world where conditions are favorable to CPV. These high DNI areas include the Middle East, North Africa, much of Australia, and the American southwest.

Additionally, there are some applications where the form factor and increased efficiency of CPV is an advantage. For example, in areas where totally shading land in fixed solar panels might damage the underlying natural vegetation, a tracked panel with a small footprint – just the base of the pedestal tracker – might be preferable. The additional risk adding by moving parts such as a tracker have been a barrier for CPV, especially since this technology has not scaled enough for the standardization that other aspects of the photovoltaics industry have experience in the past few years. Other possible entry markets would be land-constrained areas such as mines and islands in desert areas. There are also some ways to make in-roads to gain technical credibility earlier. Reliability is an important consideration for an untested technology. Early testing under the sun and reliability testing are necessary. We also got good advice to, from the get-go, only use materials that have already been certified for use in today's solar technologies.

The takeaway from our stakeholder interviews and participation in the Berkeley Haas School of Business Cleantech to Market program was that while the global photovoltaics market has recently grown significantly, the environment for a new

CPV technology is poor. There are currently 200 GW of solar energy production capacity available today with expected growth to 400 GW over the next few years. The new capacity added in 2013 and in 2014 was about 40 GW each year. This business has recently transitioned to a large industry, and it is not done growing. However, much of this growth has come through increased scale and standardization of c-Si products and consolidation with many smaller companies going out of business. Over the past five years concentrating photovoltaics has gone from a growing to a shrinking component of the overall photovoltaics market. During this time two of the largest CPV companies Soitec and Amonix have left CPV and essentially gone out of business, respectively. At the same time one-axis tracking unconcentrated silicon solar cells at the utility scale has become commonplace, undermining the benefit of the longer generating day that comes from a tracking technology. At the time of writing silicon is the single dominant photovoltaics technology and seems likely to stay in that position for some time to come. At the same time, it is not clear that the silicon market is profitable enough to keep up with growing demand for renewable energy generation, so space for alternatives may expand again in the future.

Conclusions

Nurturing a CPV technology today means waiting for the market to become favorable again. Ultimately there is a not a clear answer to whether or not our implementation of spectrum-splitting PV is an idea worth pursuing. Our cost modeling showed there was too much uncertainty to assess whether the cost and LCOE at scale would be competitive or not. Certainly there are remaining efficiency increases possible, and these are worth demonstrating. Additionally, we ran into many challenges in micro-optics fabrication which could be fruitfully studied. Whether or not to pursue commercialization, however, is a value judgment. The timeline for possible success is unknown, and the goalposts for measuring success are a moving target as silicon efficiency and price continue to improve. There is a risk that after decades of investment this technology could have successfully met all of its marks and still not be adopted at a wide scale because it is not sufficiently outperforming the incumbent technology.

At its best technoeconomic analysis keeps a technology grounded in reality. In the process of external validation we were forced to fill in gaps in our designs to build up a full picture of our system. Additionally, recognizing gaps in our knowledge about manufacturing in some cases led us to reach out to vendors and identify new methods

or learn about relevant limitations. However this process is time-consuming to do well. Thus, sometimes, at worst, this cost modeling exercise involved playing with numbers in a spreadsheet until they met a predetermined endpoint detached from reality. In our experience, the pay-offs of this analysis were the largest the two times we brought that manufacturing expertise directly into our team.

Chapter 6

HIGH-CONTRAST GRATINGS

Metamaterials are arrangements of more than one natural material at a small enough size scale that they combine to create a new effective medium with properties distinct from the components. This is most exciting when resultant properties are inaccessible with natural materials. Recently, metasurfaces, 2-dimensional metamaterials, have received much attention as an easy-to-fabricate subset of metamaterials, which still enable extraordinary properties including near-unity reflectance [39] and zero backscattering [40]. The generalization of Snell's Law to include phase discontinuities imparted by subwavelength scale interface features creates a framework for designing laterally macroscopic optics with sub-optical wavelength thicknesses [41].

My work has focused on a type of metasurface that has also been referred to as a high-contrast grating (HCG), which is the term I will use in this chapter. HCG, shown schematically in Figure 6.1a, are composed of a layer of high-refractive index semiconductor material patterned at a near-subwavelength size scale. That is, the characteristic length of the grating lies between $\frac{\lambda_0}{n_g}$ and $\frac{\lambda_0}{n_{med}}$, where the refractive index of the grating material is high and the refractive index of the grating medium. (Based on the following results and realistically accessible materials, I say $n_g \geq 3$ and $n_{med} \leq 1.55$.) These structures have been shown as a viable replacement to Bragg reflectors in Vertical Cavity Side Emitting Lasers thanks to their broadband, single polarization reflectivity [42]. Patterned crystalline silicon on a glass substrate was shown to have 74% peak reflectivity at normal incidence with >40% reflectivity at a 45° angle for use in color filters for displays. [43] The same group also demonstrated fabrication of their grating designs by nano-imprint lithography achieving 85% peak reflectivity centered at 620 nm for their red color filter. [44] Another group reported simulation results with polarization independent HCG reflectivity above 99% at normal incidence using crossed silicon stripes suspended in air which could be achieved by undercut etching.

The mechanism for high reflectivity is proposed to be modal interference within the grating layer preventing light from transmitting through. Since the subwavelength scale of the features renders non-0th diffracted orders evanescent, specular back-

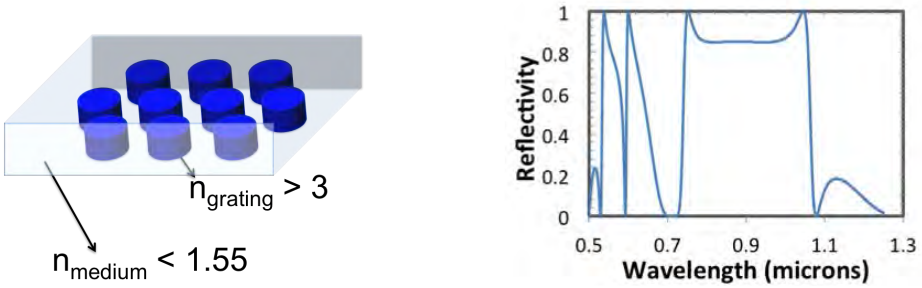

(a) (b)

Figure 6.1: (left) High-contrast grating schematic and (right) top-hat reflection profile of a simulated high-contrast grating.

reflection can go to near unity [45]. Reference [46] considers the grating layer as simultaneously a homogenized effective medium and a coupler for light into the homogenized effective medium. They identify the modes at work to be the Fabry-Perot resonance and the guided modes of the effective medium layer. The slowly varying Fabry-Perot resonance and the quickly varying waveguide mode interfere, producing a Fano resonance. The next higher order waveguide mode also interferes with the Fabry-Perot mode producing a Fano resonance with the opposite arrangement of its sharp and slow cut-offs. These two adjacent Fano resonances with opposite alignment give a top-hat like reflection profile which is exactly the desired characteristic for a band-stop filter. An example is shown in Figure 6.1b. Since the coupling into the guided waveguide mode is through the grating vector $\boldsymbol{G} = \frac{2\pi}{Period}$, as the incident angle deviates from normal, the lowest order coupling via diffracted orders ±1 splits, since the ±1 orders are no longer degenerate at non-normal incidence angles. Reference [47] demonstrated that the degree of symmetry of the tiling of grating elements is an important design characteristic of the gratings for the response of different polarization light and for more uniform performance with varying incident angle. A HCG based spectrum-splitting optic has been designed [48] with a test filter demonstrated for a Cassegrain device architecture [49]. A fabricated TiO_2 grating (with low refractive index contrast) showed poor performance relative to the designed specifications, and side-wall angles were found to be a sensitive parameter with deviations of just a couple of degrees from 90° sidewalls, giving large drop-offs in performance.

As described in Chapter 5, the main cost driver for a high efficiency design of the Polyhedral Specular Reflector spectrum-splitting design, detailed in Chapter 3, is the dichroic filter fabrication. High-contrast gratings are a promising alternative

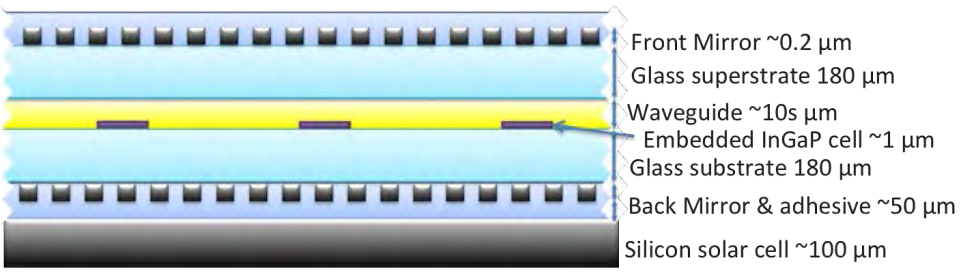

Figure 6.2: Spectrum splitting applications of high-contrast gratings include (right) Polyhedral Specular Reflector and (left) Tandem Luminescent Solar Concentrator.

for the splitting elements for cost and complexity reduction. In contrast to the slow fabrication process to deposit many-micron-thick distributed Bragg reflectors (DBR), the grating features can be made by a single sub-micron layer deposition followed by nanoimprint lithography and an etching processes, which can be done at large volumes. Additionally, sub-micron thicknesses mean less material per filter compared to a DBR. By virtue of the high refractive index contrast, the reflection band of HCG can also be more incident-angle tolerant. The requirement of many layers of materials and for material compatibility among successive DBR layers limits the use of layers with very different refractive index (e.g. ten pairs of GaP and SiO_2). Using HCG allows fewer components and less material per unit aperture area in a spectrum-splitting solar device, reducing cost and complexity. Figure 3.1e shows a schematic of the PSR in which the filters would be HCG. Early results on HCG showed a remarkable degree of angle insensitivity which prompted us to explore an additional application of HCG as a spectrum-splitting optical element in a Tandem Luminescent Solar Concentrator (TLSC) shown in Figure 6.2.

Tandem Luminescent Solar Concentrator

A luminescent solar concentrator (LSC) is a device which exploits the ability to expend energy to decrease entropy of light. This trade-off allows concentration of diffuse light, which without the energy trade-off violates the second law of thermodynamics. The definition of free energy, $\Delta G = \Delta H - T\Delta S \leq 0$, gives the minimum ΔH required to decrease the entropy of diffuse sunlight. Thus, solar light can be collected from a wide range of angles and downshifted by a dye or, as in our case, quantum dots. The photoluminescence of the quantum dots is trapped within a waveguide that has an aperture area of active semiconductor material which can collect the concentrated light. This collection aperture area is smaller than total input area of sunlight, implying a certain geometric concentration ratio. Traditional

LSC only use total internal reflection (TIR) to trap luminescence. Photoluminescent light hitting the front and back interfaces of the device are reflected back if the angle of incidence is beyond the critical angle as defined by Snell's law. Any light within the escape cone is lost. Traditional LSC thus have large losses and low efficiency.

Our strategy is to sandwich the quantum dot embedded waveguide between two band-stop mirrors with high reflectivity in the photoluminescence range and high transmission everywhere else to trap the photoluminescence in the waveguide. Shorter wavelength light will be transmitted through the top mirror into the waveguide, absorbed by the quantum dots, downshifted, and trapped by the mirrors. Longer wavelengths of light will be transmitted through both top and bottom mirrors to an underlying silicon solar cell. This tandem architecture has the potential to improve upon the efficiency of a silicon solar cell by converting higher energy photons in a cell which generates greater voltage. In executing this project, we will use near-unity CdS/CdSe core/shell quantum dots from the group of Paul Alivisatos at UC Berkeley and high-quality InGaP cells from the NREL III-V group.

Filter Specifications

Ideal filters for the PSR would have on average >85% reflectivity within the target band and >90% transmission for longer wavelengths. High transmission for longer wavelengths is important, since erroneously transmitted photons can still be converted in a lower bandgap cell but erroneously reflected light is lost completely in a higher bandgap cell. The seventh filter is a metallic mirror coated with a few dielectric layers to give full broadband reflectivity. However, to give shorter wavelength light a second chance to be absorbed in the following cell rather than the lowest, longpass rather than band stop filters would be most ideal for this design. Figure 6.3 shows the target specs for each of the seven PSR filters and TLSC mirrors vertically offset with the high values showing regions for which unity reflectivity is desired and the low value for each trace corresponding to zero reflectivity. The lighter colored portion of the trace for Filter bands 2 through 7 and TLSC Bottom shows the region in which the filter performance is non-critical though the indicated performance would be beneficial.

For the LSC application, the top and bottom mirrors have slightly different requirements. For the top mirror, the target is to let in as much light as possible while still maintaining high reflectivity at the peak of quantum dot photoluminescence to allow in as much incident power as possible. The back mirror target is slightly

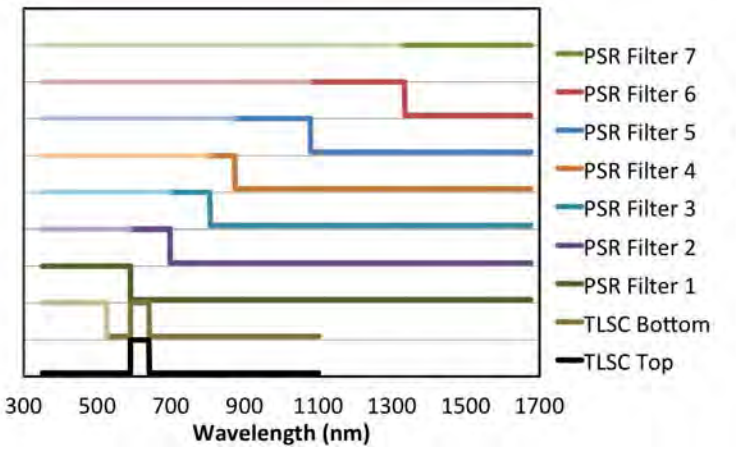

Figure 6.3: Target specifications for filters for the Polyhedral Specular Reflector and Tandem Luminescent Solar Concentrator.

more complex. The quantum dots absorb short wavelength light up to around 525 nm. The photoluminesced light peaks near 615 nm and has a bandwidth of about 50 nm. Thus the power in the spectrum between 525 nm and 590 nm light should pass through the back mirror to the underlying silicon cell. This is a high power portion of the spectrum, so failure to collect light in this spectral region would be detrimental. Additionally, high reflectivity for the short wavelength light absorbed by the quantum dots would allow it to pass through the waveguide twice. This dual pass absorption allows either improved absorption of the light toward the absorption edge of the quantum dots, i.e. just below 525 nm where the dot absorption is weaker, or allows the optical density of the waveguide to be as low as half of what it would need to be for full absorption in a single pass. This design freedom is advantageous but not required for high performance, and thus this portion of the bottom mirror filter specification is also a "want" rather than a "need".

6.1 High-contrast grating modeling

High-contrast grating modeling was done using the rigorous coupled wave analysis (RCWA) method [50] using commercial software program RSoft DiffractMOD. With this semi-analytical method, the steady state electric fields from plane wave illumination of an infinitely periodic, planar grating can be determined. The periodic, complex dielectric function of the grating layer is expressed as a Fourier series truncated to a finite number of terms. The electric fields in the grating layer and the media on either side of the infinite layer are represented as sums over the same series terms. Applying boundary conditions of Maxwell's equations at the interfaces be-

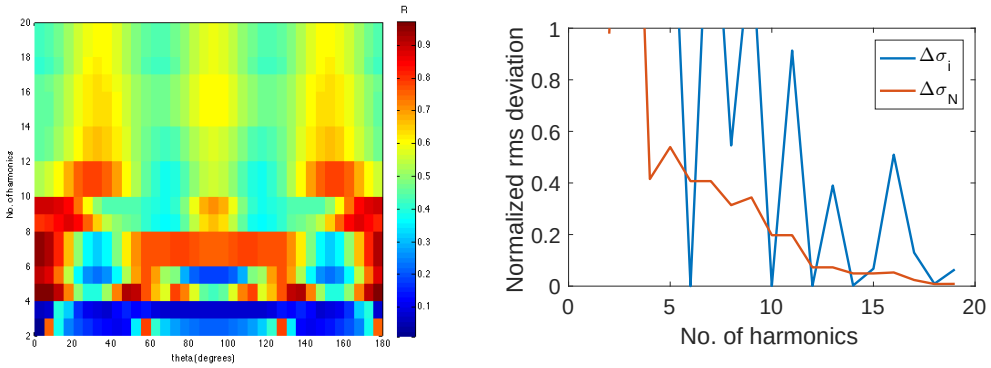

(a) (b)

Figure 6.4: Example of convergence testing simulation data (right) and (left) results of applying normalized rms deviation metric.

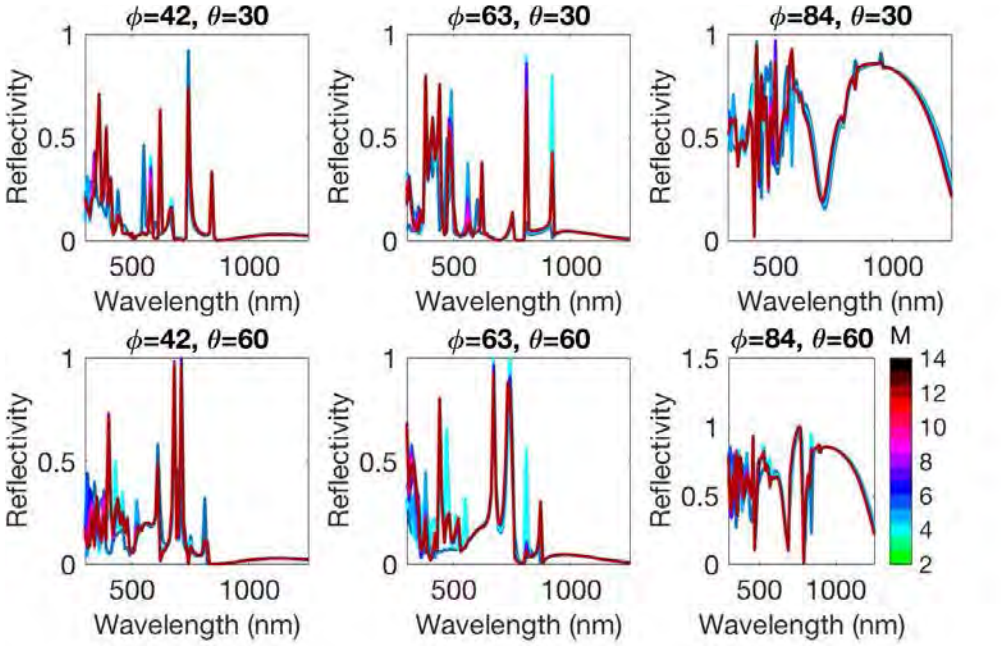

Figure 6.5: Broadband and multiple angle convergence testing results for n=2.7 grating in n=1.5 medium.

tween the grating and the incident and transmitting media gives a series of coupled equations which can be solved by a numerical matrix inversion, giving steady-state fields in all space. Related quantities such as transmission, reflection, absorption, and intensity in each diffracted order can be calculated from this. This method is faster than a full numerical solution to time-dependent Maxwell's equations.

The accuracy of RCWA simulations and the required computational time depend

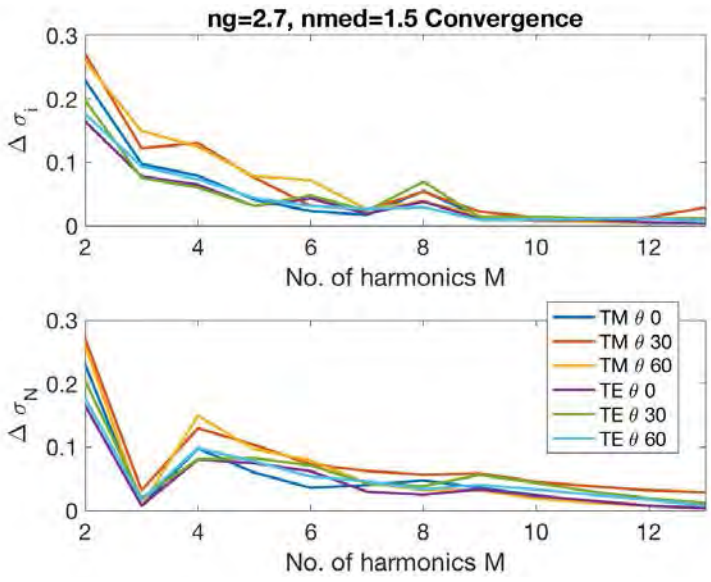

Figure 6.6: Normalized rms deviation of reflectivity of n=2.7 grating in n=1.5 medium.

on the number of Fourier terms, or harmonics. Convergence testing is required to obtain the appropriate number of harmonics for sufficiently accurate results. Simulations always give some answer. It is up to the modeler to evaluate whether the results are meaningful or not. Figure 6.4a shows a clear example of what can go wrong. These data show the reflectivity of TM polarization light from a grating composed of silicon nanopillars, hexagonally tiled with air as the grating medium. The wavelength $\lambda_0 = 600\ nm$, and polar angle of incidence $\phi = 30°$ with azimuthal angle θ ranging from 0° to 180° by 5° increments. The reflectivity is plotted as a function of the number of harmonics (from 2 to 20) included in the calculation. It is clear from this that simulations at a small number of harmonics significantly misconstrue grating reflectivity. Around twelve to fourteen harmonics the 60° rotational symmetry of the lattice becomes apparent.

In order to quantify the discrepancy and set a threshold for what level of variation is acceptable I use a pair of normalized root mean squared (rms) error metrics, defined as

$$\Delta\sigma_i = \sqrt{\frac{\sum_j \left(R_{i+1}(\lambda_j) - R_i(\lambda_j)\right)^2}{\sum_j R_i^2(\lambda_j)}} \tag{6.1}$$

$$\Delta\sigma_N = \sqrt{\frac{\sum_j \left(R_N(\lambda_j) - R_i(\lambda_j)\right)^2}{\sum_j R_i^2(\lambda_j)}}, \tag{6.2}$$

where $\Delta\sigma_i$ is the rms deviation between the results for i harmonics versus $i + 1$ harmonics, and $\Delta\sigma_N$ is the deviation between the results for i harmonics and N harmonics with N being a large number which is assumed to give fairly accurate results. The values of $\Delta\sigma_i$ and $\Delta\sigma_N$ for this case plotted in Figure 6.4b show that the value of $\Delta\sigma_i$ has not stabilized even for a large number (10-20) of harmonics, however, the relative error from $harmonics = 20$ drops below about 10% starting with harmonics=12. In general, as the ratio of wavelength to grating periodicity decreases, more harmonics are necessary. Thus for the broadband simulations necessary for spectrum splitting optical elements, I have done broadband convergence testing. An example is shown in Figure 6.5 where for different values of polar angle ϕ and azimuthal angle θ, reflection spectra are shown calculated using a range of number of harmonics. It is clear that the values change more as a function of the number of harmonics for shorter wavelengths. Smaller numbers of harmonics also produce some artificial resonances. Applying Equations 6.1 and 6.2 to these results yields Figure 6.6 indicating relative errors below 5% for ten or more harmonics. As seen in Figure 6.4a, however, plateaus in results do occur for certain numbers of harmonics, so it would be safer to additionally compare a subset of the results, to a simulation done with a much larger number of harmonics as well.

6.2 Results

The first simulations done were to confirm the relevance of the results and mechanism described in Reference [45] and [46] for both polarizations at oblique incidence with 2-dimensionally patterned gratings. Figure 6.7 shows the reflectivity as a function of wavelength and grating thickness for a grating composed of square-cross section pillars of crystalline silicon tiled on a square lattice with angle of incidence of 45° and polar angle set so that the plane wave is incident along one of the grating vectors with $n_{med} = 1$. The general characteristics of reflectivity match those for one-dimensional grating structures illuminated by a single polarization of light. First, for long wavelength light with $\lambda_0 > 1800\ nm$, there are weak Fabry-Perot resonance reflection peaks and valleys as the grating thickness changes. The shortest wavelength light ($\lambda_0 < 500\ nm$) is strongly absorbed, so the reflectivity in this region is low. For shorter intermediate wavelengths ($500\ nm \leq \lambda_0 \leq 1000\ nm$, the feature size of the grating is larger than the incident wavelength giving higher order diffraction. Thus, the specular reflectivity is low. Finally, the target high-contrast grating behavior is achieved for λ_0 between 1000 nm and 1800 nm where the lowest order guided modes of the grating layer are accessible. Here, modal

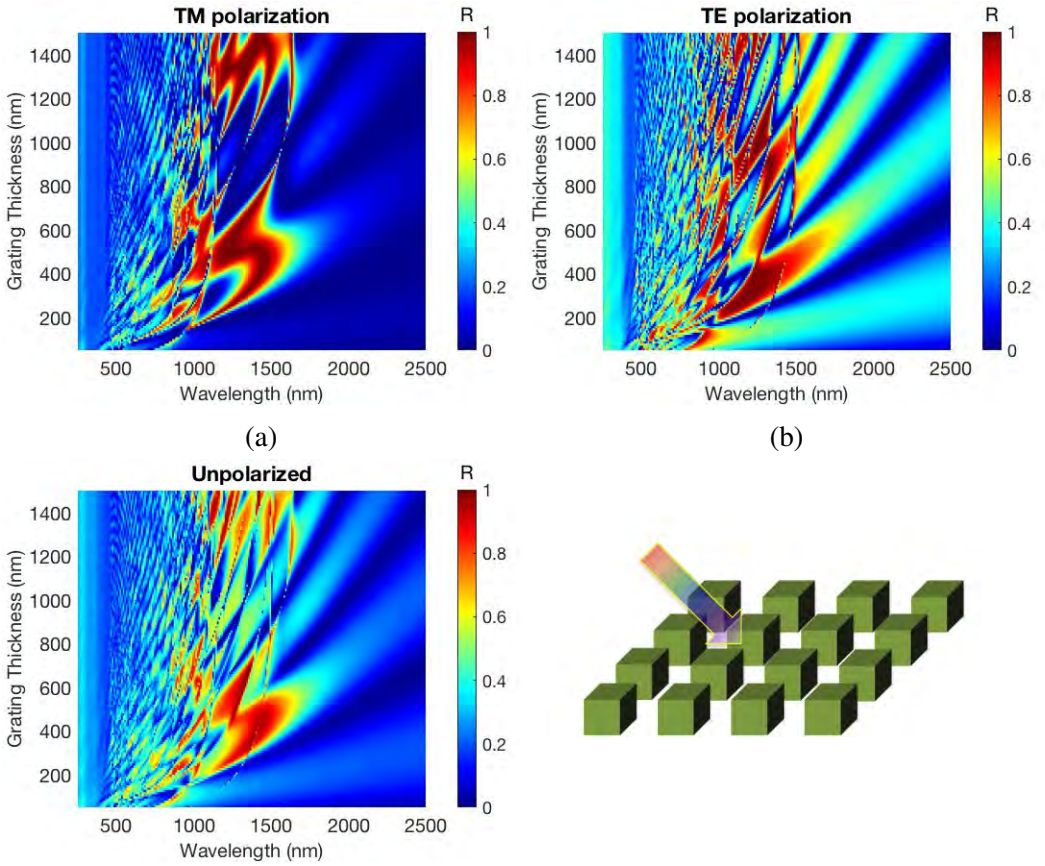

Figure 6.7: (top) Grating reflectivity for TM and TE polarized illumination on square cross-section pillars arrayed on square lattice with silicon grating material and $n_{med} = 1$. (bottom) Grating reflectivity for unpolarized light and grating schematic showing 45° broadband illumination.

interference gives high specular reflectivity.

Oblique incidence creates problems of having degenerate grating coupling vectors and polarization sensitivity, decreasing reflection peaks. As seen in Figure 6.7c, the strong reflection regions for TM and TE polarization do not overlap fully, giving lower maximum reflectivity values for unpolarized light. Higher refractive index of the grating medium decreases these effects since light is refracted toward normal incidence as it passes into the grating making the large range of angles in the medium have more similar reflectivity. The magnetic field intensity in a c-Si grating with air medium at the resonance wavelengths at normal incidence and 45° incidence, shown in Figure 6.8, indicate that in both cases similar modes are excited within the grating element. The longer wavelength resonance is an electric dipole resonance and the shorter wavelength resonance a magnetic dipole. The proximity of these two

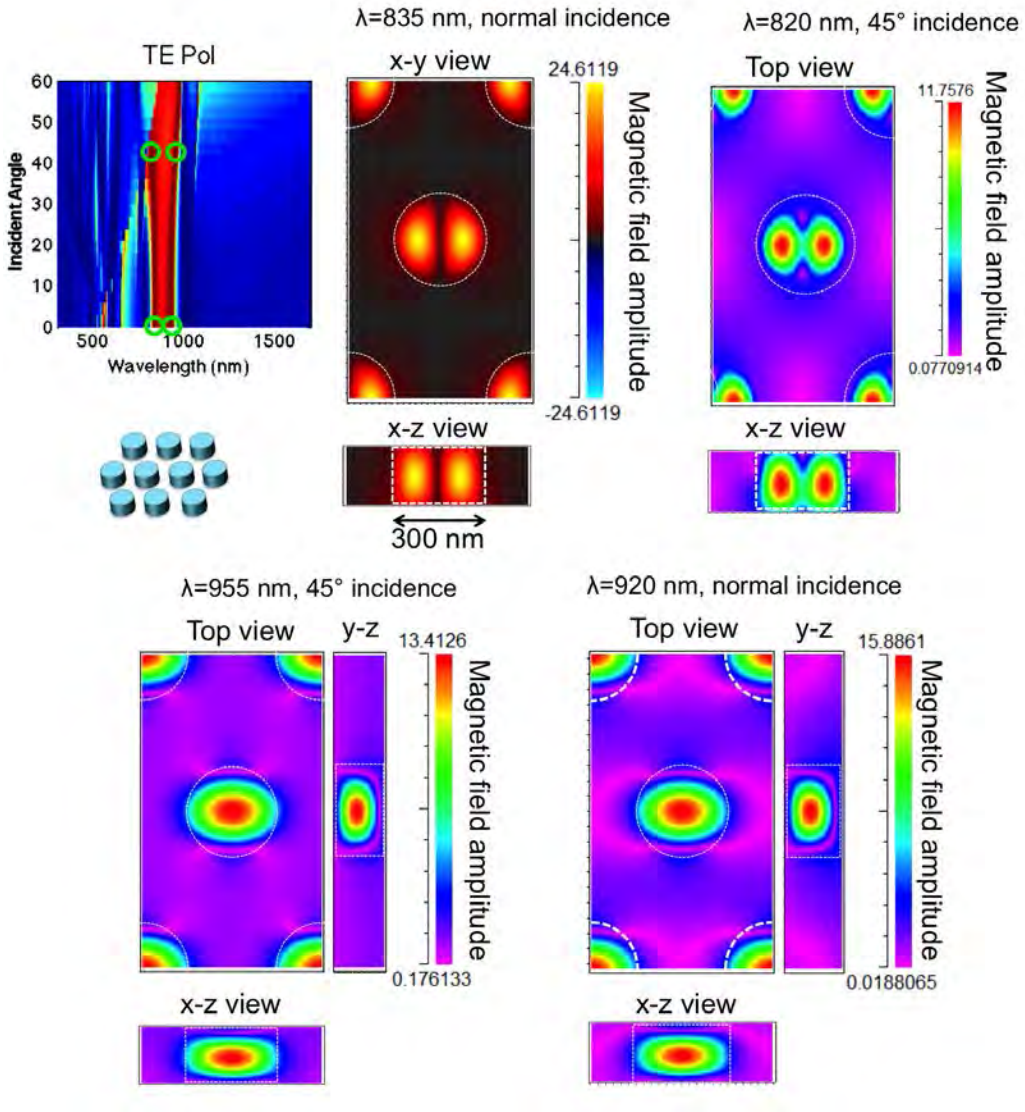

Figure 6.8: Magnetic field profiles of a grating on resonance illuminated by TE polarization light at normal incidence and 45° incidence showing very similar modes excited in both cases. The longer wavelength resonances appear to be electric dipole resonances while the shorter wavelength resonance is due to a magnetic dipole.

resonances gives the broadband reflectivity desired with $\frac{\Delta\lambda}{\lambda} \approx 0.11$. To additionally mitigate polarization sensitivity and the washing out of the top-hat reflection profile, we opted to use higher rotational symmetry gratings with circular cross-section pillars on a hexagonal lattice. There are five independent parameters for this grating geometry. The two materials parameters which can be changed are the refractive indices of the grating and of the medium. The three geometrical parameters are grating thickness (or pillar height), fill fraction (the percentage of the grating area

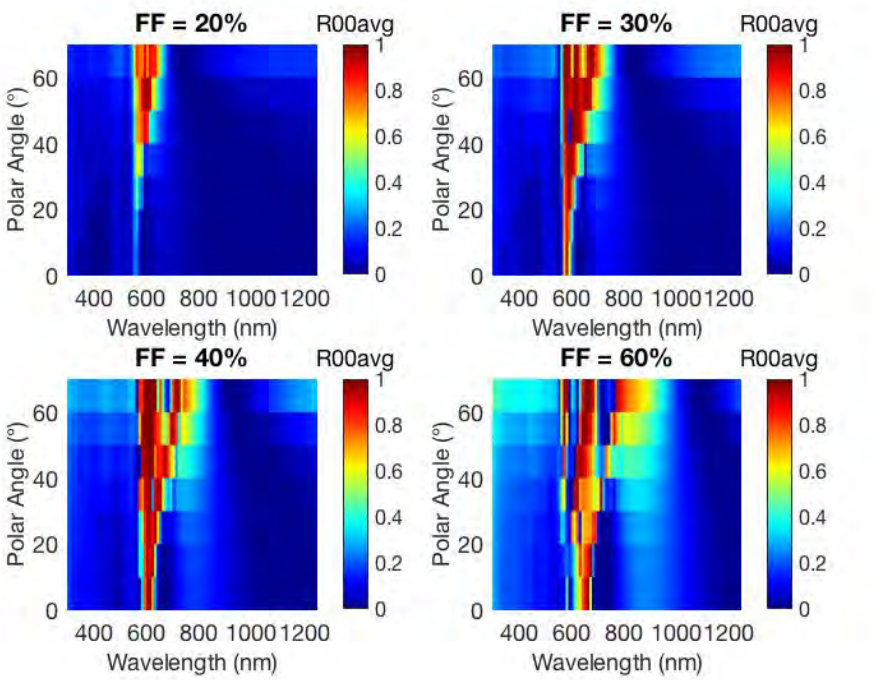

Figure 6.9: Reflectivity of AlSb high-contrast grating with $n_{med} = 1.5$, period=250 nm and grating thickness $t_g = 250\ nm$ for varying grating thickness fill fraction FF.

occupied by the grating material), and period of the grating. The fill fraction and period together fix a certain pillar diameter. (Any two among grating periodicity, fill fraction, and pillar diameter are independent.) Each of these parameters were varied to explore the grating design space for this geometry.

Figure 6.9 shows the reflection spectra for unpolarized illumination as a function of incident light versus incident polar angle for four different values of fill fraction with fixed period. The higher symmetry grating has more uniform reflection between the two polarizations as seen in >90% reflection peaks which require aligned reflection bands for the two polarizations. This AlSb grating in $n = 1.5$ medium shows that for low fill fractions, the reflection band is not strong, dipping below 40% near normal incident. As the fill fraction increases, the peak reflectivity goes up and the reflection bandwidth increases. Finally, at high fill fractions coupling between the adjacent grating elements leads to more complex mode profiles and reflectivity. The combination of parameters for FF=30% and FF=40% give quite desirable reflectivity. The effects of varying grating thickness are shown in Figure 6.10. Below the optimal thickness, the reflection modes present are dispersive and weak. At the optimal thickness, the modes interfere to produce an angle independent reflection. As the thickness increases beyond the optimal thickness, the two modes,

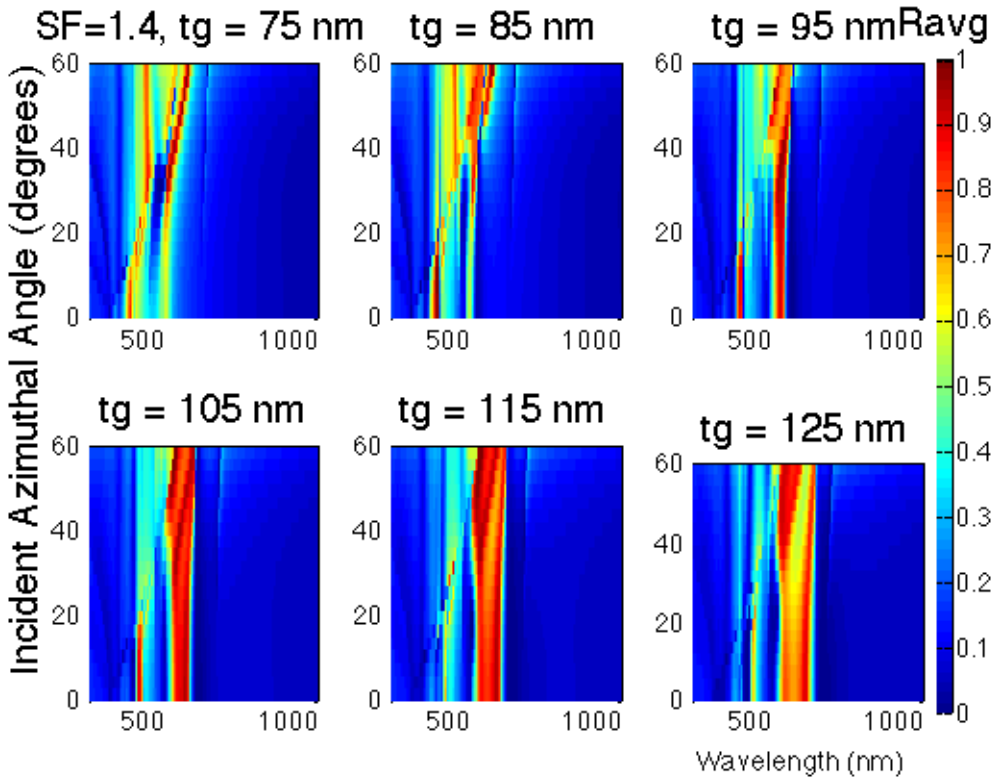

Figure 6.10: Reflectivity of a Si high-contrast grating with $n_{med} = 1$, pillar diameter=210 nm and FF=22.7% for varying grating thickness t_g.

shown above to be electric and magnetic dipole modes, move further apart giving a broader reflection band with lower reflectivity.

Maxwell's equations are scale invariant. Thus, for the wavelength range that refractive index of the grating material does not change much, the structure can be scaled up in all three-dimensions and show the same reflectivity for a proportionally scaled up wavelength. Figures 6.11b-d show the reflection characteristics of a silicon in air grating scaled up in size by factors of two, three, and four in each linear dimension. There are minor differences attributable to the dispersion of the silicon grating material over this wavelength range. Doing a fine re-optimization of the grating parameters around the scaled-up values could result in better performance.

Grating Materials

Grating materials must have high refractive index and low absorption throughout the wavelength range of interest. The inverse relationship of high bandgap energy materials having lower refractive index make this challenging. The refractive index and bandgap of a variety of possible materials are given in Figure 6.12. For

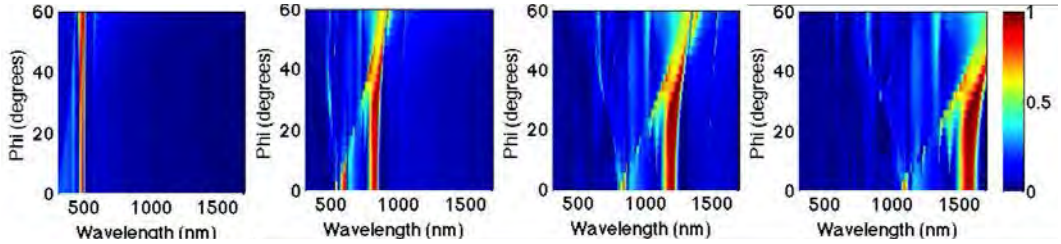

Figure 6.11: Reflectivity of silicon grating in n=1 medium with (left to right): $a = 300nm$, $r_{disk} = 75nm$, $tg = 70nm$; $a = 600nm$, $r_{disk} = 150nm$, $t_g = 140nm$; $a = 900nm$, $r_{disk} = 225nm$; $a = 1200nm$, $r_{disk} = 300nm$, $t_g = 280nm$. ©2015 IEEE

a photovoltaic technology to be scalable, as discussed in Chapter 5, cost is a key factor. Thus, materials such as TiO_2 or polycrystalline silicon, which have cheaper component elements and are widely used industrially, are preferable. Materials such as aluminum antimonide and gallium phosphide in contrast are typically epitaxially grown by slower processes on expensive substrates for precise electrical properties. Good optical properties can be achieved with lower quality materials, so it is possible that viable fabrication routes for polycrystalline or amorphous GaP or AlSb exist which give sufficient optical quality without high-cost growth. Generally, however, as a material moves from high-quality single crystalline to polycrystalline to amorphous structure, sources of deleterious absorption increase. From a performance standpoint, higher refractive index gives greater angle-independence and higher peak reflectivity as long as the reflection peak is at an energy below the material bandgap. Bandgap of 3.1 eV or greater would give low absorption across the entire solar spectrum of interest. The highest refractive index materials such as Si, AlSb, and GaP and common materials with high bandgap energy such are TiO_2 and silicon carbide are the most interesting candidates for high-contrast gratings based on these criteria.

The most favorable grating media are run-of-the-mill transparent dielectrics which are low cost and already validated for use in photovoltaics such as glass and PMMA with $n_{med} \approx 1.5$. However since refractive index contrast is a key factor in HCG performance, I also simulate media with $n_{med} = 1$ and $n_{med} = 1.2$. The former can be approximated by patterning "mushroom caps" of high refractive index by etching an undercut into the substrate material. Likewise $n_{med} = 1.2$, while not accessible with bulk materials, can be approximated using highly porous materials. Long-term practical concerns for porous and undercut etched materials include mechanical robustness and potential for dust and moisture incursion, both of which can be detrimental to the lifetime of a photovoltaic system that needs to maintain its

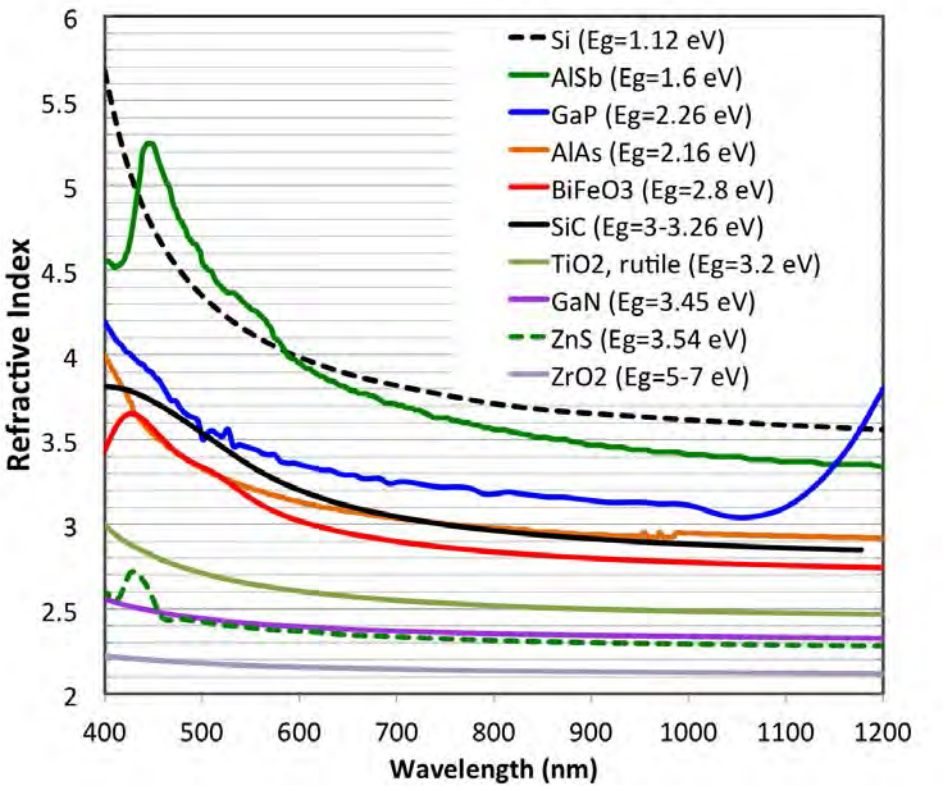

Figure 6.12: Candidate high-refractive index materials for high-contrast gratings.

performance over a 25-year timescale. Table 6.1 details the grating materials and media simulated. For the $n_{med} \approx 1.5$ simulations, a geometrical parameter sweep was done to quickly target a promising parameter range for high reflectivity. This included simultaneously sweeping grating thickness ($t_g = 50-1000\,\mu m$), fill fraction ($FF = 10\%-90\%$) for a fixed value of grating period, or grating width ($P \approx 250\,nm$ for AlSb, 240 nm for Si, and $width = 200\,nm$ for GaP). Specular and total reflectivity, direct and total transmission and grating absorption were simulated as a function of wavelength and incident polar angle. Even using an optimistic refractive index of $n_g = 2.7$ for TiO_2, the index contrast is too low to give angle-independent reflection bands (Figure 6.13). The data shown are representative of the best results from a thorough parameter sweep of grating fill fraction and thickness. The reflection features which are present vary in wavelength significantly as the angle of incidence changes. In addition to this high dispersion, the index contrast is not high enough to obtain high reflectivity across incident angles. A more realistic refractive index for TiO_2 deposited by methods suitable for large volume production is between 2.2 and 2.5. Thus, we must seek higher index materials or lower index media for our applications.

	Si	GaP	n=2.7	n=2.4	SiN	AlSb	AlAs
air	x	x	x	x			
n=1.2							
n=1.5	x	x	x	x		x	x
air/n=1.5 interface	x	x			x		

Table 6.1: High-contrast grating simulated materials combinations

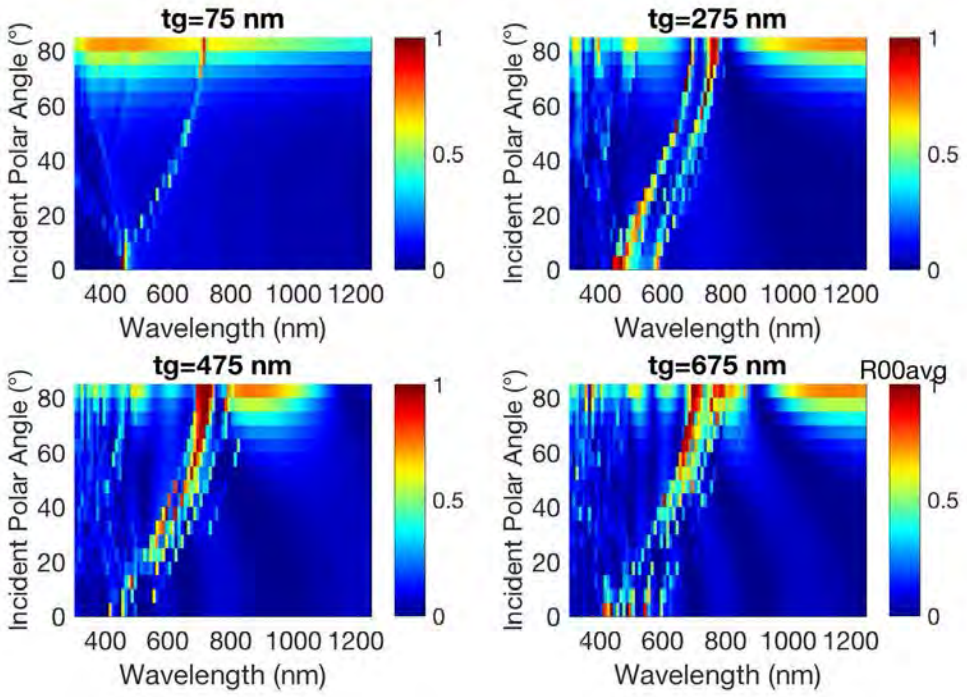

Figure 6.13: Reflectivity as a function of wavelength and incident angle for a dispersionless and lossless grating material with $n_g = 2.7$ and $n_{med} = 1.5$. Reflection bands are dispersive and do not have high reflectivity for a width range of angles.

Figure 6.14 shows the best polar angle-averaged reflectivity simulated for AlSb, Si and GaP gratings in an n=1.5 medium. Fully angle-averaged peak reflectivity will be slightly lower due to azimuthal angle variation which gives lower reflectivity for plane waves oriented along directions of lower density in the grating (e.g., oriented in the direction lying between the two lattice vectors). GaP shows higher transmission across the out-of-band regions due to its higher bandgap ($E_g = 2.26\ eV$). It absorbs strongly, however, below its bandgap. AlSb has an indirect bandgap at 1.6 eV with its direct bandgap strong absorption onset around 2.2 eV. Its refractive index of 4 at 600 nm gives better peak reflectivity making it a promising candidate material as well. Silicon has a comparable refractive index around 3.8 at 600 nm but has a

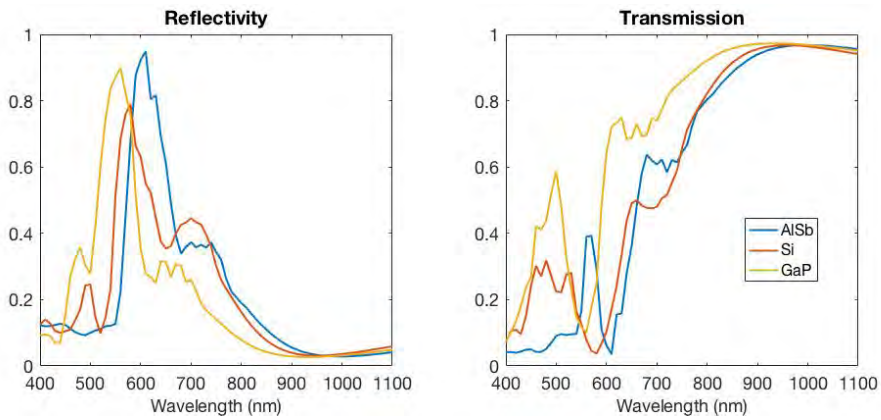

Figure 6.14: Hemispherically angle-averaged reflectivity and transmission as a function of wavelength for AlSb, Si and GaP gratings in $n_{med} = 1.5$.

lower energy indirect bandgap giving higher absorption at the target luminescence wavelength band.

The final steps in optimizing these best results are to repeat simulation for a higher the number of harmonics, include azimuthal angle variation, and fine-tune the values of the grating thickness, period, disk diameter, and fill fraction for optimization performance. This process will likely improve in-band reflectivity and out-of-band transmission slightly. The target specs of >99% in-band reflectivity and >97% out-of-band transmission, however, remain elusive. We need to consider more significant design changes to approach these values.

One option for increasing peak reflectivity above what is seen in Figure 6.14 is to stack more than one HCG. Figure 6.15a shows the reflection of a single GaP grating as well as two GaP gratings one on top of the other with a large enough spacer to treat the reflectivity of each layer independently. Thus we can estimate the reflectivity change due to the additional layer with $\Delta R = T \times R \times T$ where the additional reflectivity comes from light which transmits through the first grating, gets reflected off the second and finally gets transmitted through the first grating again, back into the waveguide. As seen from this expression, unfortunately stacking pays off less and less as the initial reflectivity gets better. 70% reflectivity becomes 76% while 90% becomes 91%. Even worse, the shoulder of reflectivity for long wavelengths is at the peak for highest ΔR, increasing unwanted reflectivity from 30% to 45%. Stacking two layers close enough to give optical coupling between them may give different results and remains to be simulated.

Another possibility is exploiting total internal reflection by placing the grating near

an air-glass interface. Figure 6.15b shows the same GaP grating fully immersed in an $n = 1.5$ medium with an air interface a half-wavelength ($\frac{\lambda_0}{2*n_{med}}$) away from the grating. The grating is embedded a half-wavelength deep just inside the glass semi-infinite half at an air-glass interface. The presence of the interface increases in-band peak reflectivity when illuminated from the glass side by $14.5\%_{abs}$. Thus the angle-averaged reflectivity experienced by photons luminesced by the quantum dots improves. Additionally the reflectivity for long wavelength illumination which must pass through the front and back mirrors to reach the underlying silicon solar cell remains largely unchanged. Unless long wavelength light is scattered as it enters the waveguide, the angular spread when it reaches the back mirror from the waveguide will the the same refracted angle spread as it has upon entering from the air side. The relevant reflectivity value will thus still be the lower air-side reflectivity. Incorporating the total internal reflection of an air-glass interface also requires using a different criterion for selecting the best HCG grating. Total internal reflection perfectly reflects light outside the escape cone of 41° for an air/n=1.52 interface. Thus, the HCG's performance now depends on its performance up to 41° not a full hemispherical angle-average.

HCG in the Polyhedral Specular Reflector

Individual HCG have reflection bands too narrow to serve as band-stop filters for the PSR, let alone longpass filters. As described above stacking gratings is not very effective at increasing already high peak reflectivity. However, it is more effective at widening a reflection band. Figure 6.16 shows two of the seven filter bands approximated by silicon in air gratings from those shown in Figure 6.11 along with some intermediate scaling. For band 5 requiring reflectivity between 874 nm and 1078 nm, two gratings are stacked with the combined reflectivity given by $R_{total} = R_1 + T_1^2 \times R_2$ and combined transmission by $T_{total} = T_1 \times T_2$. The base gratings do not have high reflectivity at 45°, so the structure would need reoptimization for the appropriate angle range. In the images shown peak reflectivity occurs around 20° angle of incidence. As seen in Figures 6.9b and 6.9c, near-unity, polarization averaged reflectivity can be obtained at 45°. The biggest downside of stacking gratings is diminished transmission for out-of-band wavelengths. It remains to be seen how much benefit can come from adding antireflection layers onto the resonant structures to cut down on long-wavelength Fabry-Perot reflections. In all likelihood, these gratings would find better applications in alternate spectrum splitting geometries than the PSR for which out-of-band transmission efficiency is

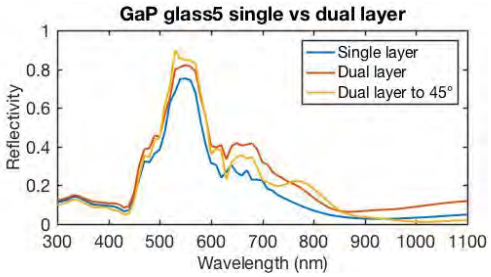

(a)

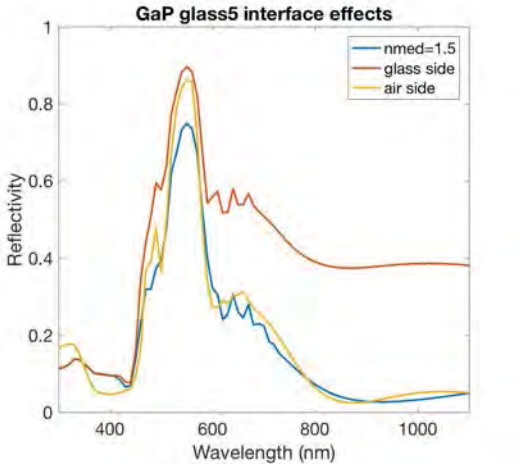

(b)

Figure 6.15: Reflectivity of (left) GaP HCG near an air/glass interface, and (right) GaP pillars topped with SiN HCG.

very important to overall performance.

Evaluating mirrors for tandem luminescent solar concentrator

While peak reflectivity is easy to read off a plot, assessing the performance of one mirror against another in the trade-off between high in-band reflectivity and high out-of-band transmission benefits from a more holistic metric. Thus, a figure of merit to weight different spectral and angular ranges by their relative importance is needed. Ultimately, I sought a figure of merit to closely approximate the amount of power converted in the correct cell. In order to estimate this, first, I assume that solar illumination over a 60° half-angle cone of angles of totally diffuse light can be collected. Thus, I can integrate the mirror reflectivity over this range, angle averaging the output of my RCWA simulations $R(\theta_{ext}, \phi, \lambda)$ to get

$$R_{ext}(\lambda) = \int_0^{\frac{2\pi}{3}} R(\theta_{ext}, \phi, \lambda) \cos\theta \sin\theta d\theta d\phi, \tag{6.3}$$

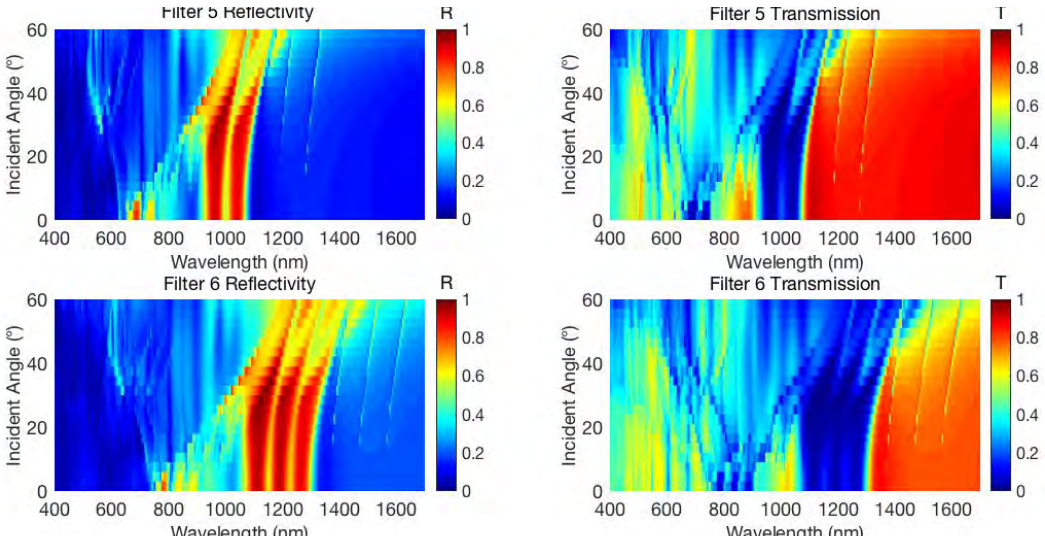

Figure 6.16: Multiple silicon in air structures stacked to generated wider reflection bands for PSR band 5 on top and band 6 on the bottom.

where ϕ is the polar angle and θ the azimuthal angle and R mirror reflectivity. I similarly angle average the mirror from the waveguide side, this time considering uniform illumination from the quantum dots embedded in the LSC waveguide over a whole hemisphere to get

$$R_{int}(\lambda) = \int_0^{\pi} R(\theta_{int}, \phi, \lambda) \cos\theta \sin\theta d\theta d\phi. \tag{6.4}$$

Now I define the Figure of Merit (FoM) to be

$$FoM(n) = \frac{P_{Si} + P_{InGaP}(n)}{Incident\ Solar\ Power}, \tag{6.5}$$

where the silicon cell power P_{Si} is defined as

$$Power = V_{OC} \times FF \times \sum_i Flux(\lambda_i) \tag{6.6}$$

using properties of a high quality silicon heterojunction HIT cell to give the open circuit voltage $V_{OC} = 730\ mV$, fill fraction $FF = 0.8$, and short-circuit current is estimated as

$$J_{SC,Si} = \sum_{\lambda=525\ nm}^{1200\ nm} AM1.5G(\lambda_i) \times T_1(\lambda_i) \times T_2(\lambda_i) \times EQE_{Si}(\lambda_i),$$

where I only consider the wavelength range 525 nm to 1200 nm which is the intended band for the silicon cell. $EQE_{Si}(\lambda_i)$ is for a Kaneka HIT cell from [51]. The flux reaching the silicon cell is defined as the sum of the AM1.5 global reference

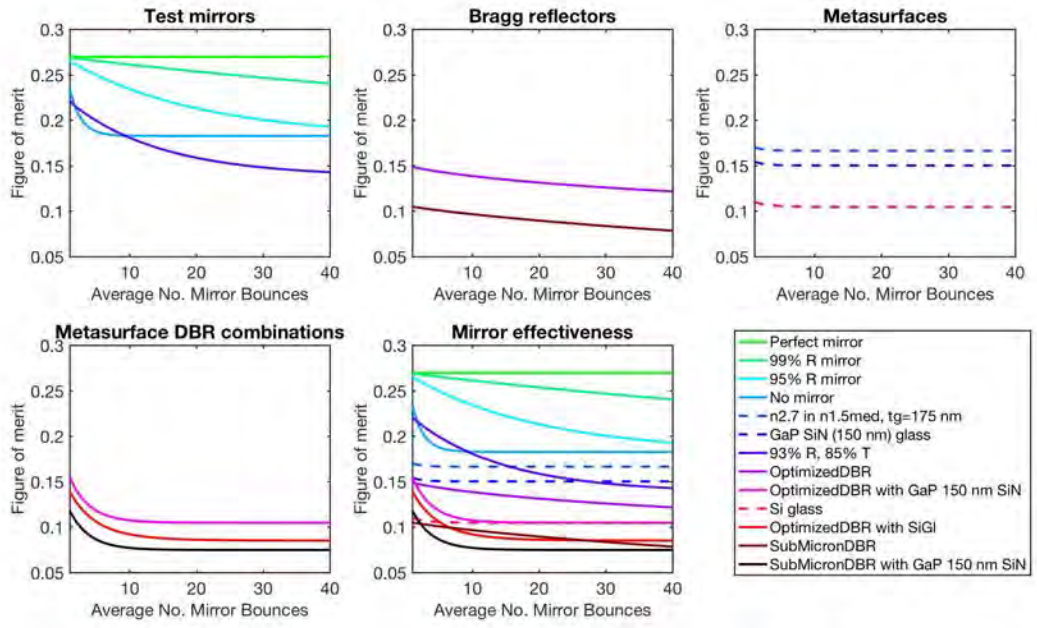

Figure 6.17: Figure of merit for Tandem Luminescent Solar Concentrator design for ideal filters, Bragg reflectors, high-contrast gratings, and combinations of the two as a function of average mirror bounces.

spectrum transmitted through mirrors 1 and 2 and converted by the silicon cell. The power of the InGaP top cell P_{InGaP} is a function of the average number of mirror bounces which depends on the architecture of the device. Analogous to P_{Si}, it is defined by equation 6.6 as the product of InGaP voltage ($V_{OC} = 1.4\ V$), fill fraction ($FF = 0.85$), and current, calculated by

$$Flux_{InGaP}(\lambda_i) = PL_{QD}(\lambda_i) \times (R_{int}(\lambda_i))^n, \tag{6.7}$$

where n is the average number of mirror bounces and the quantum dot photoluminescence $PL_{QD}(\lambda_i)$ is

$$PL_{QD}(\lambda_i) = \left(\sum_{\lambda=300\ nm}^{525\ nm} T_1(\lambda_i) \times AM1.5G(\lambda_i) \times A_{QD}(\lambda_i) \right) \times \frac{PL(\lambda_i)}{\sum_i PL(\lambda_i)}. \tag{6.8}$$

The quantum dot absorption is assumed to be a step function with no absorption for $\lambda > 525\ nm$ and perfect absorption at shorter wavelengths. The InGaP cell is additionally assumed to have unity EQE. All short wavelength photons which are transmitted through the top mirror are thus assumed to be absorbed by a quantum dot and re-emitted. The final factor in equation 6.8 redistributes the total number of re-emitted photons into the experimental photoluminescence spectrum of the

quantum dots. The number of these re-emitted photons which are retained in the waveguide and thus converted by the InGaP cell depends on the mirror reflectivity over the wavelength range of photoluminescence and the average number of mirror bounces.

The results of this figure of merit can vary based on the choices of the open-circuit voltage, FF and EQE of each cell as well as the cutoff off wavelength and average number of mirror bounces. Using the listed assumptions above and calculating the FoM as a function of mirror bounces from 1 to 40 for a number of mirrors, we get Figure 6.17. Our Monte Carlo modeling performed by David Needell indicates the number of mirror bounces is a strong function of mirror quality with as many 500 bounces for a perfect mirror or as few as three for a poor mirror. As indicated in the figure, neither the currently designed Bragg reflectors optimized by Colton Bukowsky or the HCG discussed in this chapter or combinations of the two have yet to reach the performance of notional mirrors with flat angle-independent reflectivity in-band and transmission out-of-band. In general, the FoM shows that metasurfaces cannot be use for the top mirror as the absorption of light between 400 nm and 525 nm for silicon, AlSb and GaP is too high. This is evident in the flat Figure of Merit for the HCG metasurfaces which do not change as a function of the number of mirror bounces. The power converted by the metasurface mirror TLSC comes primarily from light transmitted directly to the silicon cell, since the light that should be collected in the top cell which would be susceptible to loss at higher numbers of mirror bounces is largely absorbed by the HCG. In contrast, the DBR mirrors have high in-band reflectivity and no short-wavelength absorption (they assume lossless dielectric materials). Thus even after a large number of mirror bounces, the FoM value has not plateaued. There is still energy collected by the InGaP which could be lost at a higher number of mirror bounces. However the value of the FoM is low due to low out-of-band transmission to the underlying silicon cell.

Among the DBR/HCG combinations shown with a DBR front mirror and a HCG back mirror, the current results seem to combine the worst qualities of each mirror. The trapped photoluminescence is lost in under 10 mirror bounces while the transmission to the silicon cell is low. In part this is due to the reflection peaks of the HCG being centered at slightly too short wavelength to be well aligned with the quantum dot photoluminescence as shown in Figure 6.15. This is a matter of slightly scaling up the gratings to give reflectivity that is well aligned with the emission peak. Additionally, prioritizing transmission to the silicon cell can give the combinations

higher efficiency potential. This path is the one we are currently pursuing for this design.

6.3 Summary and Next Steps

Rigorous coupled-wave analysis simulations of reflection and transmission efficiency of high-contrast gratings were done. The gratings were evaluated for use as spectrum-splitting optical elements in the PSR and the Tandem Luminescent Solar Concentrator. These high-refractive index, near-subwavelength-scale gratings were shown to have relatively angle-independent reflection peaks. Paired Fano resonances give breadth to the reflection band. The bandwidth, peak reflectivity and angle insensitivity improved with higher refractive index contrast between the grating material and medium. Also, lower extinction coefficient gave higher peak reflectivity. Thus AlSb and GaP are optimal materials with low absorption in the visible range and high refractive indices. Finally, it was shown that stacking additional patterned layer and placement of air interfaces could improve performance. Appropriately sized reflection bandwidths are possible for the longer wavelength spectral bands of the PSR. The out-of-band transmission however is not high enough to give high device efficiency. Achieving at least >85% in-band reflectivity and >90% out-of-band transmission overall from the stacked gratings would enable 40% module efficiency. The much more stringent requirements for the narrower band tLSC filters require >99% in-band reflectivity and >97% out-of-band transmission to improve upon the conversion efficiency of a high quality silicon cell alone. The absorption in materials with high enough refractive index for promising reflectivity was shown to be too much to use the current high-contrast gratings as the front mirror in a tLSC. The best-to-date peak angle-averaged reflectivity is 95% for an AlSb grating in n=1.5 medium with about 80% long wavelength transmission.

Next steps targeting incremental improvements should focus on increasing peak reflectivity, decreasing long wavelength Fresnel reflections and short-wavelength diffraction. In part this should be done by finely adjusting the geometrical parameters of gratings. Additionally, simulations should be repeated at a higher number of modes to get refined results. Application of optimization methods to reduce manual parameter sweeps could significantly speed up this design process. Slight randomization in position of grating elements should be tested. It is possible that this would decrease higher order diffraction efficiency (i.e., short wavelength diffraction) without strongly interfering with the lower order resonances which create the high-contrast grating reflection band. Studies should be done permuting the shape

of the individual grating resonators to check the effect. Literature has shown high sensitivity of HCG reflection to grating element shape such as sharp corners. While it is likely to be low especially as the refractive index goes up, this check is necessary as fabrication errors are inevitable, and an understand of their influence on performance should be quantified for large scale applications. Fabrication of gratings alongside further simulation to confirm tolerances is also necessary. Among other factors, evaluating whether or not the AlSb indirect bandgap of $E_g = 1.6\ eV$ is absorbing too in the photoluminescence wavelength range for effective use is a high priority. Finally, improvements to the figure of merit include accounting for the fact that not all light hitting a solar cell in an average low DNI environment is uniformly distributed across a hemisphere. This assumption penalizes our technology significantly compared to the peak efficiency of a conventional solar cell which is measured at normal incidence and should be addressed.

To move the needle on HCG performance for spectrum splitting photovoltaics, different geometries and materials combinations need to be explored. Moving beyond variations of the single patterned layer grating, geometrical combinations of HCG and DBR remain to be fully explored. For example, while optically independent stacked HCG layers did not give improvements, optically coupled stacked layers have not been explored. In overall device design, high-contrast gratings should be explored as light trapping optical elements in traditional luminescent solar concentrators. Such single junction luminescent solar concentrator designs would reduce the transmission problem to just that of short wavelength light rather than both short and long wavelength light. Additionally, short-wavelength transmitted diffracted orders could be less of a problem in such an architecture. Finally, it remains to be investigated whether there are scalable methods of obtaining GaP and AlSb and if there are any materials use concerns for AlSb for large-scale deployment in photovoltaics.

Regarding materials selection, ways of exploiting high refractive index TiO_2 in an air medium seems to be the last hope for possibly using HCG as a front mirror or a short wavelength filter in a photovoltaic application. Design work remains to be done with this material pair. Any future materials innovation in transparent, high refractive index material could be fruitfully applied to high contrast gratings, for example development of a germanium carbide with high refractive index and lower bandgap than SiC. Regarding high efficiency luminescent solar concentrator work, a key enabling technology will be high quantum yield, near infrared quantum dots.

This would enable both higher efficiency single junction and tandem luminescent solar concentrators by allowing the trapped and thus rejected spectral window to move away from the peak of the solar spectrum. A quantum dot with emission near λ=800 nm would pair well with GaAs solar cells, either as a single junction or as a top junction for a tandem cell with silicon.

Chapter 7

SUMMARY AND OUTLOOK

The goal of this thesis was to push the boundaries of photovoltaic efficiency in response to both current market forces and the scientific imperative to test the limit. Today's current photovoltaic efficiency record for a cell is 46% and for a module is near 39%. We aimed to use spectrum-splitting photovoltaics, in which broadband sunlight is split into separate frequency bands and sent to solar cells of different bandgap. In the best case, well-separated photons generate the highest possible voltage leading to higher overall solar-to-energy conversion efficiency, bringing up the peak power conversion efficiency and lifetime energy production which contribute to lower the $/W and LCOE, respectively.

The Holographic Spectrum Splitter design used volume phase holographic diffraction gratings to split white light into four spectral bands. Each band would be converted by a dual junction tandem multijunction solar cell allowing eight junctions with a four-way split. The design had a high efficiency potential of >37%, just eking out a record efficiency. The design complexity made simpler, slightly less efficiency designs more favorable. The underlying logic of optically recordable spectrum-splitting optical elements with the ability to diffract all transmitted light into a single diffracted order remains sound, however. Sinusoidal diffraction efficiency profiles and diffraction angle dispersion must be address for higher efficiency.

High-contrast gratings were shown to be an interesting, angle-independent single layer alternative to Bragg reflectors in photovoltaic applications. High refractive index combined with low loss was shown to be the key factor in their performance. This difficult combination makes short wavelength visible high-contrast gratings an unrealized technology. Given the very high demands of the Tandem Luminescent Solar Concentrator, alternative applications may be better suited for HCG use, such as multispectral imaging or color filtering for imaging. Similarly, the TLSC concept would be better deployed to improve the efficiency of mediocre Si solar cells rather than high efficiency silicon cell for which the presence of the waveguide diminishes the performance of an already excellent bottom cell. Similarly, applications paired with lower bandgap quantum dots and lower bandgap cells embedded in the waveg-

uide have the potential to relax the current narrow range of specs for the HCG to give high efficiency.

The Polyhedral Specular Reflector design still has potential to be a world record efficiency device. The solid, index matched optical path with embedded DBR filters results in strikingly high efficiency spectrum splitting. However, concentration via CPC was attempted at a challenging size scale. Our path lengths were long enough that plastic materials absorbed considerable. At the same time the curvature was nearly impossible to realize in glass. Additionally, the difficulty of developing in-house processing capabilities for seven solar cells were underestimated. While GaAs and InGaP solar cells are commonly manufactured, the five additional bandgap cells were new territory for our team. Finally, our designs required micro-assembly and precision optics fabrication tools that pushed the boundaries of what is currently possible. Advances in these areas would benefit the future development of a photovoltaic technology like the Kirigami PV spectrum-splitting design. Taking on these large challenges simultaneously hampered our ability to realize a record breaking spectrum splitting efficiency despite having a design that could get there.

Overall, this thesis shows that multiple designs of spectrum-splitting photovoltaics has the potential to surpass the efficiency of today's state-of-the-art flat-panel and CPV technologies. Efforts to take the PSR concept and develop a commercial solar technology were hampered by a combination inability to realize all of the designed bandgaps of cells in the allotted time, lack of high precision glass/plastic molding and microassembly capabilities to iterate our prototyping process faster and by external market forces. In today's market the potential for higher efficiency in a new form is not as compelling as it had been earlier in the past decade when silicon raw materials prices spiked and before silicon grew sufficiency to enjoy many incumbency advantages. Whether or not the market opens again to concentrating photovoltaics or not remains to be seen. While the highest efficiency cells and modules are CPV, the technology may have missed its moment to grow enough to reap the economies of scale that would allow it to drop in price to a level competitive with silicon. If so, the future of spectrum-splitting PV innovation will lay with technologies like the TLSC which could integrate into today's silicon photovoltaics industry.

BIBLIOGRAPHY

[1] W. Shockley and H. J. Queisser, "Detailed balance limit of efficiency of p-n junction solar cells," *J. Appl. Phys.*, vol. 32, pp. 510–519, 1961.

[2] Renewable Resource Data Center (RReDC), National Renewable Energy Laboratory. (2016). Best research-cell efficiencies, [Online]. Available: `http://www.nrel.gov/ncpv/images/efficiency_chart.jpg` (visited on 10/09/2016).

[3] A. Polman and H. A. Atwater, "Photonic design principles for ultrahigh-efficiency photovoltaics," *Nat. Mat.*, vol. 11, pp. 174–177, 2012.

[4] R. R. King, D. Bhusari, A. Boca, D. Larrabee, X.-Q. Liu, W. Hong, C. M. Fetzer, D. C. Law, and N. H. Karam, "Band gap-voltage offset and energy production in next-generation multijunction solar cells," *Prog. Photovolt.: Res. Appl.*, vol. 19, pp. 797–812, 2011.

[5] J. F. Geisz, R. M. France, I. García, M. A. Steiner, and D. J. Friedman, "Device characterization for design optimization of 4 junction inverted metamorphic concentrator solar cells," in *10th International Conference On Concentrator Photovoltaic Systems: Cpv-10, AIP Conference Proceedings*, 2014.

[6] E. C. Warmann and H. A. Atwater, "Energy production advantage of independent subcell connection for multijunction photovoltaics," *Energy Science and Engineering*, vol. 4, pp. 235–244, 2016.

[7] J. D. McCambridge, M. A. Steiner, K. A. E. Blair L. Unger, E. L. Christensen, M. W. Wanlass, A. L. Gray, L. Takacs, R. Buelow, T. A. McCollum, J. W. Ashmead, G. R. Schmidt, A. W. Haas, J. R. Wilcox, J. V. Meter, J. L. Gray, D. T. Moore, A. M. Barnett, and R. J. Schwartz, "Compact spectrum splitting photovoltaic module with high efficiency," *Prog. in PV: Res and Appl.*, vol. 19, pp. 352–360, 2011.

[8] X. Wang, N. Waite, P. Murcia, K. Emery, M. Steiner, F. Kiamilev, K. Goossen, C. Honsberg, and A. Barnett, "Lateral spectrum splitting concentrator photovoltaics: Direct measurement of component and submodule efficiency," *Prog. Photovolt.: Res. Appl.*, vol. 20, pp. 149–165, 2012.

[9] S. van Riesen, M. Neubauer, A. Boosa, M. M. Rico, C. Gourdel, S. Wanka, R. Krause, P. Guernard, and A. Gombert, "New module design with 4-junction solar cells for high efficiencies," in *11th International Conference on Concentrator Photovoltaic Systems: Cpv-11, AIP Conference Proceedings*, 2016, pp. 100006-1–100006-8. DOI: `doi:10.1063/1.4931553`.

[10] G. Kim, J.-A. Dominguez-Caballero, H. Lee, D. Friedman, and R. Menon, "Increased photovoltaic power output via diffractive spectrum separation," *Phys. Rev. Lett.*, vol. 110, p. 123 901, 2013.

[11] M. Stefancich, A. Zayan, M. Chiesa, S. Rampino, D. Roncati, L. Kimerling, and J. Michel, "Single element spectral splitting solar concentrator for multiple cells CPV system," *Opt. Express*, vol. 20, pp. 9004–9018, 2012.

[12] B. Mitchell, G. Peharz, G. Siefer, M. Peters, T. Gandy, J. C. Goldschmidt, J. Benick, S. W. Glunz, A. W. Bett, and F. Dimroth, "Four-junction spectral beam-splitting photovoltaic receiver with high optical efficiency," vol. 19, pp. 61–72, 2011.

[13] J. C. Goldschmidt, C. Do, M. Peters, and A. Goetzberger, "Spectral splitting module geometry that utilizes light trapping," *Sol. Energy Mat. Sol. Cells*, vol. 108, pp. 57–64, 2013.

[14] A. G. Imenes and D. R. Mills, "Spectral beam splitting technology for increased conversion efficiency in solar concentrating systems," *Sol. Energy Mat. Sol. Cells*, vol. 84, pp. 19–69, 2004.

[15] A. Mojiri, R. Taylor, E. Thomsen, and G. Rosengarten, "Spectral beam splitting for efficient conversion of solar energy—a review," *Renewable and Sustainable Energy Reviews*, vol. 28, pp. 654–663, 2013.

[16] D. Zhang, M. Gordon, J. M. Russo, S. Vorndran, M. Escarra, H. A. Atwater, and R. K. Kostuk, "Reflection hologram solar spectrum-splitting filters," in *Regional Conference Series in Mathematics*, 2012.

[17] E. R. Torrey, P. P. Ruden, and P. I. Cohen, "Performance of a split-spectrum photovoltaic device operating under time varying spectral conditions," *J. Appl. Phys.*, vol. 109, p. 074 909, 2011.

[18] E. YABLONOVITCH and G. D. CODY, "Intensity enhancement in textured optical sheets for solar cells," *IEEE TRANSACTIONS ON ELECTRON DEVICES*, vol. 29, pp. 300–305, 1982.

[19] R. Winston, J. c. Minano, and P. Benitez, *Nonimaging optics*. Academic Press, 2005.

[20] R. Winston, "Light collection within the framework of geometrical optics," *J. Opt. Soc. Am.*, vol. 60, pp. 245–247, 1970.

[21] C. N. Eisler, C. A. Flowers, P. Espinet, S. Darbe, E. C. Warmann, J. Lloyd, M. Dee, and H. A. Atwater, "Designing and prototyping the polyhedral specular reflector, a spectrum-splitting module with projected >50% efficiency," in *IEEE PVSC 42*, 2015. DOI: http://dx.doi.org/10.1109/PVSC.2015.7356406,

[22] P. Hariharan, *Optical holography: Principles, techniques and applications*. Cambridge and New York: Cambridge University Press, 1996.

[23] R. Magnusson and T. K. Gaylord, "Analysis of multiwave diffraction of thick gratings," vol. 67, pp. 1165–1170, 1977.

[24] N. Ebizuka, K. S. Kawabata, K. Oka, A. Yamada, M. Kashiwagi, K. Kodate, T. Hattori, N. Kashikawa, and M. Iye, "Grisms developed for FOCAS," *Publ. Astron. Soc. Japan*, vol. 63, S613–S622, 2011.

[25] R. T. Ross, "Cross-correlation analysis of dispersive spectrum splitting techniques for photovoltaic systems," *J. Chem. Phys.*, vol. 46, pp. 4590–4593, 1967.

[26] R. R. King *et al.*, "Band gap-voltage offset and energy production in next-generation multijunction solar cells," *Prog. Photovolt.: Res. Appl.*, vol. 19, pp. 797–812, 2011.

[27] M. S. Agamy, S. Chi, A. Elasser, M. Harfman-Todorovic, Y. Jiang, F. Mueller, and F. Tao, "A high-power-density DC-DC converter for distributed PV architectures," *IEEE J. Photovolt.*, vol. 3, pp. 791–798, 2013.

[28] J. Russo, S. Vorndran, Y. Wu, and R. K. Kostuk, "Cross-correlation analysis of dispersive spectrum splitting techniques for photovoltaic systems," *J. Photon. Energy*, vol. 5, no. 1, p. 054 599, Jan. 2015.

[29] National Renewable Energy Laboratory. (2010). Simple model of the atmospheric radiative transfer of sunshine, [Online]. Available: `http://www.nrel.gov/rredc/smarts/` (visited on 10/09/2016).

[30] ——, (2010). National solar radiation database (NSRDB), [Online]. Available: `https://maps.nrel.gov/nsrdb-viewer` (visited on 10/09/2016).

[31] S. Larouche and L. Martinu, "OpenFilters: Open-source software for the design, optimization, and synthesis of optical filters," *Applied Optics*, vol. 47, pp. C219–C230, 2008.

[32] R. Varache, C. Leendertz, M. E. Gueunier-Farret, J. Haschke, D. Muñoz, and L. Korte, "Investigation of selective junctions using a newly developed tunnel current model for solar cell applications," *Solar Energy Materials and Solar Cells*, vol. 141, pp. 14–23, 2015. DOI: `doi:10.1016/j.solmat.2015.05.014`.

[33] C. N. Eisler, C. A. Flowers, E. C. Warmann, J. V. Lloyd, and H. A. Atwater., "The polyhedral specular reflector: A spectrum-splitting multijunction design to achieve ultrahigh (>50%) solar module efficiencies," *In prep.*, 2017.

[34] W. Qiu, "PDMS based waveguides for microfluidics and EOCB," Master's thesis, Louisiana State University, 2014.

[35] M. Woodhouse and A. Goodrich, *A manufacturing cost analysis relevant to single- and dual-junction photovoltaic cells fabricated with III-Vs and III-Vs grown on Czochralski silicon*, Web page, Cambridge and New York, Sep. 2013. [Online]. Available: `http://www.nrel.gov/docs/fy14osti/60126.pdf`.

[36] C. N. Eisler, R. A. Ze'ev, M. T. Sheldon, X. Zhang, and H. A. Atwater, "Multijunction solar cell efficiencies: Effect of spectral window, optical environment and radiative coupling," *Energy Environ. Sci*, vol. 7, pp. 3600–3605, 2014.

[37] M. Shiao, "The global PV inverter landscape 2013: Technologies, markets, and survivors," GTM Research, Tech. Rep., 2013. [Online]. Available: `http://www.greentechmedia.com/research/report/the-global-pv-inverter-landscape-2013`.

[38] T. J. Hebrink, "Durable polymeric films for increasing the performance of concentrators," in *Third Generation Photovoltaics*, V. Fthenakis, Ed., 2012, ISBN: 978-953-51-0304-2. DOI: `10.5772/1386`.

[39] P. Moitra, B. A. Slovick, Z. G. Yu, S. Krishnamurthy, and J. Valentine, "Experimental demonstration of a broadband all-dielectric metamaterial perfect reflector," *Applied Physics Letters*, vol. 104, p. 171 102, 2014.

[40] I. Staude, A. E. Miroshnichenko, M. Decker, N. T. Fofang, S. Liu, E. Gonzales, J. Dominguez, T. S. Luk, D. N. Neshev, I. Brener, and Y. Kivshar, "Tailoring directional scattering through magnetic and electric resonances in subwavelength silicon nanodisks," *ACS Nano*, vol. 7, pp. 7824–7832, 2013.

[41] N. Yu, P. Genevet, M. A. Kats, F. Aieta, J.-P. Tetienne, F. Capasso, and Z. Gaburro, "Light propagation with phase discontinuities: Generalized laws of reflection and refraction," *Science*, vol. 334, p. 333, 2011.

[42] C. F. R. Mateus, M. C. Y. Huang, Y. Deng, A. R. Neureuther, and C. J. Chang-Hasnain, "Ultrabroadband mirror using low-index cladded subwavelength grating," *IEEE Photonics Technology Letters*, vol. 16, pp. 518–520, 2004.

[43] B.-H. Cheong, O. N. Prudnikov, E. Cho, H.-S. Kim, J. Yu, Y.-S. Cho, H.-Y. Choi, and S. T. Shin, "High angular tolerant color filter using subwavelength grating," *APPLIED PHYSICS LETTERS*, vol. 94, pp. 213104-1–213104-3, 2009.

[44] E.-H. Cho, H.-S. Kim, B.-H. Cheong, P. Oleg, W. Xianyua, J.-S. Sohn, D.-J. Ma, H.-Y. Choi, N.-C. Park, and Y.-P. Park, "Two-dimensional photonic crystal color filter development," *OPTICS EXPRESS*, vol. 17, pp. 8621–8629, 2009.

[45] V. Karagodsky and C. J. Chang-Hasnain, "Physics of near-wavelength high contrast gratings," *Optics Express*, vol. 20, pp. 10 888–10 895, 2012.

[46] B. C. P. Sturmberg, K. B. Dossou, L. C. Botten, R. C. McPhedran, and C. M. de Sterke, "Fano resonances of dielectric gratings: Symmetries and broadband filtering," *Optics Express*, vol. 23, A1672–A1686, 2015.

[47] S. S. Kruk, C. Helgert, M. Decker, I. Staude, C. Menzel, C. Etrich, C. Rockstuhl, C. Jagadish, T. Pertsch, D. N. Neshev, and Y. S. Kivshar, "Optical metamaterials with quasicrystalline symmetry: Symmetry-induced optical isotropy," *Phys. Rev. B*, vol. 88, pp. 201 404–201 404, 2013.

[48] H. L. Yuhan Yao and W. Wu, "Spectrum splitting using multi-layer dielectric meta-surfaces for efficient solar energy harvesting," *Applied Physics A*, vol. 115, pp. 713–719, 2014.

[49] Y. Yao, H. Liu, and W. Wu, "Fabrication of high-contrast gratings for a parallel spectrum splitting dispersive element in a concentrated photovoltaic system," *Journal of Vacuum Science and Technology B*, vol. 32, 06FG04-1–06FG04-6, 2014.

[50] M. G. Moharam and T. K. Gaylord, "Rigorous coupled-wave analysis of planar-grating diffraction," *J. Opt. Soc. Am.*, vol. 71, pp. 811–818, 1981.

[51] M. A. Green, K. Emery, Y. Hishikawa, W. Warta, and E. D. Dunlop, "Solar cell efficiency tables (version 47)," *Progress in Photovoltaics: Research and Applications*, vol. 24, pp. 3–11, 2015.

Appendix A

OPTICAL DATA

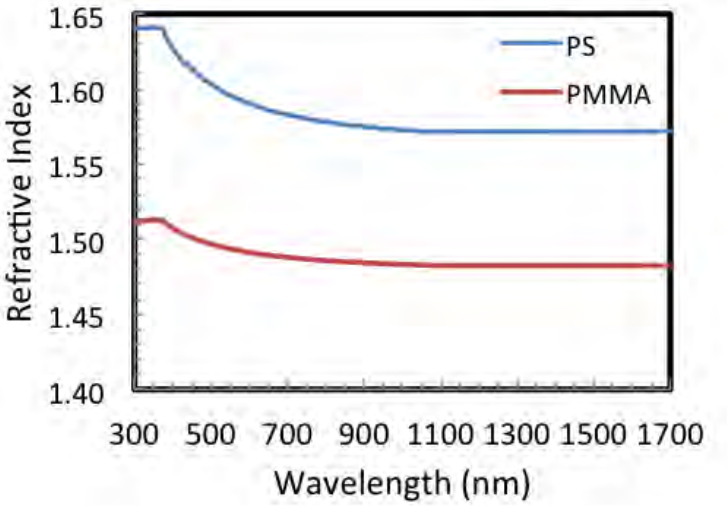

Figure A.1: Refractive index for polystyrene (PS) and polymthylmethacrylate (PMMA), the materials used for the high and low refractive index layers, respectively, in the polymer filters.

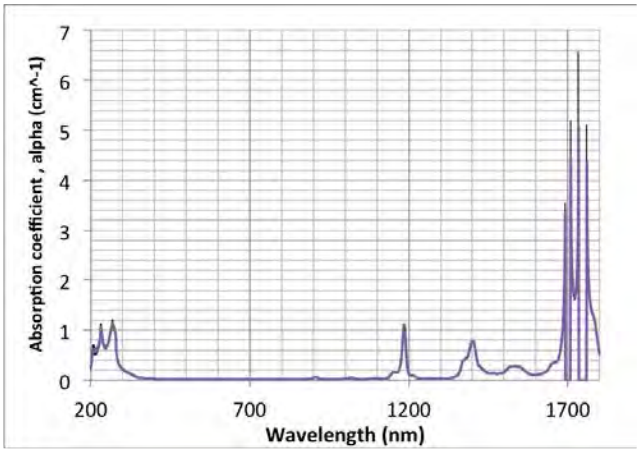

Figure A.2: Sylgard 184 2:1 base:curing agent absorption coefficient.

Appendix B

CPC DETAILS

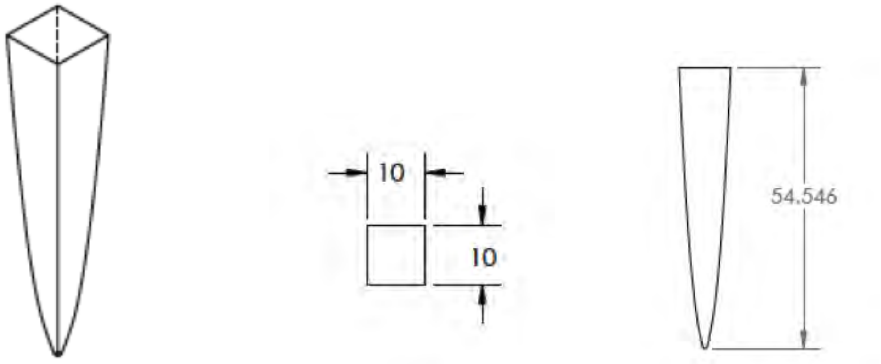

Figure B.1: perspective, top and side views of the 194X concentrator defined by the prototype design.

Sample name	Efficiency
12/4 898	62.0% ± 3.4%
11/26 #1	69.6% ± 3.1%
11/26 #2	67.7% ± 3.8%
11/25/14 898	64.6% ± 6.4%
PDMS	62.2% ± 4.3%
11/25 897	66.8% ± 4.5%
12/2 10:1	63.5% ± 2.0%
11/25 #3	66.3% ± 2.5%
11/25 #4	68.4% ± 2.6%
12/4 897 B	68.57% ± 1.7%
Average	66.0% ± 3.6%

Table B.1: Measured concentrator efficiencies

Mold fabrication

1. Mix 4:1 ratio of base to binder of Sylgard 184 together in a centrifuge tube
2. Use the PDMS centrifuge to mix and then spin the mixture to blend the two components and then remove some of the incorporated air

3. place the open vacuum tube under mild vacuum (with a dessicator in our case) to further remove air from the mixture for 10-15 minutes
4. Pour mixture around suspended positive part
5. Further degas for up to 40 minutes
6. Cure for 40 minutes at 80°C
7. When cool, gently extract the positive from the PDMS

Mold use

1. Mix 2:1 ratio of base to binder of Sylgard 184 together in a centrifuge tube
2. Repeat the mixing, degassing and curing procedure as above
3. Add collar to the mold to create an extra height to use to extract the CPC from the mold
4. Pour the PDMS mixture into the mold and degas for up to 40 minutes
5. Cure for at least 40 minutes at 80°C

Appendix C

COST MODEL

Technoeconomic analysis and bottom-up cost model

- Define the product, i.e. for a solar technology, to compare to alternatives this should be an installed area of a particular size in a particular place to be able to arrive at an LCOE that can be compared to competing technologies, especially for a higher $\$/W_p$ technology for which the advantage will be in LCOE rather than in $\$/W_p$.
- fill in missing components, e.g. racking and mounting hardware that have not yet been specified. Go with off-the-shelf, conventional parts where possible
- Compile a full bill of materials for the product
- Identify multiple sources for each input and find listed prices for off-the-shelf parts and get quotes (ideally 3+) for custom items

Bottom-up cost model

- For a bottom up model specify all steps to get from inputs to the final product in consultation with all project partners
- To incorporate scaling, get quotes at varying orders of magnitude until the price stops changing.
- Identify vendors operating at different scales – some respond well to pet projects. These are not likely to be the same vendors who can handle gigawatt scale production.

Appendix D

MATLAB CODE

Implementation of generalized couple wave analysis

9/26/16 12:02 PM /Users/sunitadarbe/Documen.../multiwave.m 1 of 3

```
function [Angle,DETE,TotOutTE,DETM,TotOutTM]...
                        = multiwave(phi,L,d,theta,n,n1,wl,modes,varargin)
format compact
global AngOut c v C D p
% ========================================================================
% MULTIWAVE gives the diffraction efficiency of 2*p+1 output modes for
% given input wavelength, angle and grating parameters; from R. Magnusson
% and T. K. Gaylord, "Analysis of multiwave diffraction of thick gratings"
% (1977)
% ========================================================================
%  INPUTS
%   d = thickness of grating in microns
%   phi = angle of grating in radians
%   theta = incident angle in radians
%   wl = incident wavelength in microns
%   L = period of grating in microns
%   n = average index of refraction of grating
%   n1 = amplitude of index of refraction modulation
% ========================================================================
%  OUTPUTS
%   AngOut = output angle for each of the 2p+1 outputs considered in
%       DEGREES!
%   DETE = diffraction efficiency of the output mode
%       exiting at output angle AngOut for polarization perpendicular to
%       the plane of incidence
%   DETM = diffraction efficiency of the output mode
%       exiting at the output AngOut for polarization in the plane of
%       incidence
%   TotOutTE = sum of DETM for all 2p+1 modes
%   TotOutTM = sum of DETE for all 2p+1 modes
%
% ========================================================================
%   ASSUMPTIONS
%   Completely lossless material assumed.
% ========================================================================

p = modes;                              % scalar
K = 2*pi/L;                             % scalar
b0 = 2*pi*n/wl;                         % scalar
C = -1i*2*pi*n1/wl;
D = 1i*2*pi*n1/wl;
v=zeros(2*p+1,1);                       % dephasing factor
c=zeros(2*p+1,1);                       % obliquity factor
AngOut = zeros(1,2*p+1);
ModeNum = 1:1:2*p+1;
k = ModeNum-p-1;
v = k*K*cos(theta-phi)-k.^2*K^2/2/b0;  % dephasing factor
c = cos(theta)-k*K*cos(phi)/b0;        % obliquity factor
AngOut = atan((b0*sin(theta)-(ModeNum-p-1)*K*sin(phi))...
                              ./(b0*cos(theta)-(ModeNum-p-1)*K*cos(phi)));
Angle = AngOut*180/pi;

% ========================================================
%       Solve Coupled ODEs for a 2*p+1 modes (TE and TM)
% ========================================================

BCs = zeros(2*p+1,1);
BCs(p+1) = 1;
```

```
[Xte,STE] = ode45(@MWTESolve,[0:d/3000:d],BCs);
[Xtm,STM] = ode45(@MWTMSolve,[0:d/3000:d],BCs);

% ============================================================
%          Calculate Diffraction Efficiency vs Angle
% ============================================================

DETE = cos(AngOut(ModeNum))./cos(theta).*(STE(length(STE),ModeNum)...
                                        .*conj(STE(length(STE),ModeNum)));
DETM = cos(AngOut(ModeNum))./cos(theta).*(STM(length(STM),ModeNum)...
                                        .*conj(STM(length(STM),ModeNum)));

% ============================================================
%                        Data Output
% ============================================================

TotOutTE = sum(DETE);
TotOutTM = sum(DETM);

 if nargin > 8
    figure
    subplot(2,2,1:2)
    plot(k,DETM,'*-',k,DETE,'o-')
    title(['Diffraction Efficiency vs. Mode, Wavelength = '...
                    num2str(wl)' d = ' num2str(d) ' L = ' num2str(L)...
                                            ' theta = ' num2str(theta)])
    legend('TM Polarization','TE Polarization')
    subplot(2,2,3)
    hold all
    for l = 1:1:2*p+1
    %     if AngOut(l) > pi/2
    %       msg = sprintf('Dimension mismatch occured: AngOut too big');
    %     end
         plot(Xte,STE(:,l).*conj(STE(:,l)),'.')
    end
    title(['TE Polarization, phi = ' num2str(phi)])
    subplot(2,2,4)
    hold all
    for l = 1:1:2*p+1
       plot(Xtm,STM(:,l).*conj(STM(:,l)),'.')
    end
    title('TM Polarization')
 end
end

%============================================================
%          TE, perp (H-mode) polarization
%============================================================

function dS = MWTESolve(z,S)
global C c D v p
dS = zeros(2*p+1,1);
dS(1)=  -1/c(1)*(1i*v(1)*S(1) + 1i/2* (S(2)*D) );
    for k = 2:1:2*p+1
        if k == 2*p+1
            dS(k)=  -1/c(k) * (1i * v(k) * S(k) + 1i/2*( S(k-1)*C ) );
        elseif k == p+1
            dS(k) = -1/c(k) * ( 1i/2* ( S(k-1)*C + S(k+1)*D ) );
```

RSoft data import into MATLAB and plotting

```
        else
            dS(k)=  -1/c(k) * (1i*v(k)*S(k)+ 1i/2*( S(k-1)*C+S(k+1)*D ) );
        end
    end
end

%=========================================================
%          TM, non-perp (E-mode) polarization
%=========================================================

function dS = MWTMSolve(z,S)
global C c D v p AngOut
dS = zeros(2*p+1,1);    % a column vector, with p even
dS(1)=  -1/c(1)*(1i*v(1)*S(1) + 1i/2* (S(2)*D*cos(AngOut(1)-AngOut(2))));
dS(2*p+1)=-1/c(2*p+1)...
    *(1i*v(2*p+1)*S(2*p+1)+1i/2*(S(2*p)*C*cos(AngOut(2*p)-AngOut(2*p+1))));
    for k = 2:1:2*p
        if k == p+1
            dS(k)=-1/c(k)*(1i/2*(S(k-1)*C*cos(AngOut(k-1)-AngOut(k)))...
                        + S(k+1)*D * cos(AngOut(k)-AngOut(k+1)) ) );
        else
            dS(k)=-1/c(k)*(1i*v(k)*S(k)+1i/2*(S(k-1)*C*cos(AngOut(k-1))...
                -AngOut(k))+S(k+1)*D * cos(AngOut(k)-AngOut(k+1))  ) );
        end
    end
end
```

```
function [phi, L] = Angle(deswl, ThOut,theta,n)
format compact
% ========================================================================
% ANGLE finds phi and L for a grating that optimizes diffraction efficiency
% of diffraction order +1 for a given wavelength and output angle according
% to the equation in Gaylord
% ========================================================================
%  INPUTS
%   deswl = free space wavelength of input light in MICRONS
%   ThOut = output angle in DEGREES; direction in which high diffraction
%   efficiency is desired
%   theta = input angle in DEGREES
%   n = average index of refraction of the HOE
% ========================================================================
%  OUTPUTS
%   phi = angle of the grating in DEGREES; defined as the angle between the
%       grating normal and the K vector which is in the direction of
%       sinusoidal variation. phi range is from -90 to +90 degrees
%   L = period of sinusoidal variation of refractive index in the grating
%       in MICRONS
% ========================================================================
%   ASSUMPTIONS
%   Simple holographic grating with sinusoidal variation in refractive
%   index in a complete lossless material
% ========================================================================

% ============================================================
%        Finding PHI
% ============================================================
if ThOut < 0       % if bending light in negative x direction
    % defines phi as deviation from 90° of magnitude ThOut/2
    phi = 90 - abs((ThOut+theta)/2);
    L = double(findL(phi,deswl,ThOut,n));
elseif ThOut > 0   % bending light in positive x direction
    phi = -90 + abs((ThOut-theta)/2);  % opposite sign to keep abs(phi)<90
    L = double(findL(phi,deswl,ThOut,n));
elseif ThOut == 0
    phi = NaN;
    L = NaN;
end
% ============================================================
%        Finding L
% ============================================================
function [L] = findL(phi,wl,ThOut,n)
syms period                     % makes 'period' a symbolic variable
b0 = 2*pi*n/wl;
K = 2*pi/period;
% solving for the period
S = solve(tand(ThOut) ==  (-K*sind(phi))./ ( b0-K*cosd(phi) ),period);
% makes the solution S into a floating point number
L = vpa(S);
```

9/26/16 11:46 AM untitled4 1 of 1

```
%% Hemispherical average with no azimuthal dependence
angle = [(phi(2)-phi(1))*([1:length(phi)]) * pi /180];
dtheta = phi(2)-phi(1)*pi/180;

% Calculate the hemispherical solid angle associated with each angle
Hemis = 2*pi * sin(angle) .* cos(angle) * dtheta;

% Calculate the hemispherical irradiance (assumed totally diffuse
% sunlight) weighted R and T and normalize by the total projected
% solid angle of the hemisphere (should be pi if integrating over angle =
% 0 to pi)

TotalRef = (Hemis * R_test)/sum(Hemis);
TotalTrans = (Hemis * T_test)/sum(Hemis);
```

9/26/16 11:45 AM untitled3 1 of 1

```
%% Making a well-labeled color plot
figure('units','normalized','outerposition',[0 0 1 1])
for e=1:structSize
    subplot(B,D,e)
    pcolor(eval(xvar),eval(yvar),LSCHCG14(e).Rte)%
    shading flat; colorbar;
    caxis([0 1])
    title([strcat(LSCHCG14(e).name)],'FontSize',fontSize)
    set(gca,'FontSize',fontSize)
    xlabel(Xlabel,'FontSize',fontSize)
    ylabel(Ylabel,'FontSize',fontSize)
end
h=colorbar;
figtitle([ftitle,' Rte'])
title(h,'Rte','FontSize',fontSize);
colormap jet
saveas(gcf,[ftitle,'Rte.jpg']); saveas(gcf,[ftitle,'Rte.fig'])
```

9/26/16 11:45 AM untitled2 1 of 1

```
%% Read data from text files into MATLAB (e.g., RSoft .dat files)

cd '/Users/sunitadarbe/Documents/MATLAB/RSoft/correct_folder'
files=dir('*.dat');
fileinfo=dir('*.syms');

R_col=1;
T_col=2;

for ji = 1:Number_of_files
    name = fileinfo(ji).name;    % syms file name
    runIDij = fopen(name);
    C=textscan(runIDij,'%s %f','delimiter','='); % gets variable values
    scaninfo_uns(ji,:)=C{2}';             % stores them
    fclose(runIDij);                       % closes syms file
    M=dlmread(files(ji).name,' ',1,1);     % opens .dat file of same name
    R(ji,:)=M(:,R_col)';
    T(ji,:)=M(:,T_col)';
end
```

Appendix E

PRELIMINARY HIGH CONTRAST GRATING FABRICATION

High contrast grating fabrication was attempted in two material systems. Amorphous Si and GaP layers were patterned by ebeam lithography and etched by ICP-RIE etching. Procedures, results, and discussion of remaining work is presented below. The a-Si material was deposited by PECVD directly onto a SiO_2 slide while GaP was deposited via MOCVD onto Si. The layer was wafer-bonded onto a SiO_2 slide using SU-8 and the Si etched away by XeF_2. Process development of this lift-off procedure and more detailed results are described in Hal Emmer's thesis. A Leica Microsystems EBPG-5000+ was used for electron beam lithography and a Oxford Instruments System 100 ICP 380 for ICP-RIE etching.

GaP Patterning

1. Clean the surface of the GaP layer, e.g. rinse and sonicate in acetone and IPA and dry on a hotplate
2. Spin on resist according to manufacturer's specification (30 s, 3000 repm for ma-N 2403 and prebake 90°C for 60 s)
3. Thermally evaporate ~5 nm Al layer.
4. Pattern via ebeam lithography.
5. Develop resist (base developer, e.g. mf-319, which is a TMAH solution, so it also removed the Al layer)
6. ICP-RIE etch (a functional but not optimized recipe for n-doped 100 and intrinsic 112 oriented GaP films: 30 sccm Ar, 5 sccm Cl, 2000 W ICP, 50 W forward power
7. Remove remaining resist if needed

a-Si Patterning

1. Clean the surface of the a-Si layer
2. Spin on resist (e.g. 950 A2 PMMA)

3. Deposit ~5 nm Al layer
4. Pattern via ebeam lithography.
5. Develop resist (MIBK-IPA followed by IPA dunk to stop development). A quick O_2 plasma (~5 s) serves to clear residue.
6. Deposit alumina etch mask (used 15 nm for ~300 nm etch depth)
7. Remove remaining resist
8. ICP-RIE etch using a pseudo-Bosch etch (SF_6/C_4F_8 - see Mike Henry's thesis for details)

Results

A couple of a-Si gratings and a single GaP dose array were prepared. The a-Si gratings were all patterned by ebeam lithography without an aluminum charge dissipation layer. This caused charge build-up during exposure which led to beam deflection during the pattern writing. The results of this are shown in Figures E.1a and E.1a. The optical image shows a patchwork of domains. Zooming in closer by SEM shows that what should be a hexagonal grating has many distortions including nearest neighbor grating elements subsumed into a single grating element in the bottom left to dimer patterns elsewhere. In contrast, the bottom two images of Figure E.1 shows a uniform hexagonal GaP grating. For the latter sample, a 5 nm Al layer was thermally evaporated on top of the resist to dissipate the charge. (The Al was thermally deposited to avoid exposing the ma-N resist which is also a UV-curable resist with the stray radiation an ebeam evaporation step would produce.) This prevented the beam deflection and resulted in a significantly more accurate ebeam lithography writing step.

Two sets of SEM images were taken to assess the GaP RIE etch. The recipe was recommended for etching n-type 100 GaP, but the film I used was an intrinsic 112 layer. A dose array was made, and one patch (15 nA beam, 1250 $\mu C/cm^2$ dose) was imaged in depth. As shown in Figure E.2a, a large defect was present in one of the dose array segments. Pillars at the edge of this defect were measured (Figure E.2b). Additionally, an *in-situ* Pt deposition and FIB cross-section milling were done at the center of the grating. In both regions, the etch seems to have resulted in pillars with fairly straight side walls. At the defect edge, the etch seems to have got fully through the GaP layer and into the SU-8 as seen in the ridge toward the bottom of

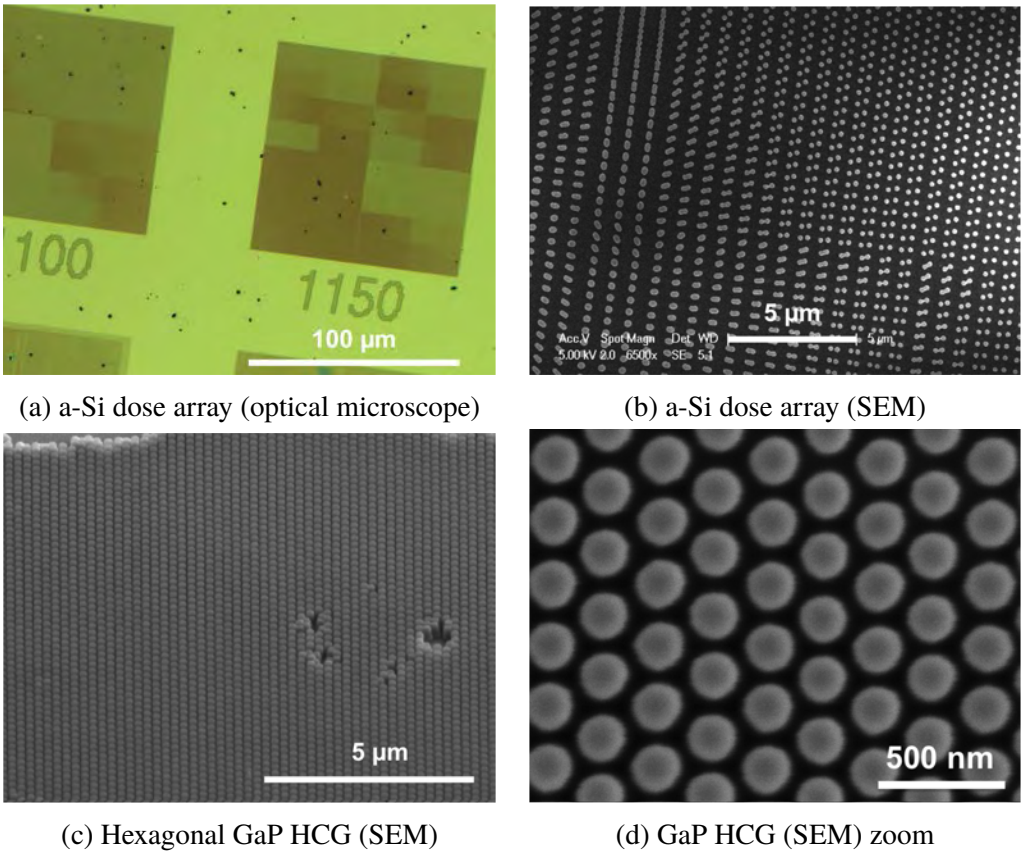

(a) a-Si dose array (optical microscope)

(b) a-Si dose array (SEM)

(c) Hexagonal GaP HCG (SEM)

(d) GaP HCG (SEM) zoom

Figure E.1: (top) Pattern drift in what should be a hexagonal grating due to charge build-up during ebeam lithography of a-Si film on quartz; (bottom) GaP grating patterned through 5 nm Al without pattern drift.

the pillars in Figure E.2b. In contrast, in the more central portion of the grating, the GaP film seems to be etched only part of the way through and the total thickness seems to be less than at the defect edge.

There are many possible regions for the mismatch between the etch results at the defect edge and in the middle of the grating. It is possible the GaP film itself had thickness variations. However, such a ~100 nm variation in a 400 nm films within 100 µm seems unlikely given that the 1 cm by 1 cm film visually appears quite uniform. It is also possible that the ma-N resist thickness varied. The sample geometry was not optimal for uniform spin coating. The SiO_2 substrate 2.5 cm by 2.5 cm with the 1 cm by 1 cm GaP film transferred onto it. This was then cross-sectioned, and the smaller of the two resulting pieces was used for the dose array. The SiO_2 substrate was rectangular, and the GaP film was not centered on the substrate. In addition, there was a ring of SU-8 around the edge of the film. In fact, I attempted to measure the thickness of the GaP layer by profilometry. However,

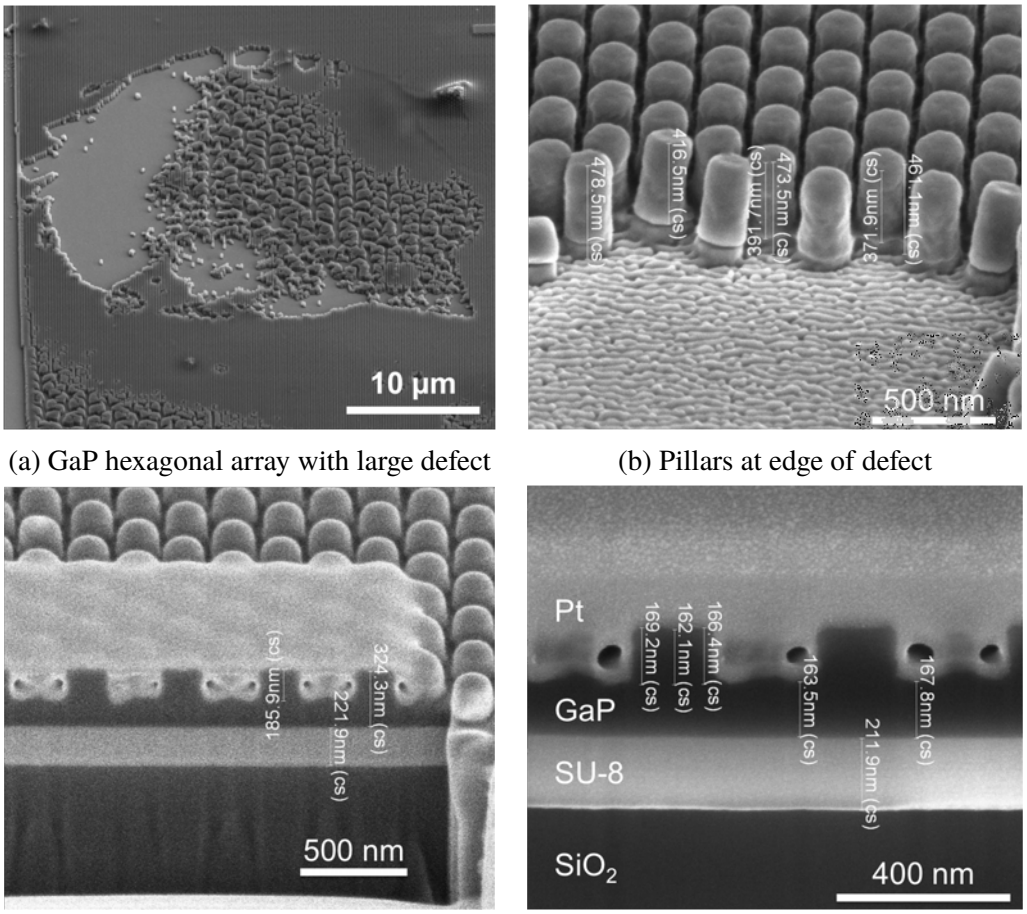

(a) GaP hexagonal array with large defect

(b) Pillars at edge of defect

(c) *In-situ* Pt deposition and FIB milling

(d) Pillars within grating

Figure E.2: While the GaP at the edge of the defect (a) appears to be etched fully through the GaP layer (b), the GaP away from the defect in the bulk of the layer appears only partially etched.

during the wafer bonding process, excess SU-8 from between the GaP, and the SiO_2 substrate leaked out forming a ring around the GaP which was 1-2 orders of magnitude taller than the GaP layer. All of this lends itself to uneven spin-coating of the resist on the sample. Thus in the bulk region if the ma-N thickness was lower, it is possible that the resist was etched through faster, removing material from the top of the pillars during the etch and accounting for the smaller overall thickness. Given the dense packing of the grating elements, it is possible that there was more restricted gas flow during the etch in bulk regions of the grating rather than near the defect edge, giving a high etch rate at the defect edge. These accumulated uncertainties underscore the need for characterization between each processing step to identify the source of such issues. Thus attempts to measure the GaP thickness by profilometry led to the stylus moving the whole sample rather than moving across

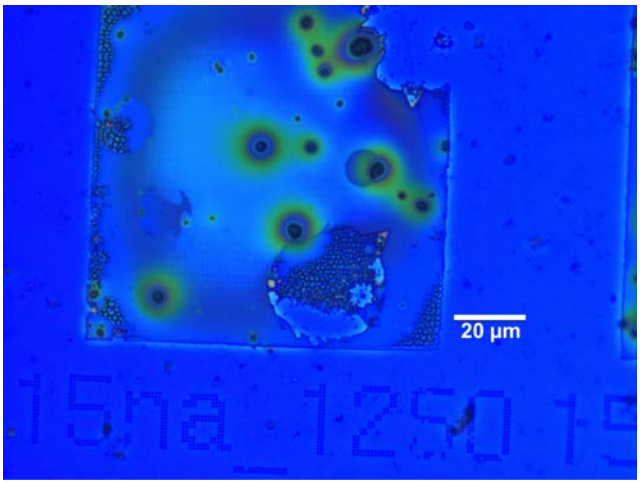

Figure E.3: Optical microscope image of one pattern in GaP dose array showing many defects in the array as well as many particles or dust specs around the grating.

the sample even with the sample vacuum on. Records from Chris Chen and Rebecca Saive who grew the layer suggested it was around 200 nm. SEM measurements after patterning and etching, however, suggested a thickness closer to 400 nm.

Another remaining concern to be addressed in future HCG fabrication is better cleaning of the semiconductor layer before processing. Figure **??** shows many defects in the grating as well as particles strewn across the surrounding area. Other cleaning options include plasma ashing followed by an oxide etch. If the defects are due to the presence of particles, this will be a problem for large scale uniformity. An additional possible source of defects within the grating is the high dose. The recommended amount for ma-N 2403 is closer to a few hundred $\mu C/cm^2$. It is possible that over-exposure caused the resist to bubble, forming some of the defects. Finally, the dust could be embedded in the SU-8 film between the GaP and the SiO_2 substrate.

Attempts at repeating the patterning at a larger scale in the other half of the same GaP cross-sectioned film failed at the patterning step. The developed resist showed no pattern. Possible reasons for this failure include little or no resist stuck to the GaP film in the initial spin-coating step, the Al layer was too thick for the exposure to go through the whole resist layer, the Al evaporation step somehow developed the whole resist layer, and that the film was overdeveloped. The only difference I know of between the first and second sample was that the second had an additional cleaning step of ultrasonication in acetone. The ultrasonication also caused some flaking off of GaP film material. It is however possible that some additional treatment was

applied to one half of sample before it was give to me, e.g. some sort of surface treatment that would affect the adhesion of ma-N.

Future work in fabricating high-contrast gratings requires optimization of film cleaning, uniformity of the spun-coat resist layer, and optimization of the etch conditions.

Tips

Some stray pieces of accumulated wisdom from the many folks who trained me in lab:

- Start the fabrication process with a dose array straddling the suggested dose range for the resist to select optimal value. Generally, a smaller beam current gives more precision, but a longer exposure is required to achieve the target dose (in Coulombs/area), so the exposure is slower.
- Prepare beakers with all needed baths ahead of time for wet chemical processes, e.g. set up beakers for development and rinses to follow the developer, especially if the development time is sensitive.
- Confirm via optical microscopy that each step has been successful.
- It is hard to find a 50 μm x 50 μm pattern on a 1 cm^2 sample so large noticeable markers are very useful for locating patterns for any characterization or measurement after fabrication, e.g. a thick large box or thick text markers written with a low resolution beam (e.g. 50 na or 100 na beam).
- Dose arrays need to be just large enough to image to ensure that the process has gone well. If not doing proximity corrections about 100 μm x 100 μm is large enough to provide an interior region that is not experiencing edge proximity effects. With proximity corrections even smaller is possible.
- Scribing an 'F' or other non-mirror symmetric symbol on a wafer can help identify if the correct side is up on a transparent substrate with a transparent thin film on it.